Model representation of a downslope windstorm in North-west Iceland

A thesis submitted to the School of Environmental Sciences
of the University of East Anglia in partial fulfilment
of the requirements for the degree of Doctor of Philosophy

Wilhelm W. T. Hodder

September 2023

ABSTRACT

The role of turbulent exchange of heat and moisture in the lee of mountains is not well understood, and these processes are generally not resolved or parametrised in numerical weather prediction (NWP) models.

High resolution Met Office Unified Model (MetUM) simulations are run and compared to in-situ observations from 12th and 19th March 2018 over Snæsfellsnes peninsula and the Westfjords, in north-western Iceland. With sub-kilometre horizontal grid-scales flow features – such as a downslope windstorm coupled with a hydraulic jump and a wave-breaking region directly aloft – are well resolved and provide suitable cases for testing different MetUM science configurations.

The model simulations have been evaluated against aircraft observations, as well as radiosonde and ground-based observations and the 0.5-km horizontal grid-spacing simulation is found to reproduce the resolved features with reasonable fidelity. As a result, the 0.5-km simulation has been established a suitable truth for model sensitivity studies.

A detailed case study analysis of a downslope windstorm over a meso-scale ridge on the 19th March 2018 is conducted and shows that the reproduction of the event is highly sensitive to resolution and is not represented in the global driving model. Analysis of the downstream impacts of the 0.5-km simulation compared to the 4.4-km and global simulations shows large lee-side differences nearest to the slope, but these differences generally attenuated to background levels within 140 km. Changing the default boundary layer turbulence parametrisation for one employing a long-tailed stability function produced similar differences seen in the resolution-sensitivity.

An 11-year climatology using the Copernicus Arctic Reanalysis (CARRA) is conducted to place the case study event into climatological context and to investigate the downstream impacts of these events on the large-scale flow. The event is found to be a moderate event for the region and time-averaged composites revealed weak, but consistent wake signatures.

ACKNOWLEDGEMENTS

I'd like to thank my primary supervisor Prof. Ian Renfrew for guiding me in my scientific development and for his untiring understanding, patience and support. I'd like to also thank Dr Andrew Elvidge for his insightful feedback, advice and ideas that helped me develop a narrative for this thesis. I would like to give thanks to Dr Peter Sheridan for his time and effort in organising my visits to the Met Office, and I am very grateful for our fortnightly virtual catch-ups, with their many insightful discussions. I would also like to thank Dr Simon Vosper for his constructive advice and expertise. I'd like to extend my thanks to all the other members of the Orography Group at the Met Office, past and present - Dr Steve Derbyshire, Dr Annelize van Nierkerk, Dr Tom Dunstan - for letting me join in their Orography Group meetings, and for their encouragement and advice. I would like to give special thanks to Dr Guðrún Nína Petersen for providing me with the ground-based atmospheric observations from the Icelandic Meteorological Office and for her invaluable insight into the weather and climate of Iceland.

I would like to thank the UK Met Office for the CASE partnership that has enriched my PhD so greatly. I would also like to extend my thanks to the Natural Environment Research Council for funding this PhD and for the School of Environmental Sciences at UEA for hosting me these last four and half years. I offer my thanks to all those involved in the Iceland Greenland Seas Project for collecting the incredibly useful aircraft observations that I had the privilege of using in my research.

My appreciation goes to my friends and colleagues, who have made this journey feel a little less daunting and made me feel at home in a new city. And lastly, to my family I express my heartfelt gratitude for their support and encouragement and unwavering belief in me.

CONTENTS

LIST OF FIGURES

LIST OF TABLES

1

INTRODUCTION

The mountainous island of Iceland is situated at the important juncture of Arctic atmospheric weather- and climate systems and the oceanic Atlantic Meridional Overturning Circulation (AMOC). The complex coupling between the atmosphere and the ocean in this region, with air-sea exchange of heat, moisture and gases, sea-ice interface with the ocean and atmosphere, and the development of impactful meso-scale weather systems, such as polar lows, has been subject to ongoing atmospheric research pursuits and recent field campaigns (e.g. Renfrew *et al.* (2019)). A significant question is the role of orographic flow in these systems, which is atmospheric flow modified by mountains and other types of topography (collectively referred to as orography). Iceland (Figure 1.1) is located south-west of the coast of Greenland and is surrounded by the Irminger Sea, the Iceland Sea (a dense water source to the AMOC (Lozier *et al.* (2019))), and the Denmark Strait, which is host to an overflow water current called the Denmark Strait Overflow and connects the Iceland and Irminger Sea (Almansi *et al.* (2020)). In this thesis we will explore the potential impacts on the atmosphere over the Denmark Strait and Iceland Sea of orographic flows over a small Icelandic peninsula, and attempt to elucidate the potential importance of such a meso-scale and easily overlooked mountain range on the regional weather and climate.

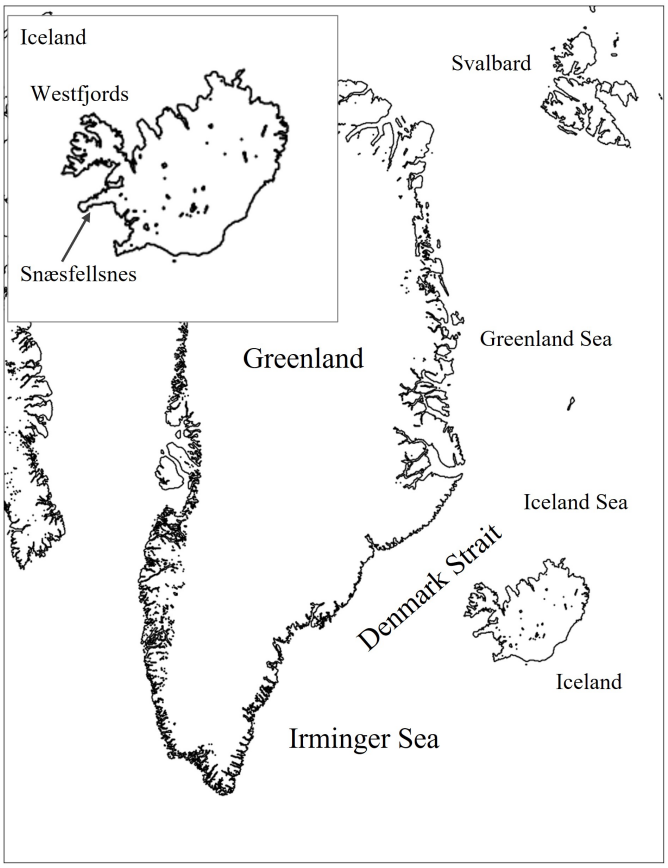

Figure 1.1: Coastline map of Arctic Regional Reanalysis, CARRA-West domain, with key geographic areas named. An enlarged map of Iceland highlights the location of the Snæsfellsnes and Westfjords peninsulas.

1.1 BACKGROUND

1.1.1 GRAVITY WAVES AND STRATIFIED FLOW

Mountains modify atmospheric flow in numerous ways, for example they cause drag and dissipate momentum through gravity waves, provide a physical barrier to flow leading to air diverting up and around mountains, and they create unique lee-side flow features. Gravity waves (often also called mountain waves) can occur in different ways, such as vertically propagating gravity waves, hydraulic jumps, which are forms of standing waves, and often include or coincide with features like gap flows (e.g. Mayr *et al.* (2007); Gaberšek & Durran (2004)); Foehn wind jets (e.g. Elvidge *et al.* (2015)); turbulent rotors in the ABL forming underneath gravity waves through wind shear (e.g. Sheridan & Vosper (2005)), wavebreaking regions, overturning aloft and mesoscale downslope windstorms (e.g. Smith (1987); Gohm *et al.* (2008)). These

features will all be addressed later in this section.

To better understand these features in the context of atmospheric flow encountering a barrier, three physical contributors have to be considered: the atmospheric stability, the wind speed and direction incident on the mountains, and the orography itself (Whiteman (2000); Jackson *et al.* (2013); Wallace & Hobbs (2006)). When these aspects are quantified as the Brunt–Väisälä frequency, or buoyancy frequency, N, the ambient, dominant or synoptic wind speed U, and the mountain height h, they can be combined to give the Froude number Fr, a scalar quantity used to describe the flow conditions (around mountains) in terms of their linearity. This is therefore an important, even if limited, quantification in Ronald B. Smith's linear theory of mountain waves (Smith (1980, 1988, 1989)). Fluid flow is considered linear if it can be effectively described using the linear forms of the Navier-Stokes equations; see table 1.1 for a breakdown of mountain flow behaviour in different flow regimes defined by Fr. The equation for Fr is given in 1.1.

$$Fr = \frac{U}{Nh} \tag{1.1}$$

Often the quantity $\hat{h} = 1/Fr$, called the non-dimensional mountain height, is used and may explain the meaning of the quantity better here: in the context of an air parcel moving towards a mountain barrier, Fr and $\hat{h}$ correspond to a ratio between the kinetic energy held by the approaching airflow ($U^2/2$) and the equivalent required gravitational potential energy to overcome the barrier height ($N^2h^2/2$). Smith (1980), Smith (1988), Smith (1985) and Durran (1986) show that when $\hat{h} < 1$ the mountain is effectively low enough for the momentum of the flow to carry the air parcel over the crest and smoothly recover to its original altitude where buoyant forces are balanced, which is described as linear flow (Table 1.1). When $\hat{h} > 1$ the mountain height is too large for low-level flow to ascend over the mountain and the flow is increasingly blocked with increasing $\hat{h}$ (or decreasing Fr), and has to move around the mountain ridge if the mountain is 3-D (e.g. conical), or is blocked if it 2-D (e.g. a long ridge); an alternative interpretation in this case is that for $Fr \ll 1$ the atmosphere is so strongly stratified (i.e. high N) that the restoring force on a vertically displaced air parcel is too strong for the parcel's momentum to overcome. At $Fr \approx 1$ the flow is also non-linear.

Gravity waves generally interact with the top of the ABL and the atmospheric layers above, for example when lee waves form in the boundary layer and are capped

Fr	$\hat{h}$	Flow behaviour
$\ll 1$	$\gg 1$	Non-linear/sub-critical: air will flow around the sides of a mountain or is blocked if the mountain is effectively 2-D.
1	1	Non-linear/critical: Layers of air just below the mountain top will flow over the mountain while lower layers may be blocked. Air flowing over will penetrate into lower altitudes and buoyantly recover to it's upstream flow level in a wave motion.
$\gg 1$	$\ll 1$	Linear/super-critical: air will flow unimpeded over the mountain. the flow lines are parallel and can be described by linear mathematics.

Table 1.1: Fr flow-regimes with corresponding $\hat{h}$ and the mountain flow behavior these values are associated with.

by an atmospheric temperature inversion aloft, which can evolve into stationary hydraulic jumps that may penetrate deeper towards the surface under increasingly non-linear conditions (Vosper (2004); Vosper *et al.* (2018)). Through this interaction gravity waves can facilitate the transport of momentum, heat and moisture across the boundary top (Vosper *et al.* (2018)). Mountains can also have related impacts that are not only felt in the wind; hot, dry Foehn, for example in the case of the Diablo winds in Northern California (e.g. Smith *et al.* (2018)), can increase the risk of wild fires, while the ascent of moist air on the windward slope can lead to unique cloud formation and precipitation as the air cools (e.g Miltenberger *et al.* (2020)).

1.1.2 DOWNSLOPE WINDSTORMS

OVERVIEW

Downslope windstorms are caused by a large-amplitude gravity wave, that produces strong critical (where $Fr \approx 1$ and flow is non-linear, see Table 1.1) near-surface winds and windstorms are known for the strong gusts on the surface of the steep downwind slopes of mountains (e.g. Jackson *et al.* (2013)). An insight into their history of observation and numerical modelling will be provided in the introduction to Chapter 3, and past climatologies and the sensitivities of downslope windstorms to changes in the large-scale atmospheric circulation will be covered in the introduction

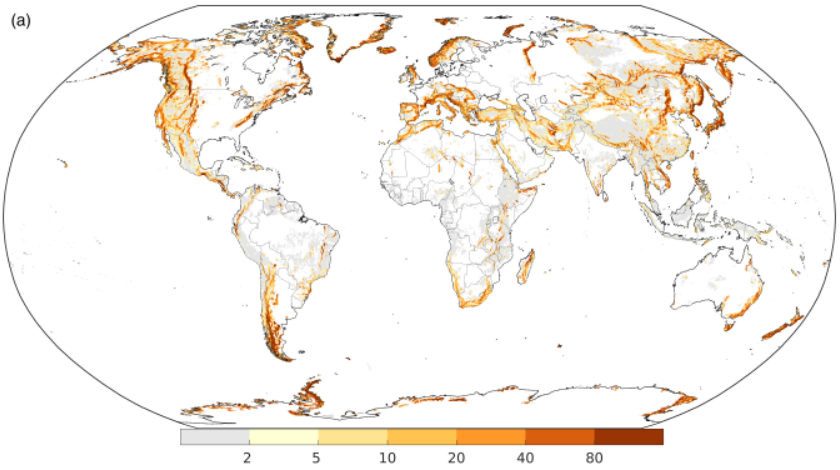

Figure 1.2: Map of average annual days where Abatzoglou *et al.* (2020) detected downslope windstorm activity in the ECMWF's ERA5 1979-2020 dataset. From Figure 5 in Abatzoglou *et al.* (2020).

to Chapter 4. Downslope windstorms are widespread and have real impacts on the environment and weather around mountain ranges and the communities that live there (e.g. Lilly & Zipser (1972)). Figure 1.2 shows a distribution of meso-scale downslope windstorm activity around the globe, which highlights how widespread these events are and how important to local weather and climate they might be (Abatzoglou *et al.* (2020)). Particularly the relatively high concentration of annual days with downslope windstorm activities seen in Iceland and eastern Greenland motivates a closer inspection of these events in this thesis.

Well known examples of downslope windstorms in the world include the Adriatic Bora (e.g. Smith (1987); Jiang & Doyle (2005)), the Boulder Colorado Windstorm (e.g. Lilly & Zipser (1972)), and the Puelche Foehn over the Andes (e.g. Beusch *et al.* (2018)). Iceland features several distinct recurring windstorms, such as the named Freysnes Windstorm (Ólafsson & Ágústsson (2007)) and unnamed windstorms on the slopes of the Snæsfellsnes peninsula south of the Westfjords (Ágústsson *et al.* (2007)) (see Figure 1.1 for location) and Mt Öræfjökull (Rögnvaldsson *et al.* (2011)). Downslope windstorms often have features ranging from 20 km to several hundred kilometres in size, which makes them generally smaller than other types of storm systems, such as those associated with synoptic scale cyclones. Lee side effects of windstorms include fast surface-level jets, rotors, and wave-breaking related potential vorticity banners (e.g Jiang & Doyle (2005)). The smaller scale of these features can mean they generally need high resolution models with grid-spacings at resolving scale (e.g. for a

20 km feature to be resolved, the grid-spacing needs to be no greater than 2-3 km) to accurately represent them (Vosper *et al.* (2018)), and may be missed in coarser global NWP models, climate models, and reanalyses.

THEORY

Figure 1.3 shows an example of a downslope windstorm studied in this thesis as modelled by the Met Office Unified Model (UM). The gravity wave is notable in the isentropes above the ridge, and is seen to propagate vertically upward. Closer to the slope the isentropes of a strongly stratified atmospheric layer at crest height are further compacted, which would correspond to an area of strongly accelerated surface wind while further aloft overturning isentropes suggest the existence of a wave-breaking zone. In the lee of the mountains the isentropes recover from their transition from sub-critical into super-critical flow in a hydraulic jump. Concordant with Vosper (2004), concentrations of momentum flux in the wave-breaking zone and below the hydraulic jump suggest areas of enhanced turbulence. Modelling by Hertenstein & Kuettner (2005) and Doyle & Durran (2007) showed that this turbulence is generated from wind-shear between the mountain wave and the ambient initially undisturbed flow above and below the wave causing rotors (eddies in the atmosphere linked to waves) to form.

Jiang & Doyle (2009) investigated the role atmospheric moisture has in mountain waves during the T-REX campaign in the Sierra Nevada , and found that gravity wave amplitude is reduced for relative humidity maxima > 70 % at mountain crest height, and established a wave-response regime for different upstream moist layer depths. Adding to this , Rögnvaldsson *et al.* (2011) found that simulated cloud microphysics is also found to have a variable impact dependent on the difference in the simulated hydro-meteor and moisture distribution. There are three fundamental theories that have been used to describe the formation of downslope windstorms:

1. Two-layer hydraulic flow, where a stable layer or inversion separating a neutrally or weakly stable boundary layer from a stably stratified upper layer near peak-height undergoes a hydraulic transition from sub-critical flow to fast, super-critical flow over the lee-side slope (Long (1954); Smith (1985); Durran (1986); Klemp & Durran (1987)).

2. Vertically propagating vertical waves reflect off a pre-existing critical (inversion-

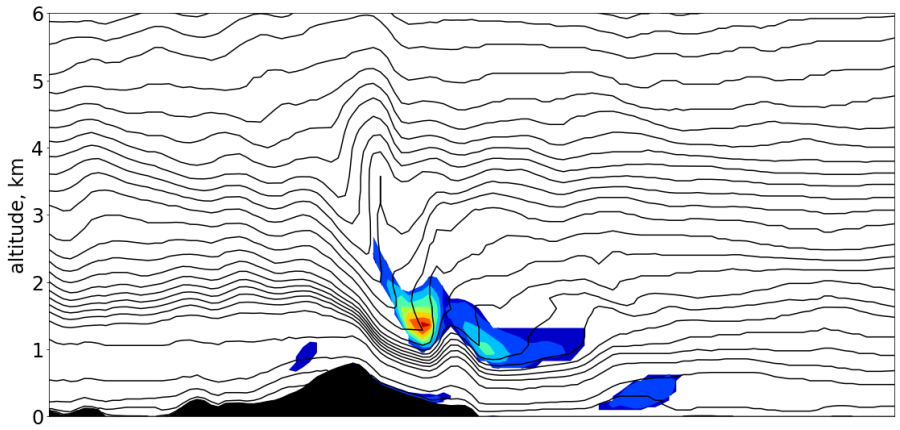

Figure 1.3: Day-time vertical cross-section of 0.5 km grid-spacing regional atmosphere UM forecast over the Westfjords, Iceland (see Chapters 2 to 4). Black contours are 1 °C isentropes of dry potential temperature and color depicts windstress values greater than 0.5 N m^{-1}. Wind flows from left to right.

like) layer aloft, typically the tropopause, and constructively interfere by the mountain amplifying the flow momentum over the lee-side slope (Klemp & Lilly (1975)).

3. Vertically propagating gravity waves reflect off a self-induced critical layer (where the ambient flow speed is equal to the phase speed), created by wave-breaking aloft, where the isentropes of the wave reverse and momentum is dissipated (Peltier & Clark (1979)); this reflection results in a downward momentum flux and amplification of flow speed on the lee-side slope.

These theories have been directly compared (e.g. Durran & Klemp (1987)) extensively reviewed in the literature (e.g Jackson *et al.* (2013)), and the hydraulic theories of Smith (1985) and Durran (1986) have been shown to satisfy observations of and numerically modelled representations of downslope windstorms. More recently, Vosper (2004) has built on the work of Smith (1985) and Durran (1986) as the theoretical basis for their description of lee-waves and lee-side flow separation leading to rotor formation and Abatzoglou *et al.* (2020) has performed a global climatological study detecting synoptic scale downslope windstorms in the ERA5 reanalysis dataset using criteria based in the hydraulic theory.

As described above, downslope windstorms attract scientific interest due to the risk they pose to people and property. With understanding of windstorm evolution and behaviour being continually refined, the theory can be applied to both modelling

efforts to improve forecasting downslope windstorms and detecting past downslope windstorms in climatologies.

1.1.3 APPLICATIONS OF WINDSTORM CLIMATOLOGY

The applications of downslope windstorm climatologies are numerous. Smith *et al.* (2018) used ground-based observations and found Diablo winds, Foehn winds linked to severe wildfires in Northern California, to be abundant and diverse in structure, intensity and flow direction. Serafin *et al.* (2017) performed a 5 year climatological study in Owens Valley, also in Northern California, using ground-based atmospheric observations to characterise westerly wind events (WWE). Plavcan & Mayr (2014) used a statistical algorithm on ground-based weather station data to detect Foehn wind events in the Wipp Valley, Alps, exclusively using wind speed measurements, at a similar frequency as when other quantities are included in the selection criteria. Closer to our ridge in the Westfjords, Ólafsson & Ágústsson (2007) complimented their case studies with a climatological analysis of the Freysnes windstorm with wind speed measurements to study their seasonal distribution and used an ECWMF reanalysis to characterise atmospheric shear aloft during Freysnes windstorm events. Ágústsson *et al.* (2007) also used an ECWMF reanalysis and climate model to characterise the Kvísker downslope windstorm in Iceland, and elucidate the binary modality of events like that and the Freysnes windstorm, where one type is characterised by greater strength and a short series of large-amplitude lee-waves, while the other, less frequent, type has stronger wind shear aloft suppressing the growth of lee-waves.

In Southern California Hughes & Hall (2010) employed the North American Regional Reanalysis and a 12-year climate simulation to constrain the synoptic conditions leading to the formation of Santa Ana winds, another Foehn-like flow linked to regional wildfires. They found that a high-pressure anomaly directing flow perpendicular into the front mountain ranges greatly contributes to the generation of strong surface winds. Guzman-Morales *et al.* (2016) use a downscaled reanalysis from the California Reanalysis Downscaling project, to investigate a 65 year climatology of the Santa Ana Wind, which they found to have increased in intensity since 1970 and to be sensitive to the Pacific Decadal Oscillation (PDO) and the El Niño cycle. It can

be reasoned that this sensitivity to large scale cyclical variations in climate echoes the sensitivity to initial conditions in Reinecke & Durran (2009)'s windstorm simulations.

Shestakova *et al.* (2020) conducted a detailed multi-decadal climatological study for several downslope windstorms in the Russian Arctic, using a combination of the Arctic System Reanalysis (with horizontal grid-spacing of 15 km) and ground-based observations. They found that the windstorms at different locations are diverse, with wide ranges in frequency, intensity and temperature, and also showed that the frequency of events is sensitive to the PDO, but the incoming flow characteristics of the events less so.

Montecinos *et al.* (2017) conducted a climatological study to characterise the Puelche winds, large (order 100 km in scale) easterly Foehn-like winds on the western slopes of the Andes, using the Climate Forecast System Reanalysis (approx 50 km grid-spacing) of the National Centers for Environmental Prediction (CFSR-NCEP) for a 1979-2015 time period, and found that the associated Foehn warming extended hundreds of kilometers downwind from the slope at which the winds were detected, aided by low ambient humidity, lack of clouds, and radiative warming.

All of the discussed climatological studies focussed on specific windstorms, Foehn winds or regions, with several commonalities in their results, such as downstream warming and sensitivity to cyclical changes in the large-scale circulation. Abatzoglou *et al.* (2020) are the first to test a generalised method with multi-decadal ERA5 datasets to detect and study key parameters of downslope windstorms globally, with reasonable success. However their detection ability was limited to those synoptic scale windstorms that ERA5 can resolve with 31 km grid-spacing.

Ideally we need reanalysis models with grid-spacings of order 1 km to capture the full spectrum of downslope windstorms, gap flows, and Foehn jets with their finer details, like surface level jets, resolved, as was concluded in Chapter 3. How high-resolution models have been used in windstorm climatology, and one example of a potentially suitable dataset will be discussed in Section 4.1.1.

1.1.4 FOEHN-WARMING AND TURBULENT EXCHANGE IN THE BOUNDARY LAYER

Having established the dynamical basis of mountain waves and downslope winds in Sections 1.1.1 and 1.1.2, we can now expand our overview to how they affect the transport of heat and moisture through the atmosphere in the lee of mountains. Gap winds and Foehn winds bring warmer, dryer air into lower altitudes in the lee (Mayr *et al.* (2007); Elvidge & Renfrew (2016)). Given the right conditions, such as upstream blocking or gravity wave propagation (Gaberšek & Durran (2004)), gap flows, which are winds that flow through the troughs between peaks in a ridge, create a Foehn wind that has a distinctly higher speed than the ambient flow off the mountain peaks, but is also cooler and more moist due to their lower altitude sourcing (Elvidge *et al.* (2015)). These jets interact with the ambient leeside flow through shear forces and eventually mix with the surrounding air. This may enhance mixing of air from different atmospheric layers, depending on conditions. Elvidge & Renfrew (2016) detail the mechanisms by which Foehn winds form can vary in both process and importance (Figure 1.4): isentropic drawdown, latent heating and precipitation, mechanical mixing from turbulence and leeside radiative flux convergence can all have a significant impact on leeside warming. Of these warming mechanisms, all three of the former involve turbulent scalar flux in some way. However, the significance of these scalar fluxes to the evolution of the flow downstream remains an open question and they are not as yet explicitly parametrised in models (Vosper *et al.* (2018)). Some research has started to clarify the mechanisms of scalar turbulent flux in orographic flows. For example, the shear-generated turbulence at the top of the ABL shown in Hertenstein & Kuettner (2005) would dissipate momentum across the ABL through turbulent mixing, and could also vertically transport heat and moisture. Aircraft observations by Smith (1987) and Jiang & Doyle (2004) of the Adriatic Bora and an Alpine windstorm respectively measured vertical heat fluxes of 100 Wm^{-2} associated with hydraulic jumps in the lee. The question arises here whether these heat fluxes modulated by lee-side mountain waves significantly change the downstream temperature and moisture profiles of the atmosphere. This question will be explored in Chapters 3 and 4.

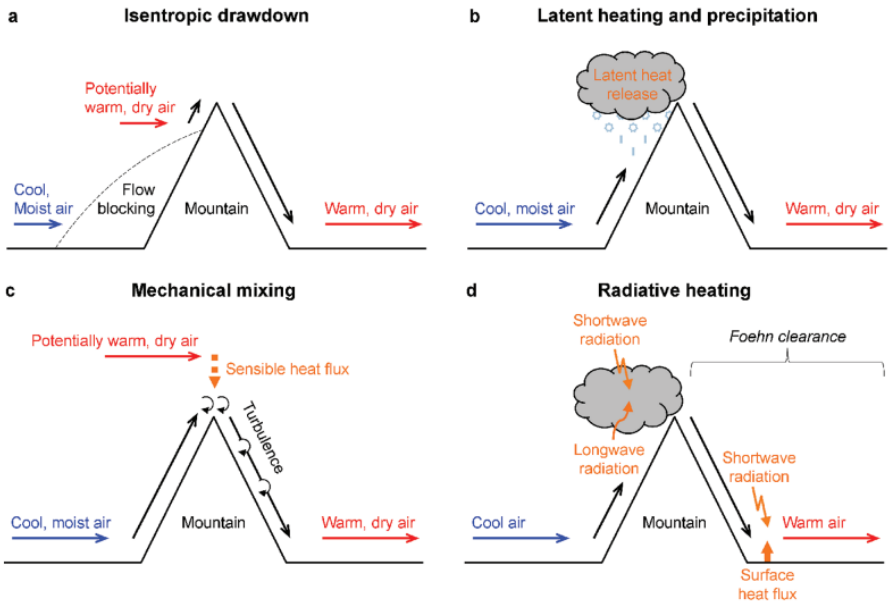

Figure 1.4: The different types of Foehn-warming mechanisms as seen in Figure 1 in Elvidge & Renfrew (2016).

1.1.5 CHALLENGES

At this point we need to establish the relevancy of the aforementioned background in the context of this thesis; what are the key challenges encountered when modelling mountain waves and downslope winds? Serafin *et al.* (2018), Vosper *et al.* (2018) and Sandu *et al.* (2019) are recent reviews of the literature that attempt to identify and summarise the challenges and gaps in our understanding of the interaction between mountains and the atmosphere and the challenges in modelling these processes. Serafin *et al.* (2018) identified a need to further improve the modelling of turbulence in the mountain boundary layer (which they defined as a form of the ABL over complex terrain, where low-level orographic flow processes dominate), and to improve understanding of how turbulence in the boundary layer interacts with flow at different scales ("multi-scale interaction"). This would include the impacts of lee-side mountain waves on the large-scale atmospheric circulation.

Vosper *et al.* (2018) considered the knowledge of turbulent exchange due to low-level gravity wave processes, and discussed that the traditional eddy-covariance turbulence closure methods used to calculate sub-grid scalar fluxes over complex terrain may not be sufficient on their own, and stressed that high resolution numerical weather prediction modelling with grids-spacing of order 100 m are

needed to model small-scale lee-side features, such as detailed rotors. They also highlight the need to develop sub-grid parametrisation schemes that fully include orographic scalar turbulent flux, as well as momentum flux, although theoretical understanding of scalar turbulent exchange requires expansion in order to do so.

Taking a global view, Sandu *et al.* (2019) addressed the cumulative impacts of orography on the large-scale atmospheric circulation, and discusses the requirement of observational constraints and high resolution simulations as solutions to make progress from our current state of knowledge and modelling capability. They state that future high-resolution (order 1 km) NWP studies should be applied to improve understanding of the distribution of orographic drag in all three spatial dimensions and how this distribution is linked to thermal stratification, particularly over differently-sized mountain ranges. Since many studies already focus on the large mountain ranges of the world (e.g. Rocky Mountains: Lawson & Horel (2015); Billings & Grubišić (2008); Andes: Beusch *et al.* (2018); and the Alps: Aebischer & Schär (1998)), a meso-scale mountain range, like those found in the Westfjords, Iceland, provide a suitable and novel experimental study location.

1.2 THIS THESIS

1.2.1 MOTIVATION

In this chapter we have discussed that orographic flows are air flows affected by nearby mountains, and express themselves in a variety of forms, including Foehn winds, gravity waves, and turbulent wakes. They occur on scales from the meso-alpha (200 to 1000 km) to the micro scale (≤ 1 km), and have significant impact on momentum, moisture, and heat transport in the atmosphere. They are associated with numerous natural disasters, including droughts, floods, and forest fires; accurate forecasting will enable damage reduction to property, and the saving of human lives. Furthering our understanding of these processes and how they are modelled will contribute to research in climate forecasting and what role mountains will play as anthropogenic climate change continues. However, forecasting orographic flows accurately faces numerous challenges, touched upon in Section 1.1.5, and particularly the role of turbulent heat and moisture flux in the lee of mountains is

an identified gap in the knowledge.

1.2.2 AIMS AND LAYOUT

The research presented in this thesis approaches the following general aims:

1. To improve understanding of the role and significance of scalar turbulent exchange in the lee of mountains,
2. to study the effect of turbulent flux parametrisation in the context of orographic flow representation in the UM,
3. and to investigate the impacts of mountain-modulated flow on the downstream scalar atmospheric state fields and the large-scale circulation in the Iceland-Greenland Seas.

To address these aims, we present our investigations as follows:

- Chapter 2: We use the Met Office Unified Model to run sub-km scale forecasts, which will be evaluated in detail against novel aircraft observations from the Iceland-Greenland Seas Project (IGP, Renfrew *et al.* (2019)). Ground-based observations provided by the Icelandic Meteorological Office, and radiosonde observations launched at Keflavik Airport will also be used to provide a comprehensive observational constraint in the lee and upstream of the mountains, and on the surface as well as aloft.
- Chapter 3: We present our case study of a downslope windstorm detected in the simulations evaluated in Chapter 2 in the Westfjords, and test the sensitivity of the windstorm's simulation to model resolution and changes in boundary layer turbulence parametrisation.
- Chapter 4: We evaluate an 11-year windstorm climatology using the novel high-resolution Copernicus Arctic Reanalysis dataset (CARRA), and attempt to overcome the limitations encountered in Chapter 3 case study analysis.

In Chapter 5 we summarise the findings of this thesis, discuss how they connect with the bigger picture laid out in this thesis introduction, and make our final conclusions.

2

EVALUATION OF SUB-KM UM REGIONAL FORECASTS DURING IGP CASE STUDIES

2.1 INTRODUCTION

2.1.1 EVALUATION OF NWP MODELS

Representing orographic flow and the transport of momentum, heat, and moisture within it in numerical weather prediction models (NWP) is challenging, since the complex orography interacting with the atmosphere breaks some of the common assumptions made in the model parametrisations (Vosper *et al.* (2018); Lehner & Rotach (2018)); the ability to evaluate a NWP simulation against observations enables the use of simulations with greater confidence, when we conduct case studies (Chapter 3) and climatological studies (Chapter 4).

Model evaluation usually involves comparing observational datasets directly to NWP model output, for example Sergeev *et al.* (2017) and Sheridan & Vosper (2012) applied aircraft data, a series of dropsondes, and satellite observations to evaluate Met Office Unified Model (UM) high-resolution (2.2 km and 1 km/0.333 km grid-spacing respectively) simulations of a polar low over the Norwegian Sea and of downslope winds over the Sierra Nevada respectively. Both represented the model-observation comparisons and highlighted biases in time-series and profiles.

When sufficient confidence in a high-resolution simulation is established, it can be compared to other simulations using different parametrisations or dynamics, for example Vosper (2015) and Vosper *et al.* (2016) investigated the performance of orographic drag parametrisations in UM simulations of the isolated mountain ranges of South Georgia and New Zealand, by comparing them to high-resolution simulations that resolved most of the drag and acted as controls. It is this method that informs our motivation in this chapter: to prove the UM regional model high-resolution simulations of the orographic flows around Iceland, and in particular the 0.5-km simulation, as effective control representations of the flow, which we can then compare to coarse resolution runs and sensitivity test runs in Chapter 3, and to reanalysis datasets in Chapter 4.

Furthermore, the Met Office Unified Model (UM) is a commercial product of the Met Office and so regular experimental evaluation of the Met Office's operational model in various locations and situations gives scientific, commercial, and strategic value to the Met Office, their clients, and collaborators.

2.1.2 CHAPTER OUTLOOK

The main aims of this chapter are to

- introduce the meteorology of the case studies,
- evaluate the model for the state variables and existing parametrised and derived flux variables using available in-situ observations,
- and to establish the UM 0.5-km regional simulation as a suitable control simulation for our case study investigation of a strong downslope wind event in Chapter 3.

This kind of model verification is not commonly done due to the rarity of lee-side aircraft observations (Renfrew *et al.* (2019)). Furthermore, a sub-km (0.5-km) grid-spacing is a higher resolution than the UM's standard operational configuration (1.5-10 km), and is therefore acting as a test for potential model development (Vosper *et al.* (2018)).

In this chapter greater emphasis is placed on the chronologically later of two case studies (labelled Case 1 and Case 2), which will be introduced in detail in Section 2.2.3.

Results are supported with aggregated values from Case 1. We chose to focus on Case 2 since it contains a strong wind event that will be further explored in Chapters 3 and 4. In Section 2.2 the model and the observations are introduced. In Section 2.3 the meteorology of the case studies is introduced via an overview of synoptic conditions from the global output, as well as the regional domains. In Section 2.4 the model output is evaluated against available observations and key features, such as biases, flow conditions and a strong wind event, are discussed, and in Section 2.5 the results of this chapter are summarised.

2.2 DATA AND METHODS

2.2.1 CALCULATING HORIZONTAL WIND SPEED

When horizontal wind speed is averaged across time, for example for a composite, it is calculated in a particular order across all chapters in this thesis. For horizontal wind velocity components u (northward) and v (eastward) at time t we apply quadrature to obtain

$$U(t) = \sqrt{u(t)^2 + v(t)^2} \tag{2.1}$$

where $U(t)$ is the scalar wind speed at a particular grid-point or flight run at time t. U is sometimes notated as wsp, and is sometimes also spatially averaged, depending on application - this will be clarified when done so. To obtain the time-averaged composite, $U(t)$ is then simply averaged across all defined time-steps.

2.2.2 MODEL SETUP

The experimental model setup evaluated in this chapter uses UM version 11.4 and the GLM6.1 global driving model (Walters *et al.* (2017)), which run on the non-hydrostatic deep-atmosphere ENDGAME dynamical core (Wood *et al.* (2014)), and were still recently new iterations in 2018 when this PhD project started. The global driving model used a horizontal resolution of N768 (approximately 17 km grid-spacing in mid-latitudes).

The model ran three 24 hour regional atmosphere forecasts with horizontal grid-

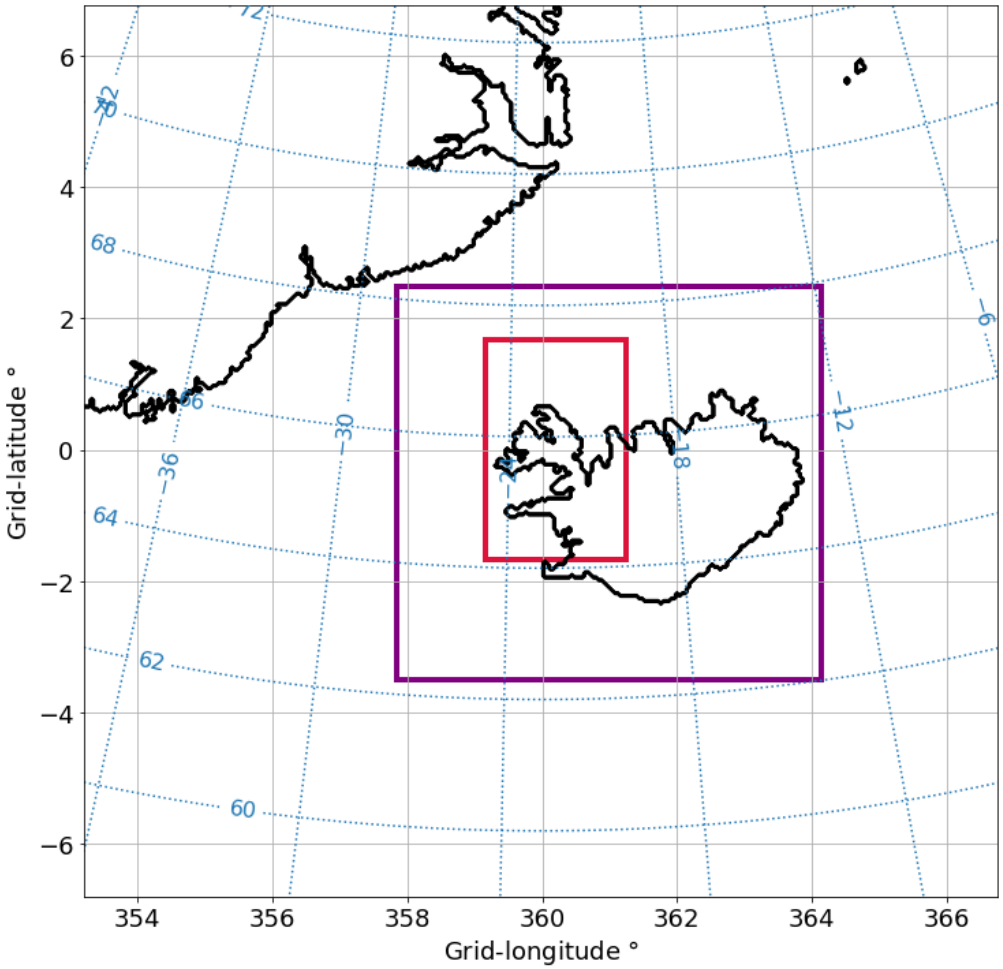

Figure 2.1: Map of 4.4-km domain with coastlines (black). The boundaries of the 1.5-km (purple) and 0.5-km (red) domains are given as boxes around the center of the map. The rotated grid is illustrated by the model grid-lines (grey) and the labelled Earth coordinate latitude-longitude lines (blue, dashed).

spacings of 4.4-km in the outermost domain, 1.5-km, and 0.5-km in the innermost domain, sourcing their lateral boundary conditions from the next one out; i.e. 0.5-km sourced from the 1.5-km domain, 1.5-km from 4.4-km, and 4.4-km sourced its lateral boundary conditions from the global driving model. The domain boundaries are illustrated in Figure 2.1.

The regional nests are run on a rotated model grid so that the grid equator passes through the domain making the grid closely Cartesian; this allows us to read the distances in our cross-sections in this thesis without having to account for significant skews from map projections. The rotated grid is illustrated by the x- and y-axes in Figure 2.1 and the Earth latitude-longitude gridlines are incldued for reference.

The configuration used for the regional atmosphere model is the UM RA1M

Domain name	Horizontal grid spacing	Grid size, y by x	Vertical grid spacing	Integration time step	Output time step
4.4-km	0.04°	340x340	70 levels - 40 km - ρ and θ levels	60s	1hr and 30min
1.5-km	0.015°	400x400	70 levels - 40 km - ρ and θ levels	30s	1hr and 30min
0.5-km	0.003°	1140x 840	90 levels - 40 km - ρ and θ levels	12s	1hr and 30min

Table 2.1: Details on regional model configuration. All domains use the semi-Lagrangian, non-hydrostatic dynamical core ENDGame. The regional UM physics configuration is RA1M, and the gravity wave drag scheme is switched off for 1.5-km and 0.5-km.

operational configuration, though with the gravity wave drag scheme switched off for the 1.5-km and 0.5-km simulations since its effect is negligible at those grid-spacings (personal correspondence with van Nierkerk and Sheridan, 2019). The regional model details are summarised in Table 2.1.

The configuration of the 0.5-km simulation will be used as a control simulation in Chapter 3, where we will compare the representation of a downslope windstorm in both the coarser resolution runs as well as in a sensitivity test run. For this purpose, even though more recent model versions have been released since, the model will be kept at vn11.4 and GLM6.1 for all further work in this thesis, which will keep the model consistent with the evaluation in this chapter.

2.2.3 CASE STUDIES AND EXAMINED FEATURES

As one of several efforts in recent years to constrain the variables involved in orographic flows, the Iceland Greenland Project (IGP) field campaign was undertaken; IGP is a coupled atmosphere-ocean project, which included two research flights over the steep and complex orography of two Icelandic peninsulas with the aim of investigating leeside turbulent exchange processes (Renfrew *et al.* (2019)). These two flights were identified as flights 301 and 306, and took place on the 12th and 19th March 2018 respectively. For the remainder of this chapter, the flights will be referred to as Case 1 (IGP 301) and Case 2 (IGP 306). The case studies

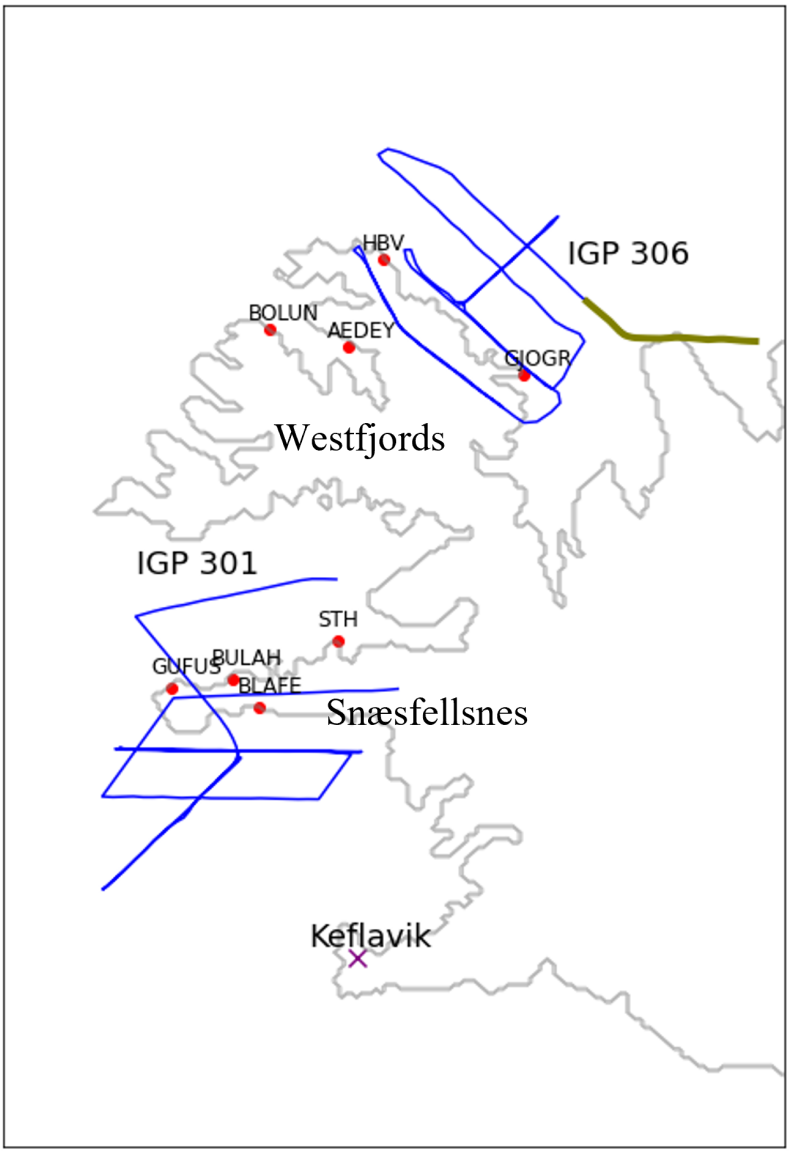

Figure 2.2: Map of sources of in-situ observations: IGP flights providing aircraft data (blue), ground-based atmospheric monitoring stations providing surface measurements (red), radiosonde sounding at Keflavik airport providing profiles (purple), and a non-run-averaged segment at the end of IGP flight 306 (case 2) used for downwind profiles (green). The Westfjords and Snæsfellsnes pensinsulas are labelled.

are further supported by radiosonde and ground-based weather station observations, which are not attributed to the IGP mission, but are instead monitored by the Icelandic Meteorological Office, providing a spatially and temporally broad suite of in-situ observations to allow for comprehensive analysis and model validation.

Flight observations predominantly took place in the lee of the mountain range, with a small number of flight legs either flown directly above the ridges or, in Case 1, upstream to provide an upwind profile for the case. The locations of each of the in-situ observation sources are illustrated in Figure 2.2. Uniquely these flights represent rare, low-level leeside turbulence observations in a strong mountain wind event, enabling a constrained study of heat and moisture fluxes in the lee, and may help to answer the question of the significance and importance of turbulent scalar exchange within a strong wind event. A summary of Case 1 and 2 flight legs is given in Table 2.2.

EXAMINED FEATURES

As will be shown in this and the following chapters, a number of features present in the case studies' observations and model forecasts will be examined. Case 1 features a low-level stagnation in the lee, alongside a number of gap flows. Case 2 features a downslope windstorm in conjunction with a directly aloft wave-breaking region and a hydraulic jump. Both cases show extensive wave patterns in the mountains' wakes. These are transient features, which suggests a certain level of luck that the aircraft was present during their life cycle. Furthermore, once validated against observations, the features seen in the model can be studied for their structure, life cycle, and impact on the modelled flow, in particular their influence and dependence on scalar turbulent fluxes. The downslope windstorm, its representation across different model configurations, and its downstream impacts on the synoptic flow will be more closely examined in Chapter 3 and 4.

2.3 SYNOPTIC CONDITIONS AND METEOROLOGY

2.3.1 CASE 2

Synoptically and locally, the Case 2 forecast is a complex and multi-factored case study. Iceland is shown in Figure 2.3 to sit at the conjunction of a high-pressure system to the south, and two strong low-pressure systems to the west over the North

Leg ID	Start time, UTC	End time, UTC	Altitude, ft	Distance, nm	Details
Case 1, IGP M301, 12 March 2018					
1	13:03	13:24	5000 - 6000	43	Profile across mountain crest
2	13:24	13:37	6000 - MSA	25	Transit and profile descent
3	13:37	13:59	MSA	43	Level
4	13:59	14:05	MSA	12	Transit and profile ascent
5	14:05	14:27	MSA	43	Level
6	14:27	14:50	MSA - 1000	43	Profile ascent
7	14:50	15:16	1000 - 3000	43	Profile ascent, then level
8	15:16	15:32	3000 - 5000	21	Profile ascent, then level
9	15:32	15:52	5000	40	Level
10	15:52	16:22	5000 - MSA	40	Profile descent, then level
Case 2, IGP M306, 19 March 2018					
1	13:00	13:46	4000 - 4500	82	Take-off, transit, level over ridge line
2	13:46	14:09	4000 - 4500	46	Level (MSA over ridge)
3	14:09	14:36	4000 - 6000	46	Saw-tooth
4	14:36	14:41	4000 - 1000	9	Transit and descent
5	14:41	15:05	1000	48	Level
6	15:05	15:18	1000 - 500	24	Descent, then level at MSA
7	15:18	15:30	500	24	Level
8	15:30	15:43	500 - 1000	24	Ascent, then level
9	15:43	15:56	1000 - 500	25	Descent, then level
10	15:56	16:02	500 - 80	12	Descent to MSA (>12 nm from coast)
13	16:02	16:24	80	43	Level
14	16:24	16:31	80 - 3500	10	Transit and ascent
15	16:31	17:01	80 - 3000	47	Saw-tooth

Table 2.2: Summary of Case 1 and 2 flight legs from mission plan. Numbering for Case 2 changed 10 and deviates from mission plan and was adapted to analysis. Onboard equipment recorded altitude, atmospheric state variables and aircraft velocity at 1 Hz and 50 Hz frequencies. All legs given were reprocessed into 12 s and 60 s run-averages where appropriate. MSA, though variable, was typically around 500 ft (150 m) over sea within 12 nm of the coast and 80 ft further than 12 nm from the coast.

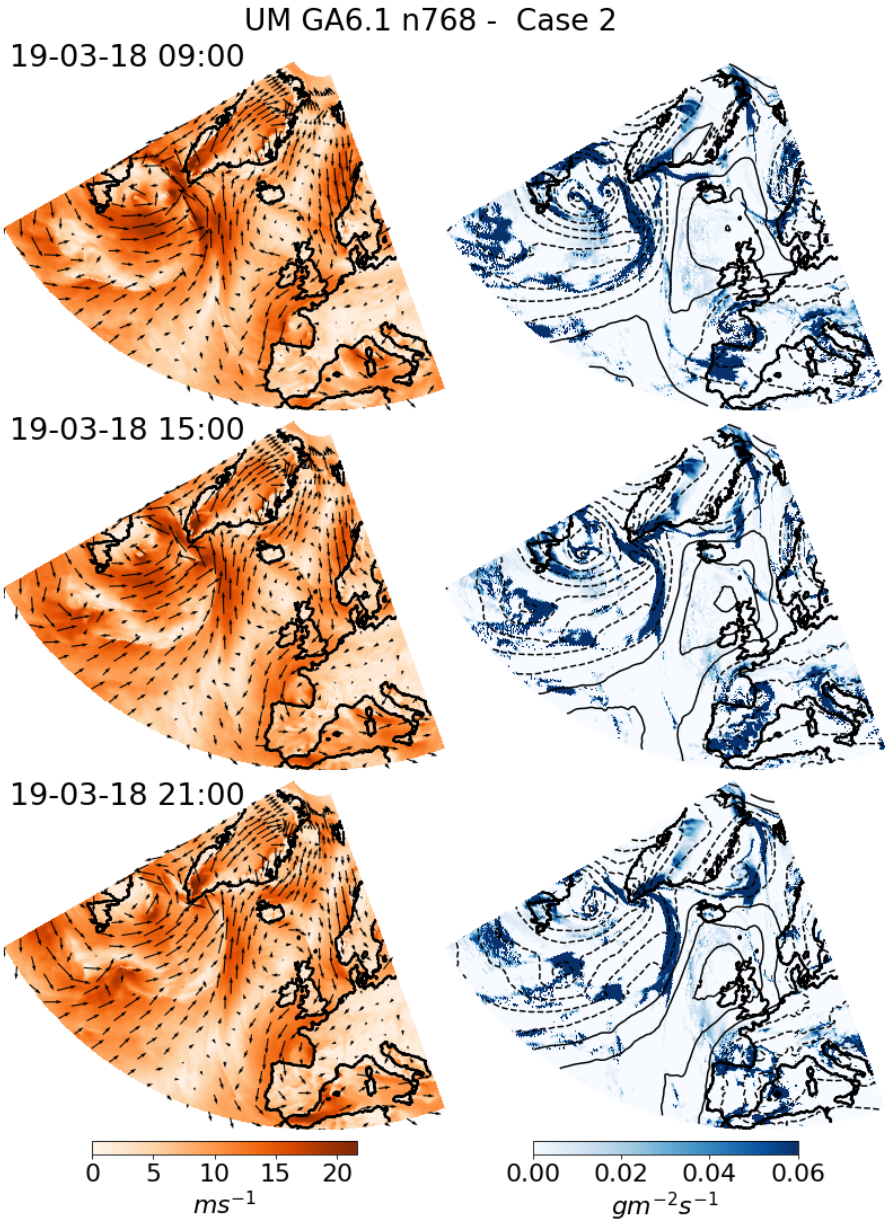

Figure 2.3: Case 2 UM global model surface diagnostic output subset with focus on the North Atlantic, North Sea, and Western Europe. Columns show 10-m horizontal wind speed on the left, and combined mean sea-level pressure (black contours) and surface precipitation flux (blue scale, with values above 0.06 g m^{-2} s^{-1} saturated to highlight lighter levels of precipitation seen near Iceland) on the right. The dashed contours represent pressure values below 1020-hPa, and therefore show low pressure centers. Contours are in 5 hPa steps. UTC on Case 2 forecast date.

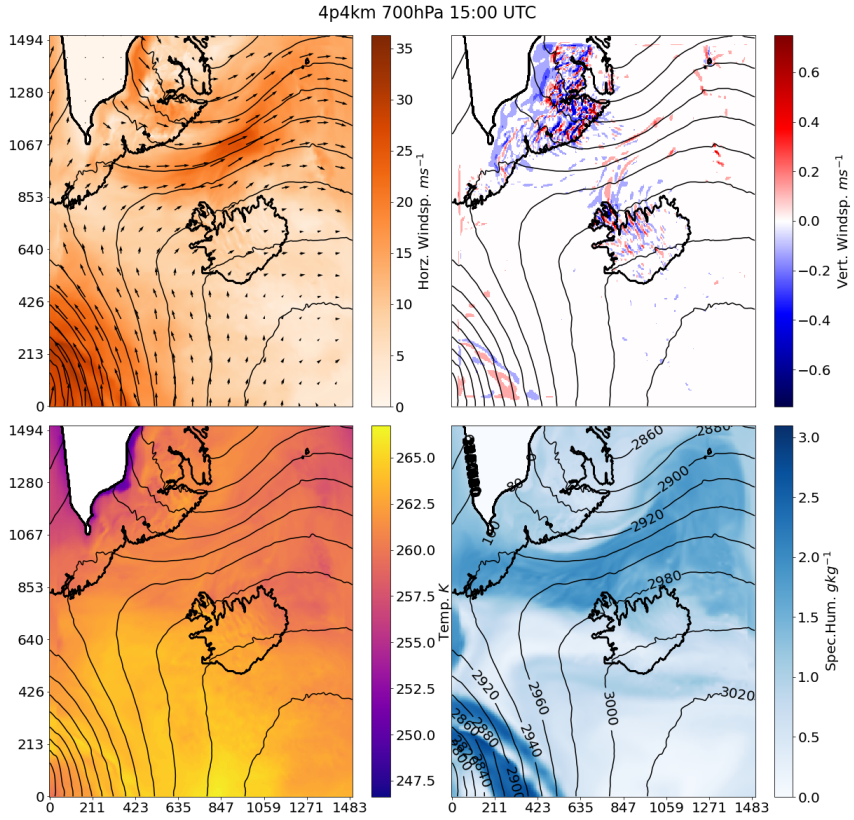

Figure 2.4: Map of Case 2 Regional Atmosphere model 4.4-km domain. Atmospheric state variables are shown at the 700hPa pressure surface at 15Z model time: horizontal wind speed (top left), upward wind speed (top right), air temperature (bottom left), and specific humidity (bottom right). Contours in each panel are geopotential height, and values in meters are labelled in specific humidity panel. Areas where surface altitude is intersected by the pressure surface are masked in white.

Atlantic and to the North over Greenland bringing in warmer air from the Atlantic Ocean into the Iceland-Greenland Sea region where it mixes with cooler air drawn down from over Greenland (temperature field not shown).

Fronts are visible in the precipitation flux, with significant bands of precipitation with values up to 0.4 g m^{-2} s^{-1} skirting the sea around Iceland and Greenland to the Southwest and Northeast. However, the sea in the immediate vicinity of Iceland sees an order of magnitude less precipitation throughout the forecast period, except a little to the East of the Iceland-Greenland Sea.

The meeting of the northern low and southern high causes a West-East

acceleration through the Iceland-Greenland Sea, as seen in greater detail in Figure 2.4. The acceleration combined with the westerly moist cooler air create a cool, moist geostrophic jet dominating the flow field in the Denmark Strait at 700-hPa. The distinct dry and warm conditions within the southern high over the area of the Atlantic Ocean immediately southwest of Iceland brings into question how much the air within this jet is mixed from the surrounding systems. The higher concentration of water held in the jet may be the source of precipitation seen to Iceland's Northeast in the global model output, where the jet appears to meet another air mass seemingly head-on as suggested by diverging isobars and an increase in vertical motion and decrease in specific humidity.

Throughout the forecast period both the northern and south-western low deepen, and the jet strengthens and eventually shifts eastward as the south-western low pushes deeper into the regional 4.4-km domain by the late evening (not shown). Meanwhile slower, southerly geostrophic winds dominate the region within which the higher resolution domains are situated, including the Westfjords, the area of focus for Case 2. The implications for the case study are that according to the model a jet of accelerated air may encroach onto the area where observations are taken.

At 0.5-km and 1.5-km resolutions accelerated geostrophic flow is visible throughout the afternoon skimming the northwestern edge of the Westfjords as the accelerated flow rotates from southwesterly to westerly and intensifies. The moist westerly wind and the warm southerly wind mix in the Denmark Strait, raising relative humidity and forming what appears to be a buffer, or layer of insulation from the cooler air mass further north, as seen in Figure 2.5. Further in the 0.5-km domain this contrast is more defined (Figure 2.6). The higher resolution resolves spatially attenuating low-level waves, as seen in the wakes of the coastal mountain ridge, yet these lee waves do not seem to radiate from the peaks northwards, but are confined by the aforementioned southeasterly air stream. Comparing upstream and lee-side conditions, the air descending from the Westfjords's northern coast is accelerated, dryer and warmer, which indicates Foehn-like warming is actively involved in the low-level lee-side flow. Granular patterns in specific humidity and vertical velocity seen in Figures 2.5 and 2.6 may be a signature of the milder precipitation seen in the area in Figure 2.3.

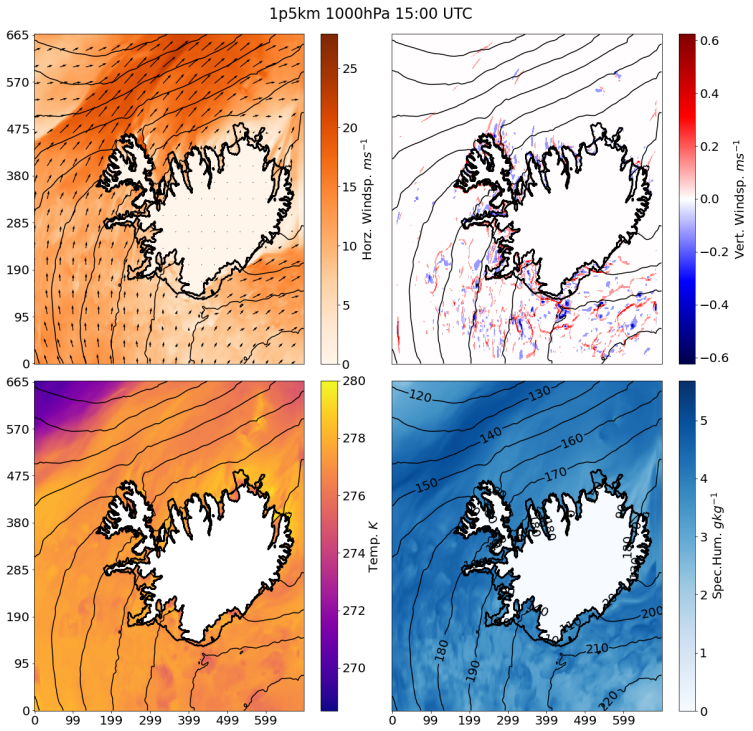

Figure 2.5: Map of Case 2 Regional Atmosphere model 1.5-km domain. Atmospheric state variables are shown at the 1000-hPa pressure surface at 15Z model time: horizontal wind speed (top left), upward wind speed (top right), air temperature (bottom left), and specific humidity (bottom right). Contours in each panel are geopotential height, and values in meters are labelled in specific humidity panel. Areas where surface altitude is intersected by the pressure surface are masked in white.

2.3.2 CASE 1

The model's synoptic conditions in Case 1 are dominated by a low-pressure system to the South of Iceland with strong cyclonic motion, and a weak pressure gradient over the Iceland-Greenland Sea region. Cool and dry air is drawn from this latter region and from Greenland, and the area of observation is dominated by northeasterly winds (Figure 2.7, top left). The most southern aircraft measurements may detect effects from the southern low, and the Keflavik soundings prove less useful, as the station is not situated directly downstream of the flow intersected by the aircraft in this case study. Case 1 represents a weaker flow state compared to Case 2. Inspecting the high resolution 0.5-km domain for this case in Figure 2.7 shows that

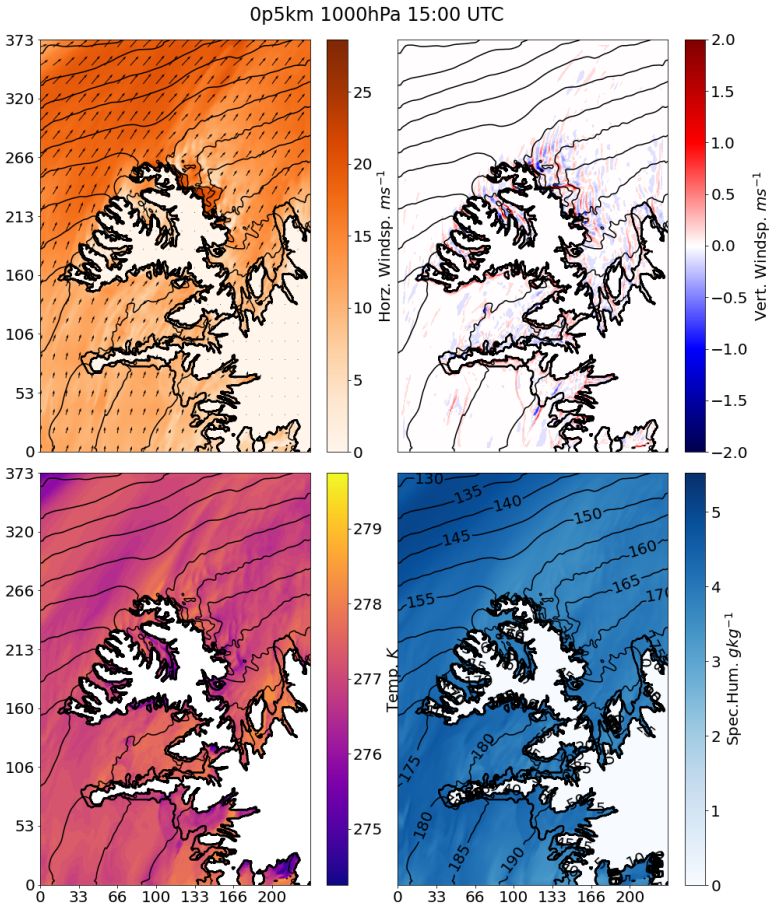

Figure 2.6: Map of Case 2 Regional Atmosphere model 0.5-km domain. Atmospheric state variables are shown at the 1000 hPa pressure surface at 15Z model time: horizontal wind speed (top left), upward wind speed (top right), air temperature (bottom left), and specific humidity (bottom right). Contours in each panel are geopotential height, and values in meters are labelled in specific humidity panel. Areas where surface altitude is intersected by the pressure surface are masked in white.

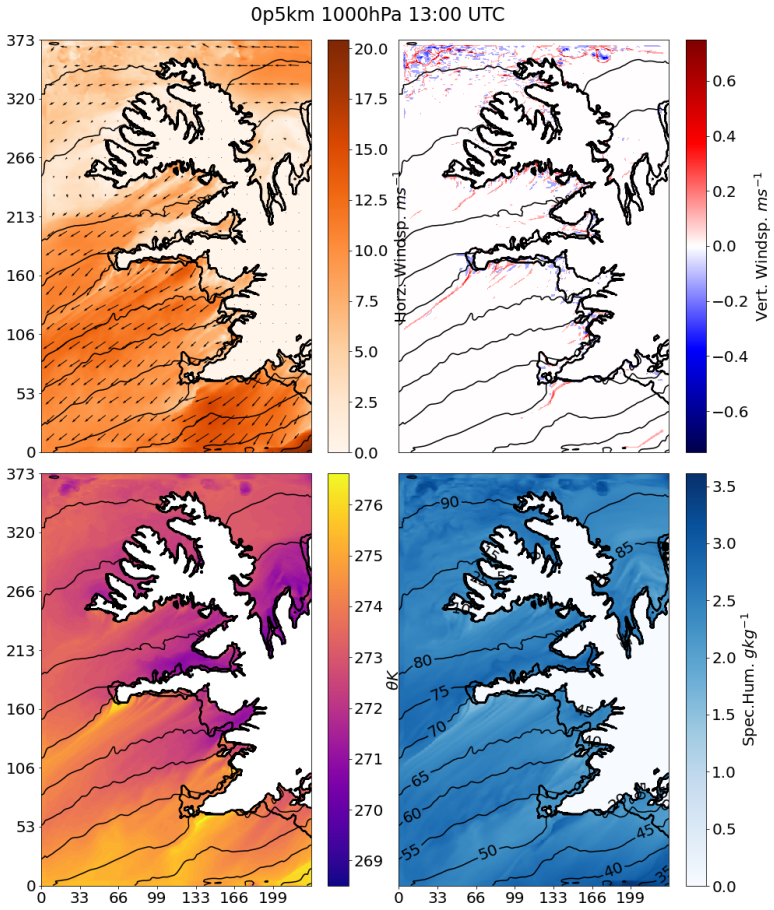

Figure 2.7: Case 1 Regional Atmosphere model 0.5-km domain. Atmospheric state variables are shown at the 1000hPa pressure surface at 13Z model time: horizontal wind speed (top left), upward wind speed (top right), air temperature (bottom left), and specific humidity (bottom right). Areas intersected by the pressure surface are masked in white.

maximum field magnitudes for horizontal and vertical wind speed, temperature, and specific humidity are below those seen in Figure 2.6, especially in the vertical velocity, w, field around the peninsula, where values of w are of order 1 m s^{-1} lower in the lee in Case 1 than in the lee in Case 2.

Finely resolved streams of air are seen in the horizontal wind speed, air temperature, and specific humidity fields originating at various points along the Snæsfellsnes Peninsula ridge (Figure 2.2), which correspond to gaps in the model orography (not shown), which is likely Foehn-like wind forming from gap flows. A

stronger wake feature is seen coming off the Snæsfellsjoekull (a volcano at the western tip of the peninsula, which is the highest peak in the ridge, Figure 2.2), with stronger warming effects, likely owing to the higher altitude and greater conical shape of the volcano, though that is difficult to confirm from this figure. Cool patches and a dense vertical velocity field north of the Westfjords may suggest precipitating cloud activity, while the southern cyclone is evident in the faster and warmer winds skirting Iceland's southern coast.

2.4 EVALUATION

2.4.1 VERTICAL PROFILES

It is reasonable to assume that the flow captured by the IGP 306 mission and by the ground-based stations in Case 2 is principally associated with the southerly flow seen in Section 2.3.1, within which the Keflavik soundings further upstream are situated. Unobstructed by any immediate orography to its south the Keflavik soundings provide a suitable location to observe undisturbed upwind conditions for Case 2. The highest resolution (0.5-km) could not be used as Keflavik and the profile flight leg lie just outside that domain, so we will show the profiles in the other two regional domains.

KEFLAVIK PROFILES

Before we apply our in-situ aircraft measurements to evaluate the UM's representation of complex flow processes in the lee of the mountains, we want to evaluate the upstream and downstream vertical structure of the modelled atmosphere against radiosonde and aircraft observations to establish a reference point for the model's performance; specifically, we want to know if any poor or good model performance near the mountain ranges corresponds to a similarly poor or good representation of the atmosphere upstream where we do not expect the mountains to have as much influence as in the lee.

Case 2's upwind Keflavik soundings, shown in Figure 2.8, provide the best approximations of undisturbed upstream orographic flow available to this study. The soundings characterise the ABL and have a strong inversion-like stable layer with a discontinuous vertical temperature gradient above 2 km altitude and increased flow

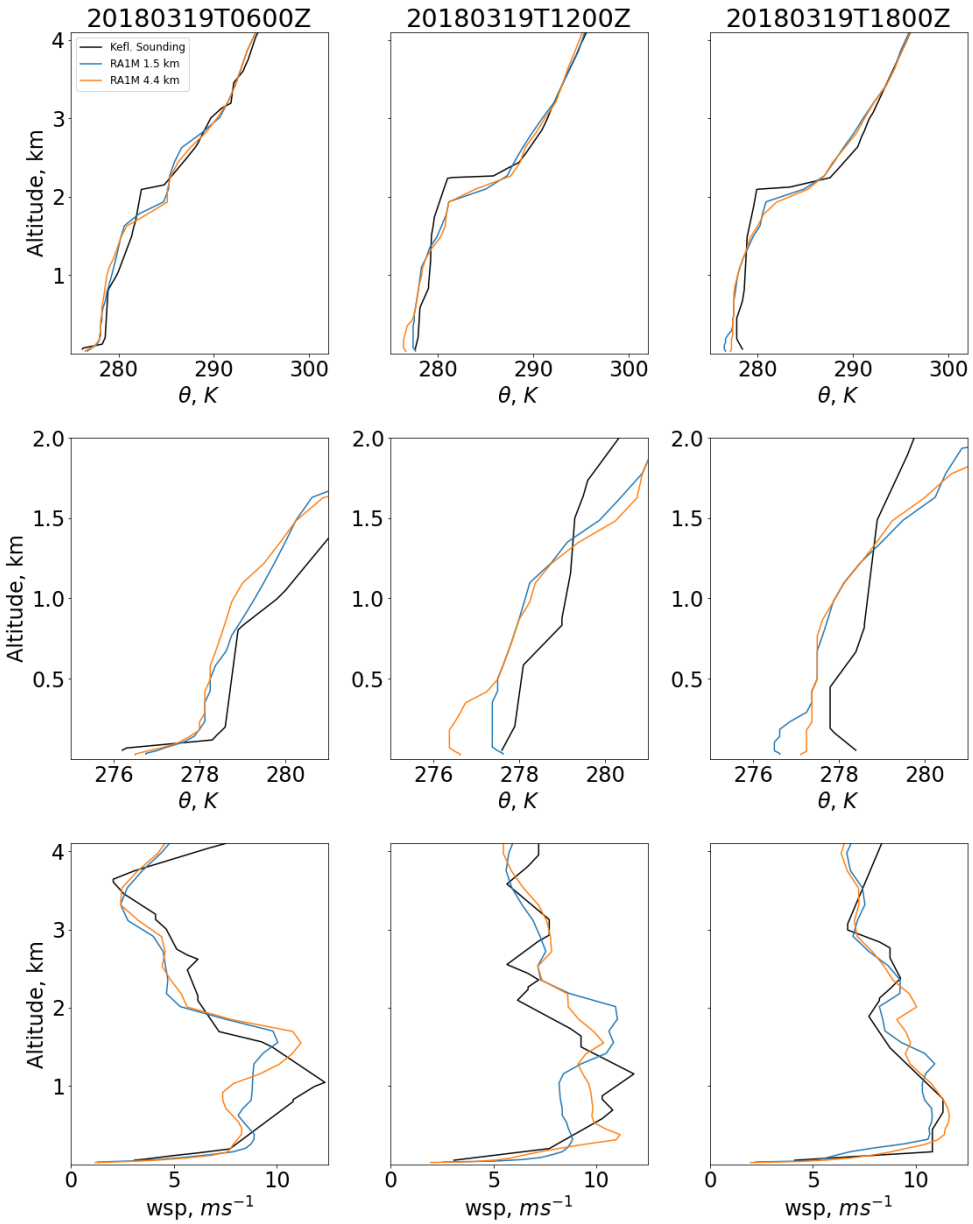

Figure 2.8: Case 2 upstream potential temperature (top two rows) and wind speed profiles (bottom row) from Keflavik radio sondes and matched 1.5-km and 4.4-km UM data on 19th March 2018.

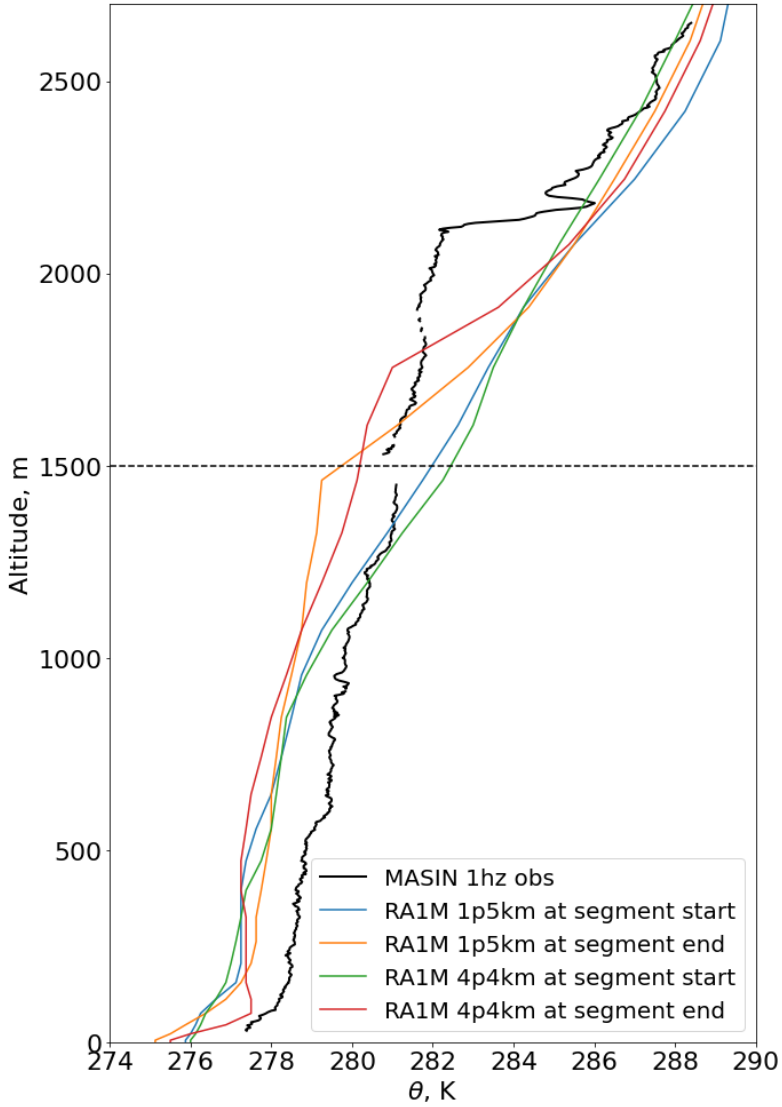

Figure 2.9: Case 2 downstream potential temperature profiles. Observations sourced from 1Hz flight data measured between 16:48 UTC and 17:03 UTC, model data columns taken at two horizontal coordinates corresponding to the grid points marking the beginning and end of the observed profile at the closest available output time step (17Z). 0.5-km simulation profiles are unavailable due to the profile' location outside the 0.5-km domain.

speed up to 12 m s^{-1} below the stable layer compared to roughly half of those values immediately above the ABL.

Despite greater deviation in the morning at 6Z forecast time, the regional model captures a high temperature gradient stable layer at a similar altitude, though it is weaker; rather than producing a sharp boundary, the model shows a smoother than observed transition forming a boundary about 400-500 m thick wherein the model overestimates the potential temperature (θ), while the model underestimates θ by up to 2 K below and directly above the stable layer before it converges with observations

at higher altitudes. The model generally underestimates wind speed within the ABL, but broadly captures the shape of the observed profile. The expectation taken from Figure 2.8 is that within the forecast a colder, yet similarly stratified than observed air mass will interact with the Icelandic peninsulas.

STABILITY AT CREST HEIGHT

The Brunt–Väisälä frequency N was evaluated from the Keflavik profiles by taking the mean potential temperature θ, and the change in potential temperature $d\theta$ and altitude dz to obtain $\frac{d\theta}{dz}$ for the interval in observations and model levels between 200 and 2000 m altitude above sea-level, to then compute N. The method will be repeated for the Froude number calculation in Section 2.4.4.

The N-measurements shown in Table 2.3, broadly support the above assumptions of the observed and forecast air mass, as in both model and observed cases, stability initially decreases after the morning, and then levels off during the afternoon. At each time UM values are larger, suggesting greater atmospheric stability in the model.

It is encouraging that both the 4.4-km and 1.5-km model resolutions are in close agreement, and this may suggest that the small temperature bias is sourced at the regional model's lateral boundary conditions, instead of a specific failing of the RA1M configuration.

Forecast time	N - observed	N - UM 1.5-km RA1M
06Z	0.0107±0.0001	0.0117±0.0011
12Z	0.0063±0.0003	0.0088±0.0001
18Z	0.0066±0.0006	0.0091±0.0001

Table 2.3: Buoyancy frequency calculations from Keflavik profiles for available times using an ABL representative sample in the 200-2000 m altitude interval. Units of N are s^{-1}, and uncertainties are statistically derived from one standard deviation in the sample.

AIRCRAFT ASCENT PROFILE

Similar to the Keflavik soundings, the final ascent, which took place from 16:48 UTC to 17:03 UTC at the end of the IGP 306 flight represents the best available source of a downstream profile for Case 2, despite part of the profile being horizontally obstructed by a small peninsula as seen in Figure 2.2, which means that the profile

cannot be considered to be purely affected by the flow over the Westfjords. With this in mind, model columns were taken at both the start (unobstructed) and end (obstructed) coordinates of the ascent from both the 1.5-km and 4.4-km domains, shown in Figure 2.9.

The observations show a strong discontinuity in the vertical temperature gradient at the same altitude and temperature as seen upstream, but the regional model's stable layer altitude has dropped down to about 1500 m. This value is clear in the obstructed profile, which shows a more stratified atmosphere, closer to the observations, than the unobstructed profiles, which show a smooth slope starting at 1 km altitude. All model profiles, however, show the same consistent underestimation in potential temperature of about 1-2 K within the ABL below 1 km, independent of resolution. As this bias was present far upstream, it appears that, while the model physics involved in the flow over the Westfjords has had a significant effect on the shape of the ABL, by reducing its height and potentially inducing strong mixing across its top, it did not work to recover the error in θ.

By the profiles alone we have so far found that the UM regional simulations capture the vertical structure of the atmosphere over most of the observed depth of the atmosphere reasonably well, with similar gradients in both temperature and wind speed, and maximum and minimum values in wind speed generally in agreement. A low-level θ-bias of 1-2 K exists below 1 km altitude and the strength, with possible consequences for turbulent heat flux in the lower ABL. The model also does not fully capture the strength and exact altitude of an observed atmospheric temperature inversion layer at 2 km altitude, which according to the findings in Vosper (2004) would produce a weaker gravity wave response. With these results in mind, we can now proceed to evaluating the modelled aloft and lee-side atmosphere using our in-situ aircraft observations.

2.4.2 FLIGHT DATA

As mentioned in Section 2.1.2, the availability of in-situ aircraft observations allows us to conduct a comprehensive and novel verification of the UM forecasts. In the previous section we evaluated the upstream and downstream profiles and general state of the atmosphere and found the first evidence of a low-level temperature bias,

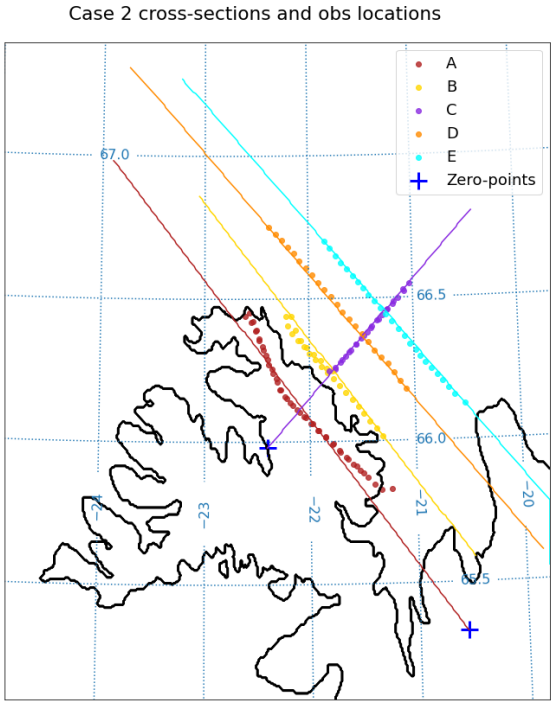

Figure 2.10: Selected IGP 306 (Case 2) flight legs (60s run-averaged point spacing) shown with corresponding cross-section locations (lines). The numerically ordered flight legs are organised into alphabetical groupings: legs 1 and 2 in A, legs 4-6 in B, legs 7-9 in C, leg 13 in D, and leg 15 in E. The zero-points on the x-axis in the vertical slices in Figures 2.11 and 2.12 are marked with blue crosses. Earth-grid latitude and longitude lines (dashed) are given with labelling in degrees.

but generally good agreement with in-situ radiosonde measurements and the aircraft profile at the end of the Case 2 flight. In this section we will look at the model performance above and in the lee of the mountain ranges in Case 1 and Case 2. We will also look in greater detail at distinct areas in the Case 2 domain, where aircraft observations are available: above the mountains, in the lower parts of the ABL in the lee, and further downstream across the height of the ABL. This allows us to not only assess the UM sub-km simulation's performance as a whole, but also to further constrain localised weaknesses and strengths in the UM's forecasting ability.

The IGP 306 flight can be split into several legs that represent a section of the flight generally flown in horizontally straight lines, some flown at constant altitude, and two saw-tooth patterns. A selection of flight legs is given in Figure 2.10, which are divided into five alphabetical groups based on regions made distinct by geographical location and flight patterns: two flight legs aloft of the mountains (A), several legs parallel to the ridge immediately in the lee (B), two legs along the wind direction (C), a downwind minimum safe altitude leg (D) and a downwind saw-tooth (E). However, other, minor,

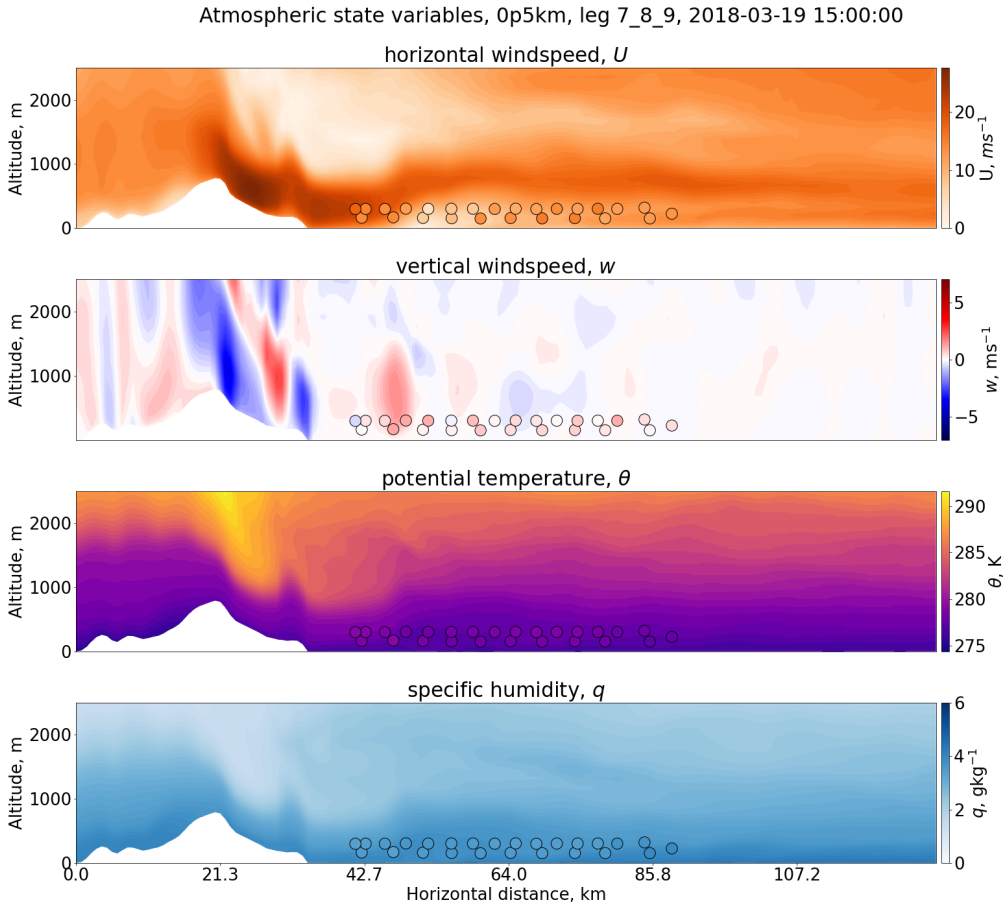

Figure 2.11: Group C along-wind slice showing model atmospheric state variables. Southern end is left, northern end right. Observations show grouping C (legs 7-9). 0-km on the x-axis is marked with a cross in Figure 2.10.

legs are present in the flight, and those are included in whole data set analyses.

EVALUATION OF ACROSS- AND ALONG-WIND SLICES

Model slices with corresponding observation points, are shown in Figures 2.11 and 2.12. Figure 2.11 shows a structure with the characteristics of a downslope windstorm forming underneath a hydraulic jump, a process described in Chapter 1. While the model captures a hydraulic jump evident in the observations the reattachment to the surface is too far downstream, which could imply that the windstorm and hydraulic jump seen in the UM may not be sufficiently resolved. Additionally, the difference between the observed temperature inversion and the modelled atmospheric stratification at mountain height discussed in Section 2.4.1 would lead to a weaker modelled gravity wave response (Vosper (2004)), which could contribute to the late surface reattachment. In Figure 2.12 model values

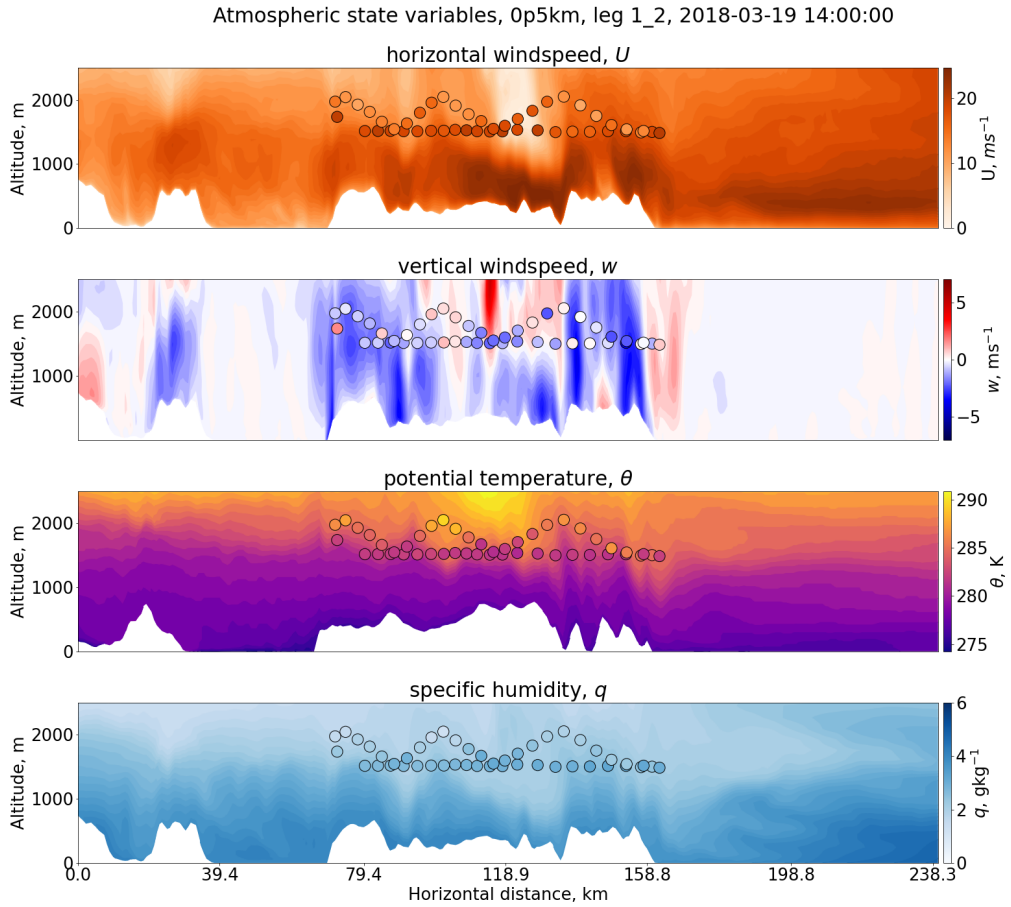

Figure 2.12: Group A cross-wind slice showing model atmospheric state variables. Southern end is left, northern end right. Observations show grouping A (legs 1 and 2). 0-km on the x-axis is marked with a cross in Figure 2.10.

underestimate the strength of the flow above the mountains, as if the storm was shallow, unlike in Figure 2.11. This is a consequence of the flight legs in grouping A (1 and 2) curving in the middle, while the cross-sections represent straight lines on the horizontal map, as seen in Figure 2.10. More likely, the values of the flight data for Group A correspond to the stronger, moist, and cooler air aloft of the mountain peak depicted in Figure 2.11.

The model also simulates a deep (2 km) moist layer across the domain depicted, with typical q values ranging 3-4 g kg^{-1} up to 2 km above sea level, and then rapidly dropping to below 2 g kg^{-1} above the ABL, which agrees with the aircraft observations in the lower ABL. Higher than modelled humidity observations above the mountain ridge in Figure 2.13 and 2.13 suggest that the observed moist layer is potentially deeper than the one modelled. A deep moist layer coinciding with high downslope

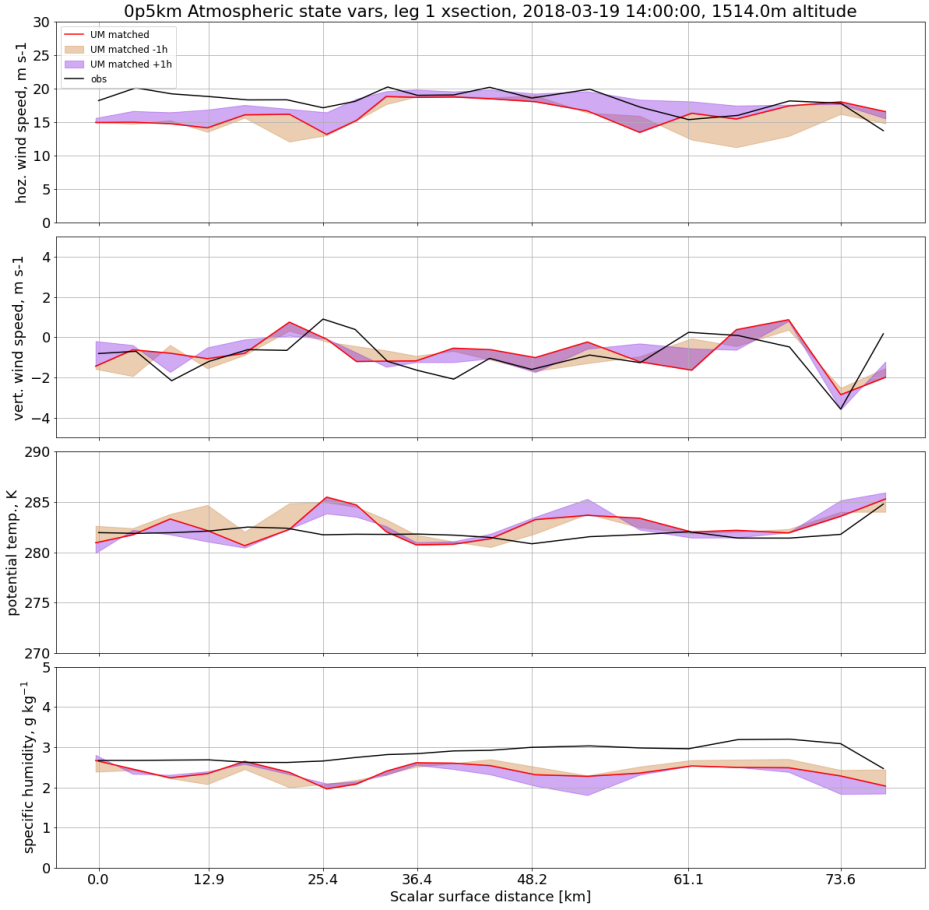

Figure 2.13: Spatial series of leg 1 (in Group A) observations (black) and matched interpolated model 0.5km measurements for atmospheric state variables: horizontal wind speed (1st/top), upward wind speed (2nd), potential temperature (3rd), and specific humidity (4th/bottom). Shaded areas represent model output one hour ahead (khaki), and after (purple) the selected output time.

wind speeds is consistent with the observations and linear wave modelling in Jiang & Doyle (2009).

When using model data interpolated from the 3D model field onto the coordinates of the observation points, shown in Figures 2.13 and 2.14 for leg 1 (in A) and 7 (in C) respectively, producing a matched dataset, the model's performance appears to confirm this point, showing a closer agreement with observed values for horizontal and vertical wind speed and θ. It is also important to consider the transience of the wind event in the model, as demonstrated by the shading in Figures 2.13 and 2.14; the

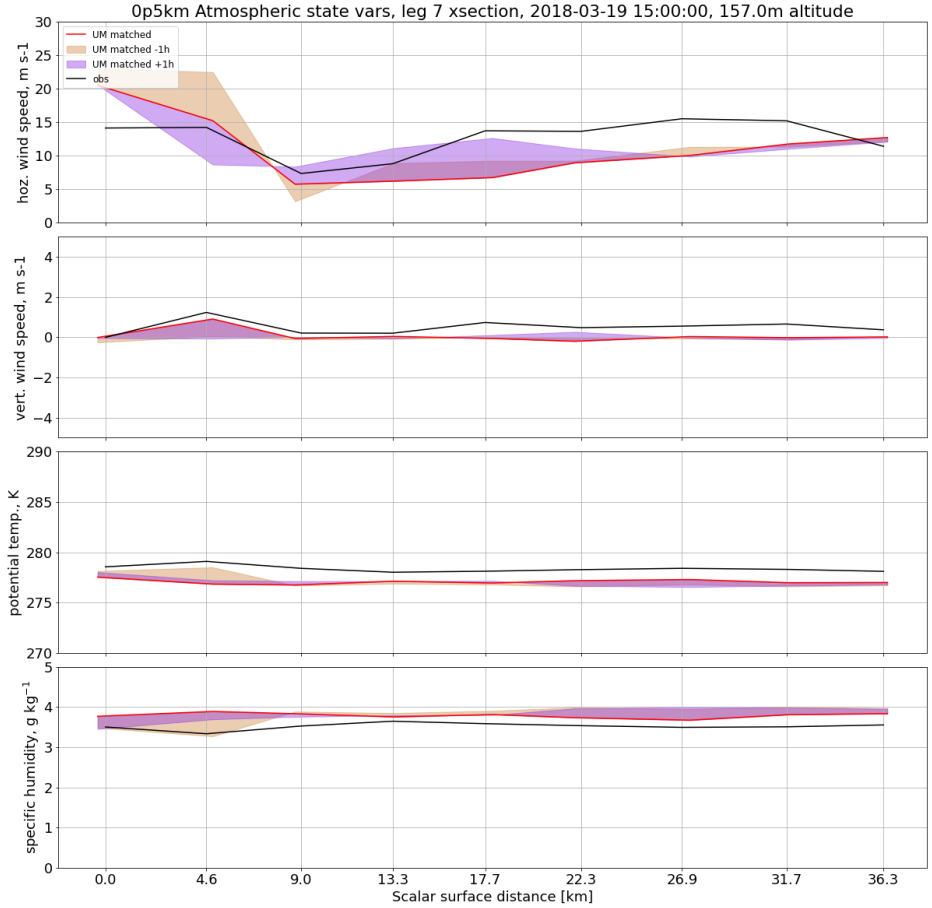

Figure 2.14: Spatial series of leg 7 (in Group C) observations (black) and matched interpolated 0.5km model measurements for atmospheric state variables: horizontal wind speed (1st/top), upward wind speed (2nd), potential temperature (3rd), and specific humidity (4th/bottom). Shaded areas represent model output one hour ahead (khaki), and after (purple) the selected output time.

flow intensifies aloft, decelerates in the lee closest to the ridge, and accelerates further out over the sea, meaning the model would be in significantly closer agreement with observations 1 hour later in this instance.

LOW-LEVEL BIASES IN TEMPERATURE AND HUMIDITY

The model shows more horizontal variation in θ than observed, and still underestimates specific humidity by an order of 1 g kg^{-1} aloft of the mountain range. In the immediate lee-side the difference in horizontal wind speed is more contrasted,

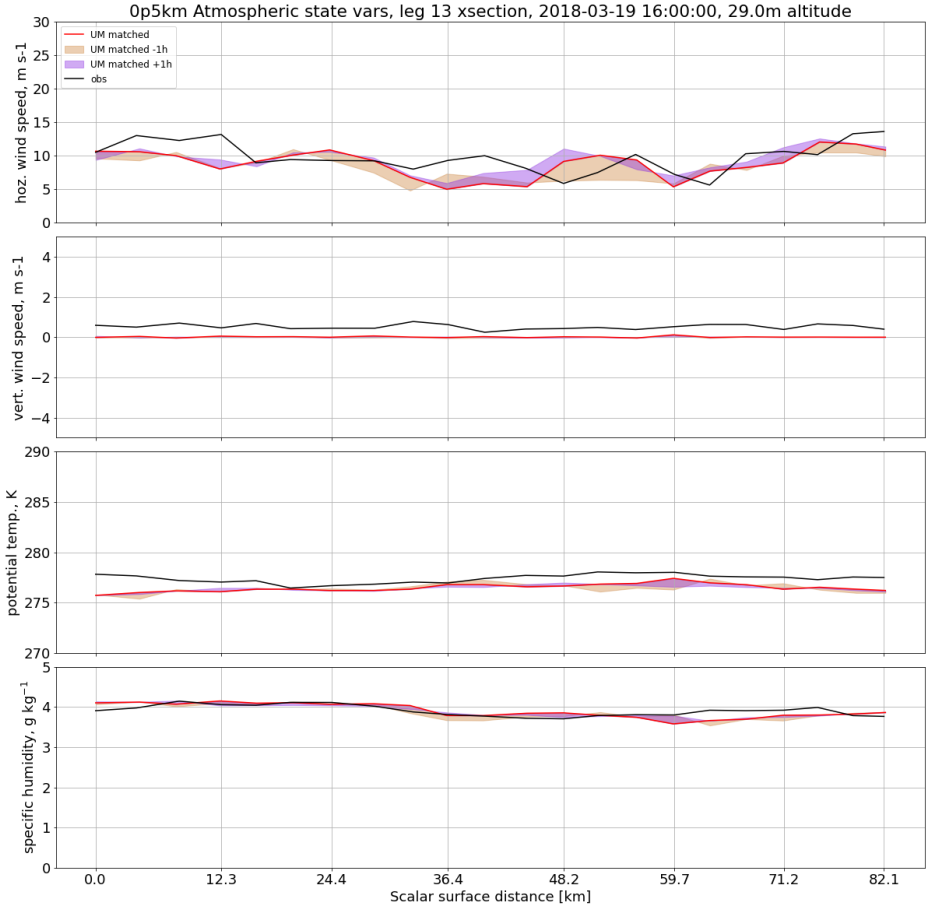

Figure 2.15: Spatial series of leg 13 (D) observations (black) and matched interpolated 0.5km model measurements for atmospheric state variables: horizontal wind speed (1st/top), upward wind speed (2nd), potential temperature (3rd), and specific humidity (4th/bottom). Shaded areas represent model output one hour ahead (khaki), and after (purple) the selected output time.

with the model underestimating low-level speeds by up to 5 m s^{-1}, as shown in Figure 2.11. Vertical wind speed is also underestimated, but that is not unusual as vertical wind speed will go to zero as we approach a flat surface. The model underestimates it in this case, because while in the real atmosphere vertical wind speed will drop continuously, while the model fields are given on fields at discreet levels, which may not capture the gradual change as effectively. Potential temperature is consistently underestimated by about 1-2 K, and there is an overestimation in specific humidity by about 0.2-0.5 g kg^{-1}.

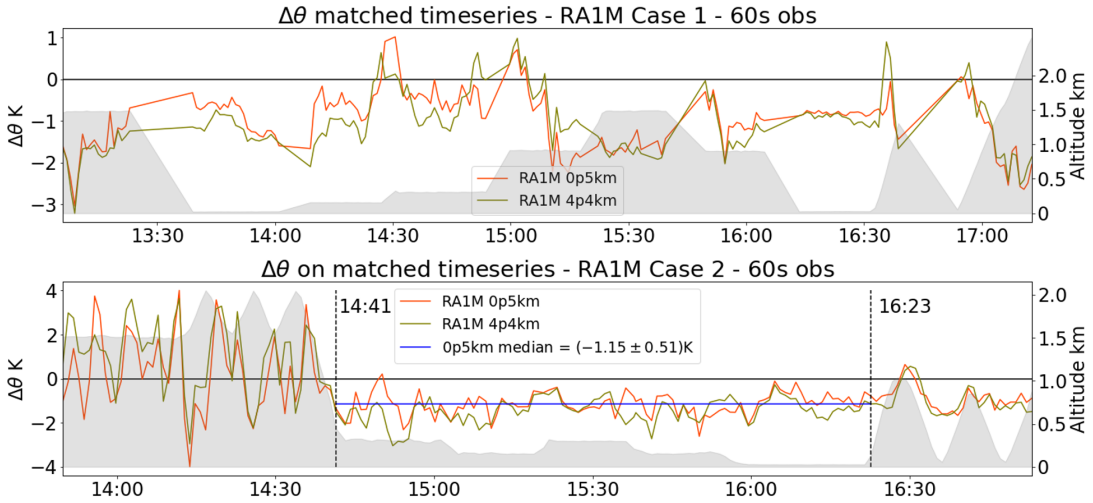

Figure 2.16: Matched time-series of difference between model and observed 60s run-averaged potential temperature for two model resolutions, 0.5km (orange)and 4.4km (green) horizontal grid-spacing. Grey shaded areas represent altitude of aircraft at the time.The black line at theta = 0 represents perfect correlation. In Case 2 (bottom panel) an interval characteristic for low flight altitude was defined, and median of delta theta was taken (blue line); Uncertainty given is one standard deviation. the vertical dashed lines mark the section of the Case 2 flight where the aircraft flew below 500 m. This segment is sampled to derived the median bias given in the legend. The left-hand axis scale gives θ-bias and the right-hand scale gives altitude.

This bias in θ is consistent with the up- and downstream profiles and appears to be maintained within the lower parts of the ABL despite strong orographic flow activity occurring upstream of the lee-side flight legs, such as a downslope windstorm on the nearby lee-side slope, which will be revisited in the next chapter. Group A doesn't see this bias in θ, which could be due to those legs taking place at the upper part of the ABL or above at 1500 m altitude.

The lack of model-observation agreement observed at this altitude is dominated by horizontal variation in θ, which likely is influenced by the flow processes due to the complex orography below and upstream. Horizontal wind speed in Figure 2.13 shows a bias reaching 5 m s^{-1} at 14Z model time, however better agreement is seen with the model output one hour later, suggesting that temporal variability also affects the model performance. Further downstream, legs 13 (D), shown in Figures 2.15, and 15 (E) (not shown), still capture a consistent θ-bias, even when agreement in humidity levels, and horizontal wind speed somewhat improves.

In Figure 2.16 we took the difference between the 60-s run-averaged observation points and the nearest-neighbour interpolated model grid-point. When considering

the IGP 306 flight as a whole in Figure 2.16, the presence of the θ-bias within the ABL becomes more apparent: measurements taken at and above 1 km altitude show no consistent offset, while the median of the deviation of the 0.5-km resolution regional model in potential temperature from observed values, $\delta\theta$, measured over legs at altitudes below 500 m in the lee of the Westfjords, is equal to (-1.15 ± 0.51) K.

During Case 1, $\delta\theta$ is predominantly negative as well, suggesting that the bias is not necessarily due to the atmospheric conditions, which differ between the two cases, during Case 2, or due to a specific upstream synoptic event, such as the high-pressure system to the south of Iceland during Case 2 or the weak pressure gradient over Iceland during Case 1. Furthermore, the regional model at the 4.4-km resolution agrees with the 0.5-km results and shows similar levels of bias. It is possible that by coincidence the modelled synoptic systems during both cases lead to an over-cooling of the lowest parts of the atmosphere.

SUMMARISING EVALUATION AGAINST AIRCRAFT OBSERVATIONS

In Figure 2.17 the evaluation results of both cases are summarised. Each case shows a broad spread in horizontal and vertical wind speed for both model output and observations, though Case 1 is more clustered. Yet neither case shows any particular bias in horizontal winds; vertical velocities are slightly underestimated in the UM for upward flow directions, but grid-scale vertical motion is particularly small in Case 1, so deviations may be less significant. No major differences between above-mountain and lee-side measurements are found, apart from wind speeds being slightly higher aloft.

The temperature bias discussed above is noticeable for lee-side measurements for both cases, corresponding to data points in the lower ABL, but only also present for above-mountain measurements in Case 1; for Case 2, the bias is reversed at higher altitudes, which could be attributed to both days involving different synoptic air masses, which coincidentally behave similarly in the lower ABL, but apart from that have distinct attributes. In Case 2 specific humidity has greater spread, and shows a model underestimation ranging from 0 to 1 g kg^{-1} for points above mountains, and the reverse in the lee. Compared to Case 2, Case 1 shows better agreement for humidity in the lee, with a distinct positive bias aloft, further adding evidence that both cases represent distinct air masses. Overall, the regional model showed consistently greater

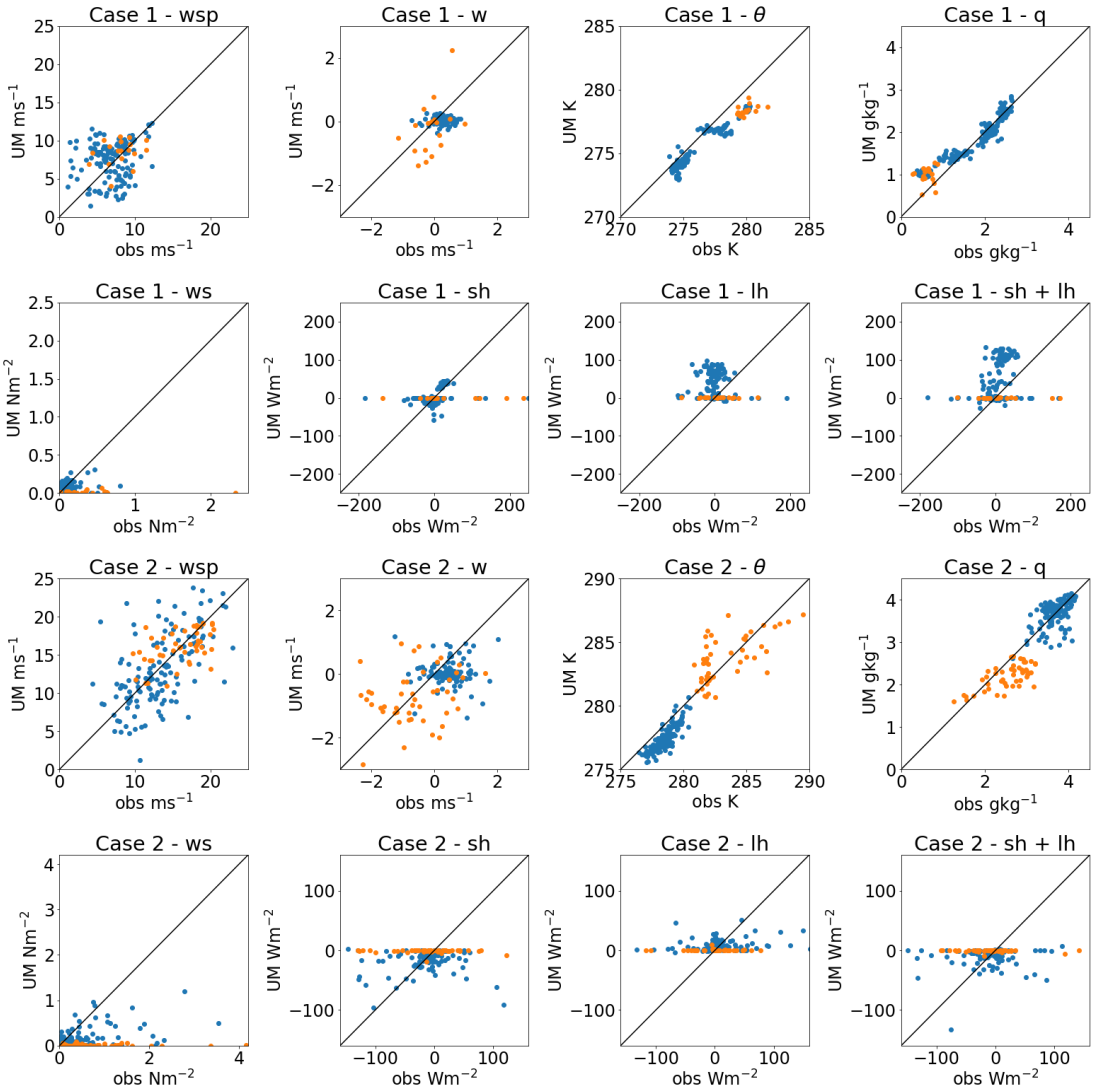

Figure 2.17: IGP 60s run-averaged observations vs.UM 0.5km matched interpolated values for atmospheric state and flux diagnostics. Data sets are split into Case 1 (top two rows) and Case 2 (bottom two rows) as well as measurements taken above respective mountain ridges (orange) and in the lee of the mountains (blue). A line of perfect correlation (black) is given for visual assistance. The showcased variables are horizontal wind speed wsp, vertical wind speed w, potential temperature θ, specific humidity q, wind stress/momentum flux ws, sensible heat-flux sh and latent heat-flux lh.

agreement for atmospheric state variables in Case 1 compared to Case 2.

The regional model demonstrated significant shortcomings in its representation of turbulent fluxes; while observations in both cases show a broad distribution nearly symmetric around zero for sensible heat, latent heat, and net flux, the model firstly underestimates flux amplitudes, and secondly depicts an asymmetric distribution. In Case 2 sensible heat flux is predominantly negative (downwards), while latent heat flux mirrors with an upward bias. Net heat flux is dominated by sensible heat in Case 2, and thus directed mostly downwards in the model. Figure 2.17 does show sensible heat flux being more underestimated in the lee of the orography compared to above the mountains in case 2. This may be linked to the under-representation of vertical wind speed at low levels in the model (e.g. Figure 2.15), since heat flux is related to perturbations in vertical wind speed. Moreover, the model captures trivial flux values in above-mountain legs and shows greater spread in the lee.

Case 1 is set apart by a noticeable clustering of sensible- and latent heat flux for lee-side measurements; aloft values behave as they do in Case 2, while lee-side measurements cluster closer to the line of perfect correlation, despite a distinct negative bias. This suggests that the regional model performed better in its representation of heat flux in Case 1. Furthermore, in contradiction to Case 2, Case 1 net heat flux is dominated by latent heat flux, as evidenced by the similarity in the clustering between latent- and net heat flux. The difference in Case 1 and Case 2 latent heat fluxes can be explained using Equation 2.2 (adapted from Equation 9.19b in Wallace & Hobbs (2006)), a bulk parametrisation of latent heat flux Q_{LHF}:

$$Q_{LHF} = C_E L_v \rho |V| (q_{sat}(T_s) - q_{air}) \tag{2.2}$$

where C_E is the dimensionless bulk transfer coefficient, L_v is the latent heat of vaporisation, ρ is air density, $|V|$ is 10-m wind speed, $q_{sat}(T_s)$ is the saturation specific humidity measured at sea-surface, or *skin*, temperature T_s, and q_{air} is the specific humidity measured in the air. For Case 1, where most values of q_{air} are smaller than for Case 2, the $(q_{sat}(T_s) - q_{air})$ is greater, so Case 1 would measure higher latent heat flux.

Case 1 shows little momentum flux (ws) in both observations and model, which may lead to a misrepresentation of better performance compared to Case 2, due to stronger clustering around low values of stress. Despite that, both Case 1 and 2 show

that the model generally underestimates wind stress, with a mildly wider distribution of model values in the lee. At this point it is important to note that the observed fluxes were estimated using run-averaging of 60s segments of the flight trajectory and then calculating covariances over reach run, which corresponds to a spatial length of roughly 4 km.

Since the flux diagnostics from the UM similarly derive grid-point scale net fluxes from sub-grid scale perturbations, it can be seen that the observations would represent grid-points of horizontal spacing of order 4km best, and that smaller grid-spacing will account for increasingly fewer sub-grid perturbations, where instead larger scale perturbations such as jets, up- and down drafts, and waves are better resolved and might dominate heat and momentum transport. It is for that reason that gross and subtle disagreements between observations and model diagnostics should be considered with care.

2.4.3 GROUND-BASED MEASUREMENTS

The apparently wide-spread temperature bias in the lower ABL warrants further investigation; at this point we do not know if the bias is produced in the regional atmosphere model or sourced at the lateral boundary conditions from the global driving model. We also do not know if this bias is situated at a low-level but aloft in the atmosphere, or if it extends fully to the surface, and would therefore be noticeable in the model 1.5-m temperature field. A bias of 1-2 K in the 1.5-m temperature fields could have a systematic effect on surface flux parametrisations, although those parametrisations will not be investigated in this chapter, so any real implications are unknown. Chapter 3 will look at surface heat flux diagnostics, and provide potential evidence for the impact of changes in 1.5-m temperature on surface heat flux in the model.

Measurements from Iceland's numerous ground-based weather stations corroborate the previous sections's findings, by showing a clear underestimation of 1.5-m air temperature across all four Case 2 sample stations by the 0.5-km regional model, as shown in Figure 2.18. The bias remained significant after the model surface temperature was pseudo-adiabatically adjusted based on the difference in altitude between the model surface altitude and the ground-station actual altitude. A bias,

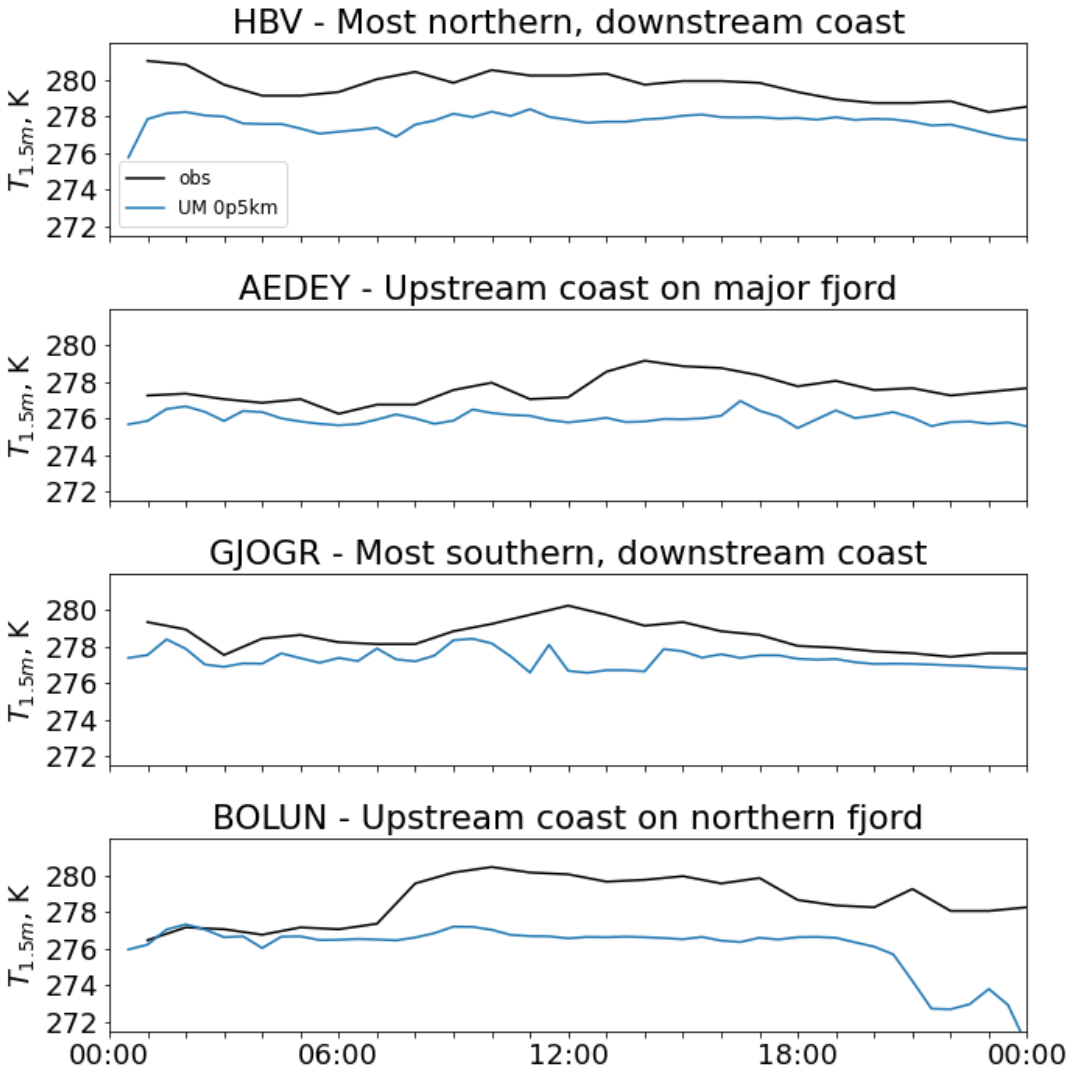

Figure 2.18: Case 2, 1.5-m air temperature $T_{1.5m}$ time series across forecast period with measurements from four representative automated atmospheric measurements (black) and corresponding nearest neighbour 0.5km UM surface diagnostics (blue).

though more variable, is also seen in ground-stations on the Snæsfellsnes Peninsula during Case 1 (not shown). Ground-based data also shows a positive moisture bias (Figure 2.20) roughly mirroring the trend in temperature, while the model 10-m wind speed was more variable, but was similar to the observations in magnitude.

COMPARISON WITH THE GLOBAL DRIVING MODEL

To address the question of the source of the temperature bias, the ground-station data is also compared to the surface output of the global driving model shown in Figure 2.19, where instead of using a small sample of stations, a total of 44 monitoring

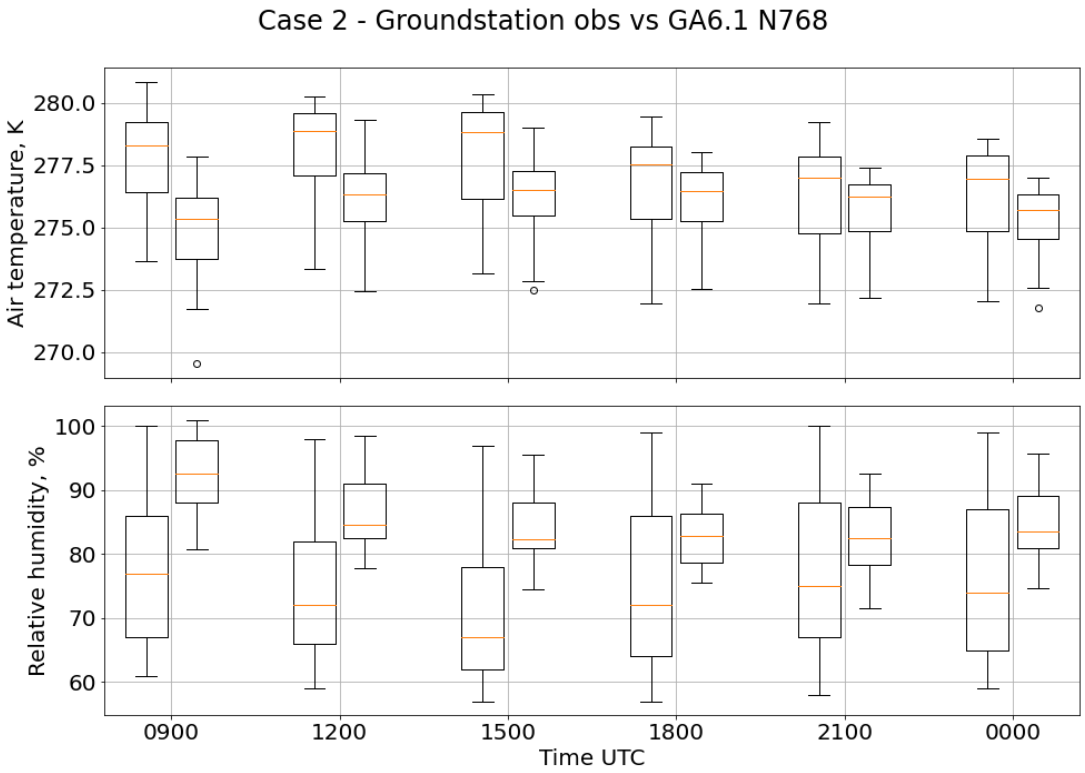

Figure 2.19: Boxplot analysis of surface variables across forecast time (starting at 9Z) of 44 ground-based atmospheric monitoring stations in NW Iceland. Observed values are the left of each pair, nearest neighbour UM measurements are the right-hand box of each pair. The boxes contain 50% of the data points, while 95% of the data is contained within the whiskers. The median of each set is the orange line.

stations in Iceland's North-West are used in the analysis to obtain a more domain-spanning picture of the driving model's performance. Between 9Z of the 19th and midnight of the 20th March the temperature bias at the surface reduces from a median of approximately 3 K to 1 K and remains significant throughout the afternoon hours. At 21Z in the evening the deviation in the medians did reach a trough of about 0.5 K. The range of the observations is generally larger than the range of the model grid-point values, apart from singular outliers.

Between 9Z and 15Z the range in temperature in the model reaches maxima and minima noticeably below their observed counterparts. While the lower observed measurements become cooler than the model from 18Z onward, the model does not give values as high as the observations. The relative humidity (RH) measurements reflect the temperature bias, by showing a positive bias. This RH bias in the medians between 44 weather stations and the global driving model agrees with the bias in the

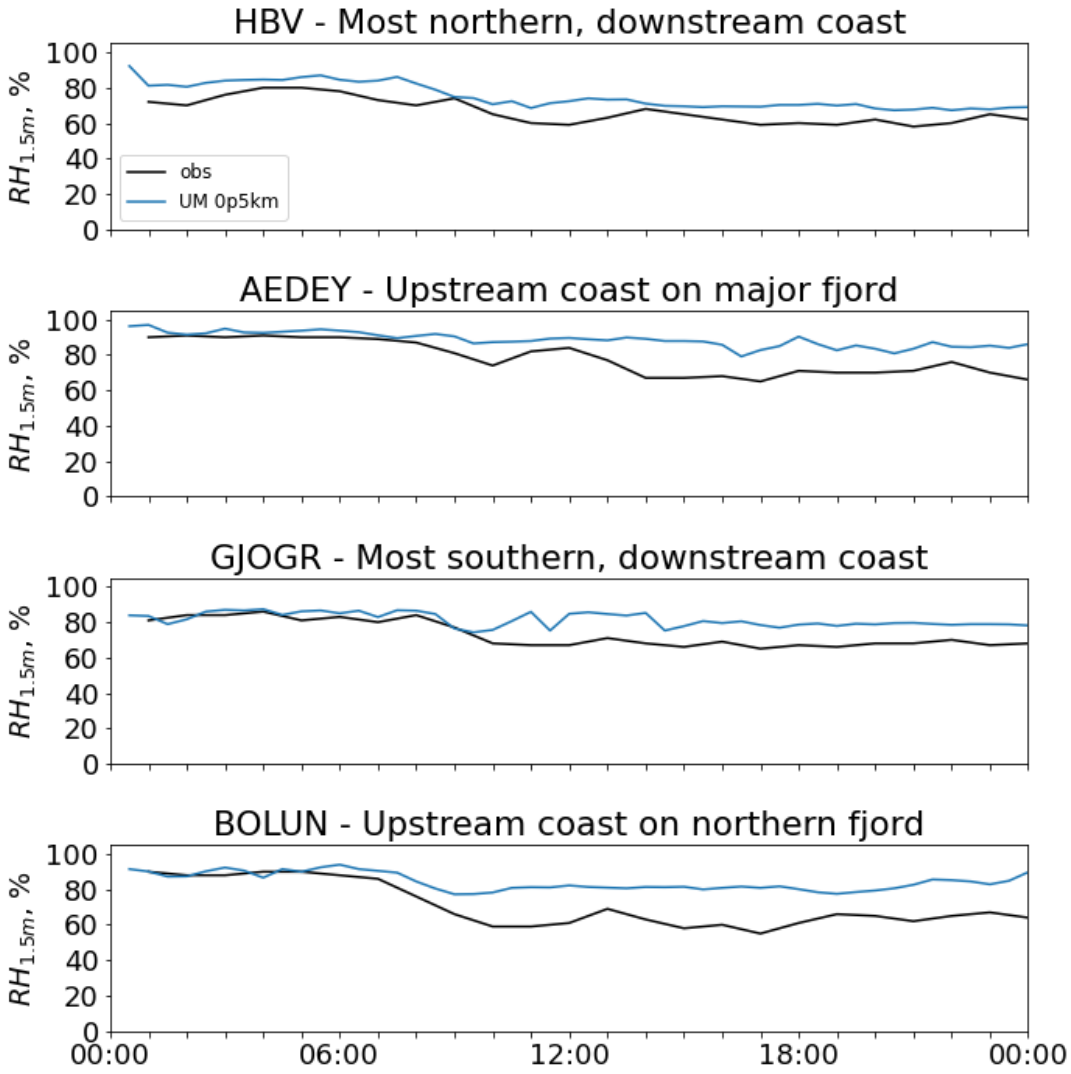

Figure 2.20: Case 2 1.5-m relative humidity $RH_{1.5m}$ time series across forecast period with measurements from four representative automated atmospheric measurements (black) and corresponding nearest neighbour 0.5km UM surface diagnostics (blue).

0.5-km regional model given in Figure 2.20, where RH values can differ by 20 % and more for the AEDEY and BOLUN stations in the afternoon. An RH-bias here would be driven by both the θ-bias and the bias in specific humidity; cooler air that cannot hold as much moisture and higher moisture concentrations both increase RH. As some of the model RH values approach 100 % a potential consequence of the biases is that the model incorrectly forecasts increased precipitation, cloud formation, or fog.

This presents evidence that the temperature bias seen in the regional model data is sourced in the global driving model. As the bias in the median appears similar to the bias values in the 0.5-km, 1.5-km, and 4.4-km resolution regional models, it

also suggests that it is likely there are no processes unique to the regional model that might amplify or correct this error. We therefore conclude that the effect is not inherent to the modelled orographic processes, resolved or parametrised, firstly due to its universal presence across the domain, as shown by the flight data and upstream- and downstream profiles, and secondly due to the universal presence of the θ bias across all regional and global model forecasts. Since it cannot be directly attributed to effects due to the orography, in future chapters orographic flow features can be studied confidently with respect to potential temperature, with the θ-bias within the lower ABL kept in mind when a system or feature is studied through sensitivity tests in concert with observations, for example in cases of lee-side Foehn-warming.

The question remains if this bias in the lower ABL might influence the turbulent exchanges in the ABL, and it can be addressed by returning to the profiles in Figures 2.8 and 2.9, where below 1 km altitude the profiles are mostly parallel with the observations, despite the bias, suggesting that the model atmosphere is similarly stable in those layers, further supported by the results in Table 2.3.

Model biases in turbulent fluxes are expected above 1 km altitude, owing to model biases in temperature gradients. More significantly the absence of a well defined inversion would have effects on orographic flows, particularly the different types of lee-waves and gap flows (Gaberšek & Durran (2004); Vosper (2004)), although the presence of a strong stable layer aloft is sufficient for windstorm generation (Smith (1985); Durran (1986); Jackson *et al.* (2013)). Considering stratification and atmospheric stability, despite the lower levels' temperature bias, the model does not represent the observed atmospheric inversion well, with differences between model and observed profiles above 2 km exceeding 5 K (Figure 2.8).

2.4.4 FROUDE NUMBER COMPARISON

The regional model at 0.5-km resolution was in closer agreement with aircraft observations in Case 1 than in Case 2, although the cause of this is difficult to know; we know that Case 2 has more complex weather patterns in the vicinity of the flight, such as a downslope windstorm, which may be influencing forecast fidelity if not modelled correctly. Case 2 also demonstrated a significantly broader distribution in measurements for most diagnostics, reiterating the complex nature of the flow

present, and the differences in air mass properties seen in both cases.

To add to the above considerations, a rough evaluation of the general flow conditions in Case 2 was performed by calculating the Froude number, using Equation 1.1, from the Keflavik profiles and using a representative mountain height of 1000 m, which corresponds to the order of magnitude of the highest peaks found in the Westfjords most eastern ridge, with the results given in Table 2.4. N was evaluated by first measuring the θ-gradient $\frac{d\theta}{dz}$ from available points within the 200 m to 2000 m altitude interval, where the change in θ and change in altitude z are taken from measurement points or model levels within he interval, to get $\frac{d\theta}{dz}$. This height interval was selected to avoid the temperature discontinuity at above 2000 m and the lowest parts of the ABL, and then computed using Equation 2.3 from Wallace & Hobbs (2006):

$$N = \sqrt{\frac{g}{\theta}\frac{d\theta}{dz}} \tag{2.3}$$

where g is standard gravity. In this case θ will be taken as the mean potential temperature in the altitude interval. The observed flow's Froude number increase from close to 1 where a transition from sub-critical flow to super-critical flow occurs (Ólafsson & Bougeault (1996); Smith (1980)), implying that the flow conditions of the day progress into an increasingly linear regime. In this process the observations diverge from the model value of Fr, which remains close to unity, where the kinetic energy of an air parcel is roughly balanced with the additional gravitational potential energy need to overcome the mountain barrier, and a gravitational wave can be generated as the air will try to recover to its original state (Jackson *et al.* (2013)).

Smith (1980) and Ólafsson & Bougeault (1996) establish that flow under small ($Fr \leq 1$) upstream Froude numbers (or high Nh/U), meaning non-linear flow, tends to form stagnant zones with wave breaking aloft of downwind slopes and flow splitting upstream, with wave breaking also being found at higher Fr-values (or low values of the non-dimensional mountain height, $\hat{h}$), which is consistent with the above mountain flow seen in Figure 2.11, although flow splitting is difficult to discern here due to the broad ridge nature of the mountains and is also not clear in Figure 2.11, which seems to show air flowing directly into the orography with noticeable upward wind speeds on upwind slopes.

Furthermore, high Froude numbers are usually accompanied by stationary lee-waves and flow detaching into turbulent structures such as rotors, while for

decreasing Froude numbers the flow would transition into a non-linear regime with hydraulic jumps a main feature at Froude numbers approximating unity (Sheridan & Vosper (2006); Vosper (2004); Jackson *et al.* (2013)). The latter is visible in the model flow shown in Figure 2.11, showing agreement with theory given the Froude numbers calculated from model profiles.

Potential overturning is also visible in the isentropes in Figure 2.11 in the second deeper wave-breaking zone aloft. The circumstances of Case 2 are complex, and other processes influence the flow, such as the complex and broadly distributed orography of the Westfjords, which is far from an isolated mountain system, and the non-ideal behaviour of different air masses on a synoptic scale with interactions occurring in the vicinity of the peninsula.

The flow regime predicted by the observed Keflavik profiles may also interact with gaps in the mountain ridge, for which the mountain height is lower than the peak, and may or may not be well resolved in the model topography, to effectively spill into the lee-side at lower altitudes and form complex turbulent structures, eddies, and induce faster jet-like wind speeds near the surface, which could be one explanation for the faster-than-model observed wind speeds in Figures 2.11 and 2.14.

Forecast time	Fr - observed	Fr - UM 1.5-km RA1M
06Z	1.07±0.06	0.76±0.08
12Z	1.71±0.12	1.01±0.11
18Z	1.61±0.22	1.14±0.05

Table 2.4: Case 2 Froude number calculations from Keflavik profiles for available times for a given representative mountain height of 1000m. In the Fr calculation the values from Table 2.3 were used with a mean sample of U in the 500-1500 m interval centered on h, to capture the speed of the flow incident on the ridge crest most effectively, while the interval used for N remains 200-2000 m to best capture the mean pseudo-adiabatic lapse rate in the atmospheric boundary layer.

Figure 2.21: Case 2 mean biases for horizontal wind speed U (top), potential temperature θ (center), and specific humidity q (bottom). Results for 0.5-km (blue), 1.5-km (orange), and 4.4-km (green) in the five geographically informed data groupings illustrated in Figure 2.10 are shown. Biases are defined point-wise by $Z_{UM} - Z_{obs}$, for a quantity Z.

2.4.5 RESOLUTION SENSITIVITY

MODEL SENSITIVITY TO RESOLUTION

The final aspect of this evaluation to discuss is the model's sensitivity to resolution. In the next chapter we will see a strong divergence in the case study downslope windstorm representation between the different model resolutions, and assessing the comparative model performance of all regional forecasts with respect to observations will help inform the results of the case study. Analysing the resolution sensitivity will also help us justify the use of the 0.5-km forecast as a control simulation in Chapter 3 and 4 instead of the computationally cheaper 4.4-km or 1.5-km forecasts, and therefore fulfil the final aim of this chapter set out in Section 2.1: to establish the UM 0.5-km regional simulation as a suitable control simulation for our case study investigation of a strong downslope wind event in Chapter 3.

Mean and root-mean-square (RMS) biases for selected atmospheric state

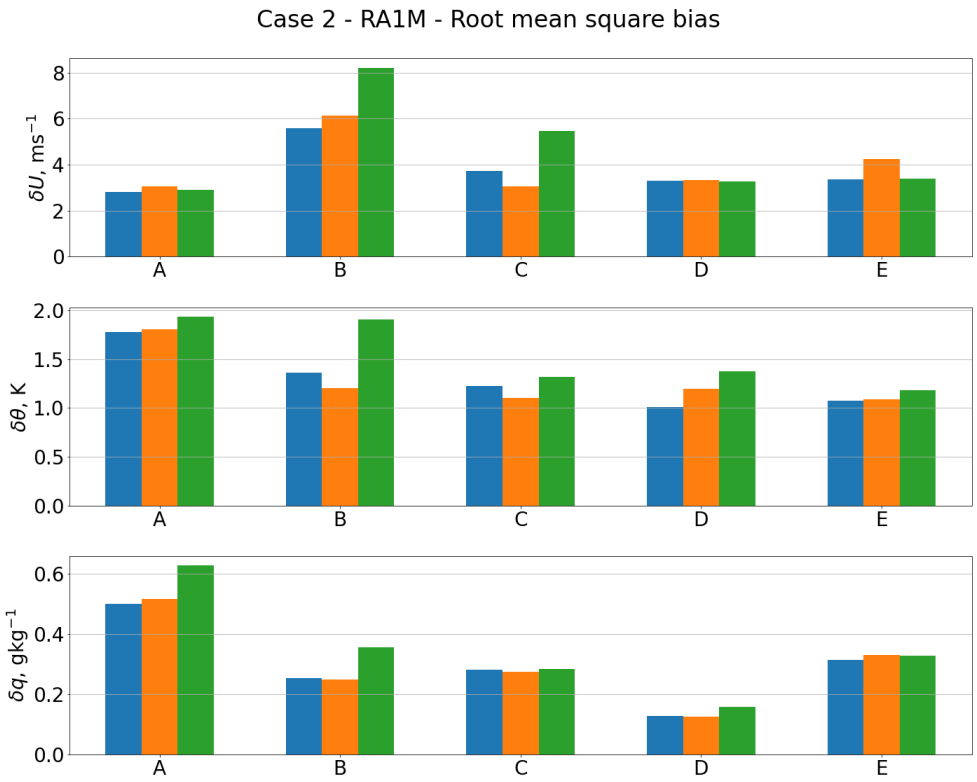

Figure 2.22: Case 2 root-mean-square biases for horizontal wind speed U (top), potential temperature θ (center), and specific humidity q (bottom). Results for 0.5-km (blue), 1.5-km (orange), and 4.4-km (green) in the five geographically informed data groupings illustrated in Figure 2.10 are shown. Biases are defined point-wise by $Z_{UM} - Z_{obs}$, for a quantity Z.

variables have been calculated using the Case 2 60s run-averaged flight data and are shown in Figures 2.21 and 2.22 respectively. Resolution sensitivity according to mean bias varies greatly with geographical location and variable, but changes more subtly for RMS. Overall 0.5-km is the best for performance, but does not do so consistently, for example in Group C 1.5-km mostly produces the lowest mean and RMS biases for all variables out of the three resolutions, except for mean wind speed bias.

4.4-km produces the largest biases across almost all groups and variables. RMS biases are largely consistent across resolution for groups A, D and E. Some of the largest differences in mean and RMS biases are seen for A, B and C particularly for θ at B and U at C, implying that low-level lee-side flow close to the mountain (e.g. within 50 km of slope base) in Case 2 is more sensitive to resolution than further downstream and above-mountain flow.

Mean horizontal wind speed U appears to be well estimated aloft for all resolutions, and is less accurately represented in the lee of the mountains. θ shows

a positive bias aloft (A) for all three resolutions, and a negative bias in all lee-side consistent low-altitude θ-bias in the time-series in Figure 2.16, supports the argument that the low-level negative θ-bias is less sensitive to resolution and sourced in the driving model.

This observation is challenged by an increased bias at 4.4-km in the bottom 500 m of the ABL at 15Z, as seen in Figure 2.8, but this bias starts to recover towards 1.5-km levels by 18Z. In terms of RMS values this lack of resolution-dependency is also clear in all groupings, including A, with 4.4-km only measuring biases up to 0.6 K in the immediate lee and of approximately 0.1 K in the other groupings. The spike in low resolution θ-biases in the direct lee could be attributed to a lack of resolved and parametrised turbulent flux in the immediate lee, leading to a less mixed atmosphere close to the ridge.

Resolution sensitivity for q is erratic. 0.5-km and 1.5-km record lower mean and RMS biases than 4.4-km, with little difference between the two higher resolutions. Generally the model under-predicts q aloft and over-predicts in the lee. In the direct lee (B) and in the minimum-safe altitude leg (D) q mean biases for 0.5-km and 1.5-km are nearly negligible compared to the 4.4-km results, while q RMS biases are of similar magnitude across all resolutions. This could be due to resolved wave patterns being out of phase with observations, while moisture transport may be better resolved at higher resolution, affecting the mean values.

Overall mean and RMS atmospheric state variables show improved representation in the 0.5-km simulation compared to the 1.5-km and 4.4-km simulations. Model performance varies greatly with geographical location with aloft (A) and the immediate lee (B) showing the greatest mean and RMS biases across all groupings and most of the largest differences between resolutions, particularly showing 4.4-km giving the highest biases. The immediate lee of a mountain range is difficult to model accurately, and higher resolutions resolve flow structures in the 1-10 km scale, possibly leading to improved performance.

We recall the overall good correspondence between model fields and aircraft observations in Section 2.4.2, particularly exemplified by the agreement in vertical wind speed and the evidence for flow re-attachment and detachment from the surface in Figure 2.11 seen in both the observation points and the model cross-section. Viewed together with the 0.5-km simulation's superior performance compared to the

other regional resolutions discussed in this section we determine that the 0.5-km regional atmosphere forecast models the atmosphere and the strong wind event seen in Case 2 with reasonable fidelity and can be used as a suitable control simulation in our case study in Chapter 3.

2.5 CONCLUSIONS

In this chapter we have evaluated regional, and in part global model, performance in concert with observations from a variety of ground-based and airborne sources. We found that the model had a negative temperature bias in the lower ABL, below 500 m altitudes, accompanied by similar biases in specific and relative humidity. This bias was consistent across regional model resolutions and was found to be sourced in the global driving model. Its impact on orographic flow structures was considered to be minor, due to model and observed profiles following a similar gradient with a consistent bias between them below 1.5 km altitude, and considering that low-level lee-side aircraft observations and corresponding model points of atmospheric state variables showed tolerable agreement compared to measurements aloft and turbulent flux measurements, with wind speed showing large temporal and spatial variation, but generally agreeing with the amplitude ranges found in the flow.

The presence of the temperature bias in both case studies is likely coincidental due to the different synoptic air masses, as evidenced by other differences in air mass properties between both cases, and due to two case studies representing a small sample of model runs, and with no sensitivity tests performed or analysed to this point. Model RH values were positively biased, with forecast surface values approaching saturation. A consequence of that may be that undue precipitation, cloud formation, or fog could be predicted, with impacts on latent heat flux in the boundary layer.

Upstream and downstream profiles revealed greater contrast between the upper ABL and strong stable layer between the UM and observations. Observed profiles consistently show a strong vertical temperature gradient at above 2 km altitude, while the model predicts these to be weaker, lower, and in the case of a profile directly downwind of the Westfjords' eastern coastal ridge, nearly absent. Hydraulic jumps, as seen in the model are capable of disrupting a strong vertical temperature

gradient in such a manner (Sheridan & Vosper (2006)). Momentum and heat flux diagnostics appear to be underestimated, and are not represented aloft. This can be explained by considering that the flux diagnostics are a product of the boundary layer parametrisation, which account only for unresolved, sub-grid scale perturbations. This can then be taken in two parts, firstly the model under-represents unresolved fluxes, and secondly, more transport is resolved at increasing resolution.

Model resolution sensitivity varies depending on geographical location with respect to the coastal mountain range, altitude, and atmospheric variable. While the 4.4-km regional model represented the variables the least accurately in most cases, the differences between the 0.5-km and 1.5-km regional models were less obvious. Points aloft of the ridge and in the immediate lee showed the most significant sensitivity to resolution, while θ and q biases further downwind are similar to each other and further support the argument of a low-level bias in the ABL being sourced from the driving model.

Finally, the representation of a hydraulic jump evidenced by aircraft observations, suitable upstream conditions ($Fr \approx 1$) and low RMS biases compared to the 4.4-km forecast make the 0.5-km forecast a suitable truth simulation to study the downslope windstorm seen in Case 2 in greater detail in the remainder of this thesis.

3

INVESTIGATING SCALAR TURBULENT FLUXES DURING A STRONG WIND EVENT OVER A MESOSCALE MOUNTAIN RIDGE IN THE WESTFJORDS, ICELAND

3.1 INTRODUCTION

The representation of the influence of orography-induced gravity waves have on boundary layer processes, such as turbulent mixing, in numerical weather prediction (NWP) and climate models is a challenging field of study, with one approach to address the problems involved being high resolution simulations (Vosper *et al.*, 2018). Several recent studies have used grid-spacings in the low single kilometers with promising effectiveness; for example Elvidge *et al.* (2015) uses grid-spacing in their simulation of gap flows and their interaction with an ice shelf in Antarctica, Sheridan & Vosper (2005) has applied 200-m grid-spacing idealised simulations to the non-idealised Falklands's orography to study an upward vorticity transport during hydraulic jump and rotor flows, Gohm *et al.* (2008) used regional nests with the finest grid-spacing at 267-m to assess the onset phase of an Adriatic Bora, also featuring a hydraulic jump, and Lawson & Horel (2015) applied 1.3km grid-spacing in a Weather

Research and Forecasting (WRF) simulation of a case study of a Wasatch downslope windstorm.

A cross-disciplinary example is from Aslam *et al.* (2018) who identified that an oceanic bathymetry of 1.5km grid-spacing is necessary to sufficiently resolve an internal tide field, though they made it clear that this requirement may be situational to the region. This regional dependence also applies to downslope windstorms and their attributed structures, especially when their component's scale is related to the scale of the orography; for instance, an accurate representation of a downslope windstorm or hydraulic gap flow in a mountain range with gap and barrier widths of less than 20km would need a considerably finer grid-spacing than the global distribution of synoptic scale downslope winds studied by Abatzoglou *et al.* (2020).

In the case of Iceland, where our case study is situated, similar windstorms have been studied: a downslope windstorm downstream of the Snæsfellsness Peninsula (Ágústsson *et al.*, 2007), a mountain range very similar to the one studied in here in the Westfjords, and the larger Freysnes windstorm (Ólafsson & Ágústsson, 2007). Both of these studies deemed a NWP grid-spacing of 1-km necessary for their purposes. Applying the method of using a high resolution simulation verified against observations as a *truth* to develop parametrisations for lower resolutions, the research in this chapter focuses on a 0.5-km grid-spacing simulation, as it would resolve even finer structures in the wake of the downslope windstorm, which may play an important role in turbulent mixing and downstream scalar transport.

While the lee-side impacts of downslope windstorms near the slope are well studied, the impact of small-scale windstorms on the large-scale circulation remains an open question; we know that wave breaking dissipates momentum and a variety of foehn mechanisms draw down heat from higher levels (Elvidge & Renfrew, 2016), gravity waves transport momentum away from the troposphere and often lead to clear air turbulence (Elvidge *et al.* (2017)), while PV banners emanating from mountain ranges are linked to cyclogenesis in the larger scale (Aebischer & Schär, 1998). Smith (1987) and Jiang & Doyle (2004) found peak heat fluxes of 100 W m^{-2} associated with a hydraulic jump during a Bora and foehn flow, respectively. Less is known about the transport into the large-scale flow, particularly for scalar quantities that are often neglected in NWP parametrisation schemes (Vosper *et al.*, 2018).

3.1.1 CHAPTER OUTLOOK

This chapter presents the same NWP case study (Case 2) that was verified against observations in the previous chapter, in which a downslope windstorm with a hydraulic jump is portrayed in the UM regional nesting domains in the Icelandic North-Western Westfjords peninsula, but not in the global driving model, which has much more smoothed orography and a horizontal grid-spacing of about 17 km. The lee opens up to the Iceland Sea, and so offers a suitable test-bed for investigating the contribution of the modelled downslope windstorm on the large-scale flow, as it is unencumbered by surface heterogeneity.

In this study the following questions will be explored:

- What is the effect of resolution on model reproduction of the downslope windstorm?
- Does the windstorm have a measurable effect on the large-scale flow?
- How sensitive is the windstorm's lee-side impact to changes in sub-grid-scale processes?

3.2 METHODS

3.2.1 RESOLUTION SENSITIVITY

To directly compare outputs between domains with different resolution, the following steps are taken:

- The larger (and coarser domains) are subset using the latitude-, longitude coordinates of the vertices of the 0.5-km nested domain. These are given as grid-coordinates and are unrotated from the coordinate system of the model grid projection into Earth-coordinates to subset the global domain.
- The coarse domains are regridded with Python Iris regridding tools, using a linear interpolation scheme. Linear interpolation was chosen instead of nearest-neighbour interpolation to create more smoothly varying regridded fields. This does not generate false data, as the detail of the regridded field

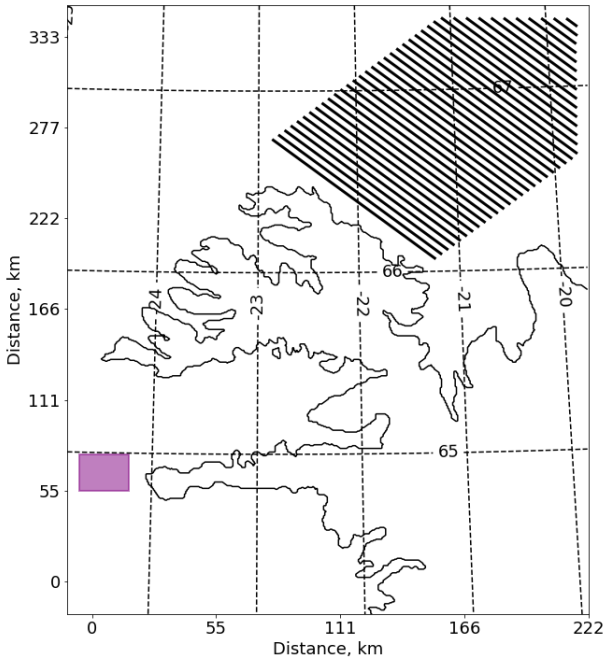

Figure 3.1: Illustration of leeside difference decay sampling. Solid lines represent sequence of 37 evenly spaced sample points and lines are spaced at 4km intervals. Sample-line size is tapered towards domain edge to exclude domain-border transition grid-points. The purple box denote the upstream sampling area for the $\hat{h}$ derivation. UM 0.5-km grid-spacing coastline (solid) and one degree latitude/longitude contours (dashed) are given for reference.

does not change, but instead creates continuous transitions between coarse grid-cells in the now high-resolution grid.

- The differences, or anomalies, between the different domains are calculated by subtracting the 0.5-km data from the regridded initially low-resolution data (i.e. 4.4-km and GLM), shown here for a quantity Γ:

$$\Delta\Gamma = \Gamma_{0.5-km} - \Gamma_{regrid} \tag{3.1}$$

To study the rate of decay of the lee-side anomaly as a result of the wind-event in this case study, mean anomalies of key fields are obtained along 37 sampling lines parallel to the ridge where the wind event, each spaced 4km apart (Figure 3.1). This number and spacing was chosen to sample sufficiently separated data as far as possible as the domain boundaries would permit. The lines are comprised

of evenly spaced points which are then used to sample the anomaly fields by the nearest-neighbour method, where the gird-point closest to the specified coordinate is selected. The sample points are spaced by 0.005° in both grid-longitude and grid-latitude, which is the horizontal grid-spacing of the 0.5-km nested domain. Since the sampling lines are approximately diagonal to the grid-axis, the sample points are spaced approximately 0.007° (or 700 m), which should ensure that each sample point corresponds to a different grid-point.

Adiabatic adjustment only applies to air temperature fields on Cartesian vertical coordinates (e.g. 1.5-m temperature). For air temperature on pressure surfaces the variability in the temperature field is invariant under transformation into potential temperature, which is conserved under adiabatic displacement.

Due to a technical issue the air temperature on pressure levels diagnostic was unavailable for the global driving model output and could not be accurately derived. It is therefore omitted from the results in this chapter.

3.2.2 LONGTAIL SENSITIVITY TEST

The stability function f_{stable} is a function of the *gradient* Richardson number Ri (a dimensionless quantity, the ratio of *buoyant consumption by static stability* and *mechanical generation by wind shear* (Wallace & Hobbs (2006))) and is used as a scaling parameter in the atmospheric boundary layer scheme in the first order mixing length closure under stable conditions (Lock *et al.* (2021)):

$$K_m = L_m^2 (S + S_d) f_m(Ri) \tag{3.2}$$

$$K_h = L_h L_m (S + S_d) f_h(Ri) \tag{3.3}$$

where K_m and K_h are the eddy-diffusivities calculated for momentum and scalar variables respectively and are related to the sub-grid flux, derived through the covariance method, of each variable in a first order closure. L_m and L_h are the neutral mixing lengths, S is the resolved horizontal wind shear, and S_d is a wind shear quantity related to parameters describing the Earth's surface at that grid-point. f_m and f_h become f_{stable} under stable conditions where $Ri > 0$. The stability function dampens the sub-grid turbulence to bring it in line what is observed in

real atmospheric processes (Elvidge *et al.* (2017); Lock *et al.* (2021)). The gradient Richardson Number Ri, used in the UM as *a local measure of stability* (Lock *et al.* (2021)) is given by

$$Ri = \frac{\Delta B/\Delta z}{S + S_d} \tag{3.4}$$

where ΔB is a measure of buoyancy and Δz is the change in height across which ΔB is derived. The default stability function in the UM RA1M configuration is the SHARPEST family of functions defined by a transitional Richardson number Ri_t, and an early form is first introduced by King *et al.* (2001), where it has been found to effectively model the sharp fall in turbulence under low positive Richardson numbers (Lock *et al.* (2021)):

$$f_{stable} = \begin{cases} (1-5Ri)^2 & \text{for } 0 < Ri < Ri_t \\ (A_{Ri} + B_{Ri}Ri)^{-2} & \text{for } Ri > Ri_t \end{cases} \tag{3.5}$$

where

$$A_{Ri} = \frac{1 - g_0 Ri_t}{(1 - g_0 Ri_t/2)^2} \tag{3.6}$$

$$B_{Ri} = \frac{g_0/2}{(-g_0 Ri_t/2)^2} \tag{3.7}$$

where g_0 is a constant usually set to 10 and Ri_t is set to 0.15. King *et al.* (2001) have also tested the Louis function (Louis (1979), which is now available in the UM boundary layer scheme (Lock *et al.* (2021)):

$$f_{stable} = \frac{1}{(1+5Ri)^2}. \tag{3.8}$$

The other available stability function is the long-tailed (longtail) function,

$$f_{stable} = \frac{1}{1+g_0 Ri}. \tag{3.9}$$

The longtail stability function used to be in the UM's operational settings, but was replaced in part because it produced higher sub-grid scale turbulent mixing for high atmospheric stability than large eddy simulations and observations would resolve (Brown *et al.* (2008); Beare *et al.* (2006)). The response of the different stability

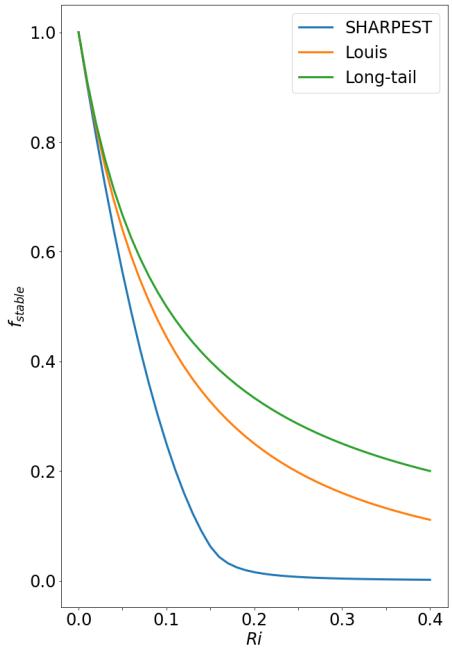

Figure 3.2: Atmospheric boundary layer stability function, f_{stable} variability with Richardson number Ri. For the Louis and longtail functions, g_0 is set to 10, and the SHARPEST function is computed with $Ri_t = 0.15$.

functions to changes in Ri are shown in Figure 3.2; The longtail and Louis stability functions provide greater mixing at higher stability (i.e. higher Ri) relative to the SHARPEST function.

Recently, Elvidge *et al.* (2017) used (3.9) in their computation of a new TKE diagnostic for the prediction of mountain wave induced clear air turbulence aloft with reasonable success. For its application in modelling mountain wave processes and due to the significant divergence from the SHARPEST function, we chose the longtail function for a sensitivity test that aims to help constrain the uncertainty in the inter-resolution analysis, while the operational RA1M configuration is used as the control.

Since both model and observed profiles during the case study date show a stable atmosphere, changing f_{stable} in the boundary layer scheme is expected to produce a noticeable response throughout the forecast. The operational global UM stability function is set to SHARP-sea/Mes-land, which applies SHARPEST to sea points, while above land it uses the Mesoscale model, which linearly blends the Louis function from the surface to SHARPEST by 200 m altitude (Brown *et al.* (2008)). The global driving model settings are kept the same for both the control and the longtail test.

The longtail regional output is compared to the GLM using the same method described in Section 3.2.1, while the 0.5-km longtail and control outputs are

compared using

$$\Delta\Gamma = \Gamma_{control} - \Gamma_{longtail}. \tag{3.10}$$

3.2.3 MISCELLANEOUS

CROSS-BARRIER VELOCITY

The cross-barrier velocity, v_{cb} is the component of the wind speed normal to the major axis of the ridge measured at or just above the mountain crest and plays an important role in the formation of downslope windstorms (Jackson *et al.* (2013); Abatzoglou *et al.* (2020)). We measured it by first defining a sample region representative of the ridge crest and then conditionally sampled all grid-points for which the corresponding surface altitude is above 500 m. This condition avoided the stagnant overturning region from polluting the sample and therefore provided a more accurate calculation of v_{cb}. The wind components u and v are obtained from the sample region to calculate the wind-speed U and the wind direction, which are then used to obtain the component of the wind perpendicular to the ridge major axis, which is approximately 45° to the y-axis of the model grid. Finally, the mean of all the computed grid-point v_{cb} values is taken to get a representative value for the ridge at each time point.

CALCULATING HORIZONTAL WIND SPEED

When horizontal wind speed is averaged across time, for example for a composite, it is calculated in a particular order across all chapters in this thesis. For horizontal wind velocity components u (northward) and v (eastward) at time t we apply quadrature to obtain

$$U(t) = \sqrt{u(t)^2 + v(t)^2} \tag{3.11}$$

where $U(t)$ is the scalar wind speed at a particular grid-point or flight run at time t. U is sometimes notated as wsp, and is sometimes also spatially averaged, depending on application - this will be clarified when done so. To obtain the time-averaged composite, $U(t)$ is then simply averaged across all defined time-steps.

NON-DIMENSIONAL MOUNTAIN HEIGHT

The non-dimensional mountain height, $\hat{h}$, is the inverse of the Froude Number, and is a non-dimensional quantity used to predict the interaction of atmospheric flow with orography, given by

$$\hat{h} = \frac{Nh}{U} \tag{3.12}$$

where h is the mountain barrier height, N is the Brunt-Väisälä frequency measured upstream from the barrier, and U is the upstream horizontal wind speed measured at crest level (e.g. Elvidge *et al.* (2015); Durran & Menchaca (2017)). For windstorms when the value of $\hat{h}$ falls within a certain range, around $\hat{h} = 1$, then the lower layer of the atmosphere flows over the mountain and produces gravity waves, and wave breaking can occur. Large values of $\hat{h}$ ($\gg 1$) lead to flow blocking, while small, or sub-critical, values of $\hat{h}$ ($\ll 1$), allow for a smooth flow of air over the barrier, reducing the amplitude of the generated gravity wave (Jackson *et al.* (2013)). It is worth noting that flow-blocking would only occur for a ridge that is sufficiently wide to act as a 2-D barrier, where as for 3-D mountains (e.g. conical shaped mountains), the flow would split around it.

Figure 3.1 illustrates the location of the sampling area for the $\hat{h}$ calculations in this chapter. The sampling area is placed to be upstream of the Westfjords, as far from the peninsula as the domain boundaries allow, which is at a distance of about 50-70km from the nearest part of the Westfjords' coast, the lower end of Rossby radii of deformation that we calculated for this mountain range, but is sufficiently far away from the northeastern coastal ridge, of which the focus of this case study lies. The flow in this sampling area would still be partly influenced by the Westfjords as well as by the Snæsfellsness peninsula to the East, introducing uncertainties that need to be considered.

The area contains 1600 grid-points which are used to compute U on a single level at 850-hPa, which during the case study fell between 1400 m and 1500 m altitude, and N for the layer between the aforementioned 850-hPa level (1400-1500 m) and the 925-hPa level (700-800 m). U can be taken from the level closest to the mountain crest, while N requires a measurement of the temperature gradient across the top of the mountain. Two different values of h were considered; 750 m represented the typical

mountain height of the peninsula in the 0.5-km domain orography, and 1000 m was representative of the crest below which the windstorm took place. Section 3.3 will use the calculations for $h = 1000$ m, since it is more relevant to the case study windstorm.

3.3 WINDSTORM EVOLUTION

In Chapter 2 we evaluated a UM regional atmosphere forecast for the 19th March 2018 over western Iceland against aircraft, radiosonde, and ground-based observations. Given the good correspondence between aircraft observations and model output (for example in the vertical cross-sections in Figures 2.12 and 2.12) and the relatively low biases of the 0.5-km simulation compared to the 1.5-km and 4.4-km simulations (Figure 2.21 and 2.22), we were able to conclude that the 0.5-km regional atmosphere simulation reproduces a downslope windstorm with reasonable fidelity, and so can be used by us as a truth simulation in this case study.

In Chapter 2 we saw a downslope windstorm with a hydraulic jump during the period of the aircraft observations (12Z-16Z), so before we directly address the questions given in Section 3.1 we will expand our view to the whole forecast and characterise the evolution of our case study windstorm. This will provide us with some initial information about the windstorm's sensitivity to the upwind conditions (which will be indicated by $\hat{h}$). It will also allow us to determine what forecast times provide the most suitable state of the windstorm for a more detailed investigation of the event's impacts downstream and potentially on the large-scale circulation.

VARIABILITY OF WINDSTORM STRUCTURE ACROSS TIME

At least three distinct phases are identified, in which the storm shows different coherent structures and intensities in both the vertical and horizontal dimensions. Points in time from different perspectives (using representative cross-sections of these phases) are shown in Figures 3.3 and 3.4. At the start of the simulation (19th March 2018 00:30 UTC, or 00:30Z forecast time) downslope acceleration is already present, but 10-m wind speeds do not pass 20 m s^{-1} until 8Z (not shown). Over time the downslope windstorm grows in size and intensity, with a hydraulic jump forming early, but frequently changing shape and location. Between 8Z and 10:30Z the storm's surface jet increasingly protrudes out to sea until it reaches an extent of 15-20 km that

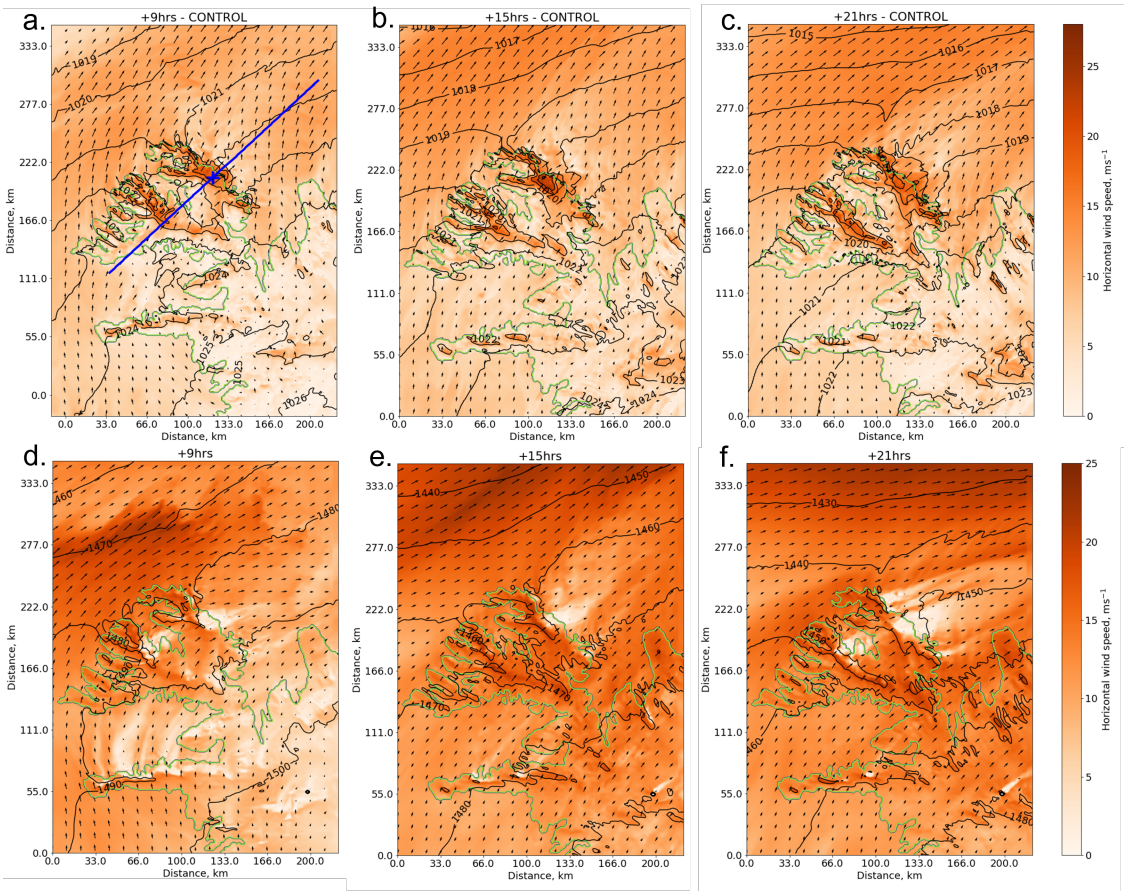

Figure 3.3: UM 0.5-km RA1M maps of horizontal wind-speed (colour scale) on case study date (19th March 2018) at 10-m (a-c) with mean-sea-level pressure 1 hPa contours (solid black) and 850-hPa (d-f) with geopotential height 10 m contours for 9Z (a,d), 15Z (b,e), and 21Z (c,f) forecast time. Blue line in a) represents location of and approximate extent of all subsequent vertical cross-sections in this chapter. Model coast-line in green. Axes are horizontal distance in kilometers. The blue cross in panel a) marks the centre point (0 km) for Figure 3.4.

is maintained hours after 15Z (Figures 3.3 and 3.4).

At 15Z a smaller secondary jump briefly forms on-shore and isentropes reach peak verticality. The formation of a stable layer at crest height and a secondary hydraulic jump, steep isentropes and a peak in wind speeds (Figures 3.3, 3.4 and 3.6) suggest that the simulated downslope windstorm is at its strongest at 15Z, compared to 9Z or 21Z where some of the above features are absent, or wind speed is not as strong than at 15Z. This makes the 15Z forecast time a suitable time for our more detailed investigation in Section 3.4 and 3.5, where we address the question of what the downstream impact of the windstorm representation in the 0.5-km simulation is relative to the coarser simulations. The shallow stable layer forms in the potential temperature contours at 2 km altitude, where we have established the top of the ABL

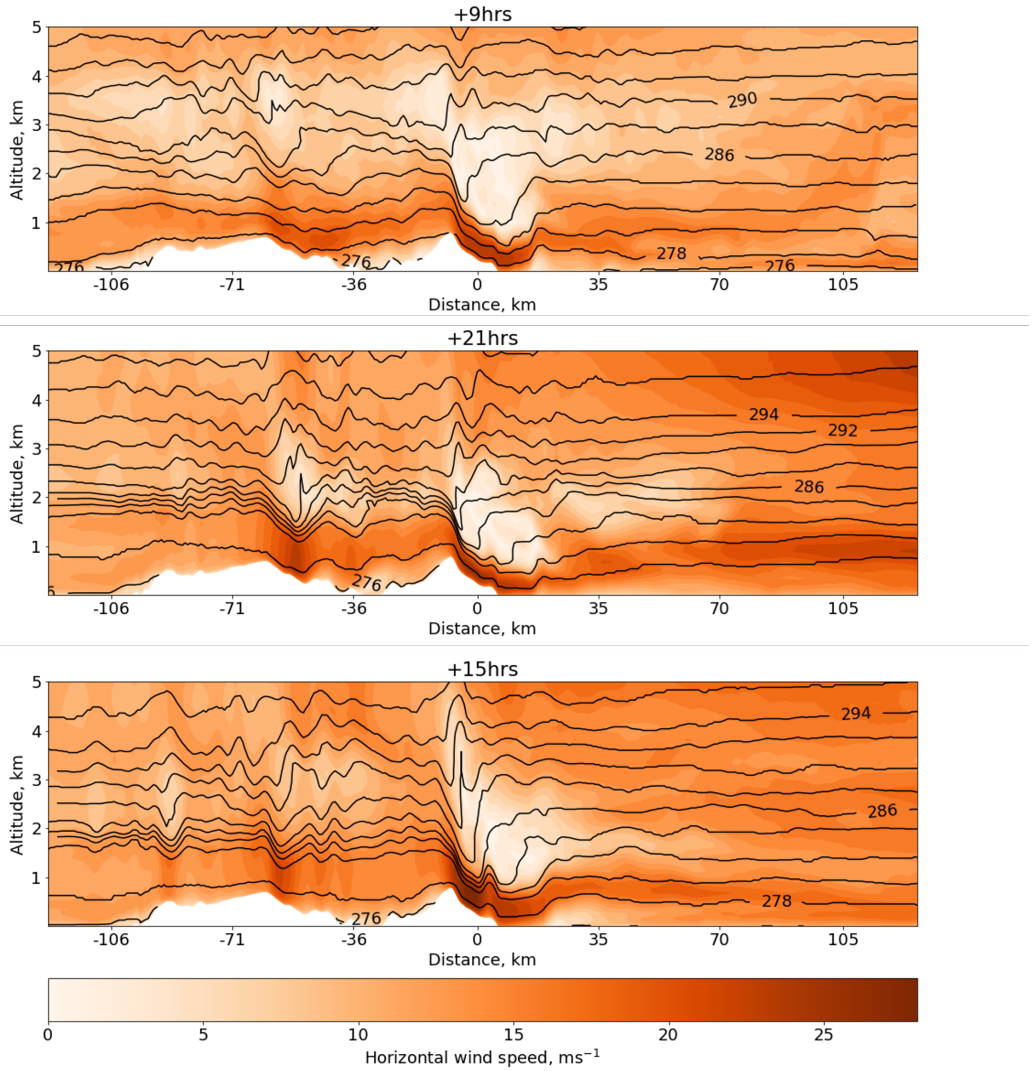

Figure 3.4: UM 0.5-km RA1M along-wind slices of horizontal wind-speed (colour scale) and 2 K potential temperature, θ, contours (solid black) on the case study date (19th March 2018). Orography is masked (white). Vertical axis is altitude in kilometers and horizontal axis is distance in kilometers centered on slope of interest. The 0-km centre point is marked as a blue cross in Figure 3.3.

to be in Chapter 2, but this layer is not strong enough to be considered an inversion in the way Vosper (2004) describes them, with $\delta\theta/\delta z \ll 0.1$ K m^{-1}.

This inversion-like layer is discussed in detail in Chapter 2 Section 2.4 and we recall that the modelled vertical temperature gradient at this height was significantly smoother than the sharp discontinuity that was observed in the upstream radiosondes and aircraft observations downstream; this difference leads us to expect a weaker gravity wave response from the model (e.g. Vosper (2004)). This stable layer is dispersed in the overturning region and does not recover in the lee within the

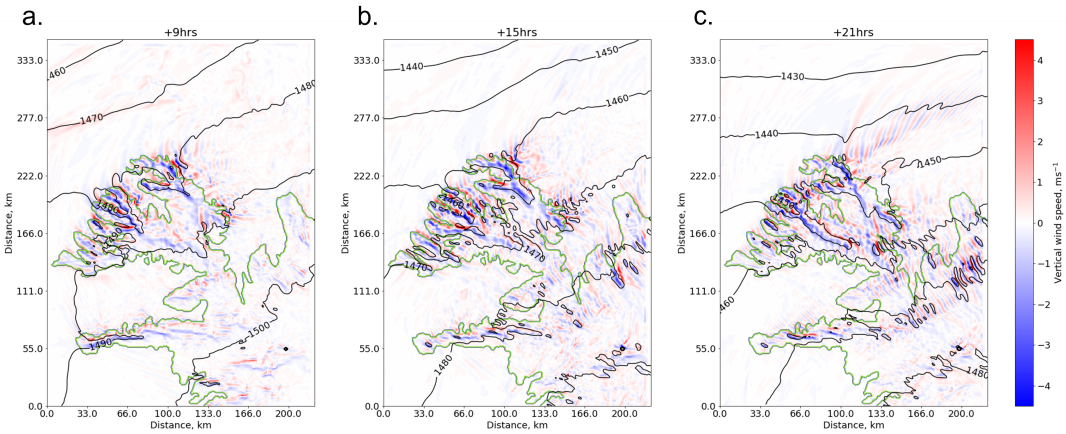

Figure 3.5: UM 0.5-km RA1M horizontal slices of vertical wind-speed (colour scale) on the case study date (19th March 2018) at 850hPa with geopotential height 10 m step contours for 9Z (a), 15Z (b), and 21Z (c) forecast time. Model coast-line in green. Axes are horizontal distance in kilometers.

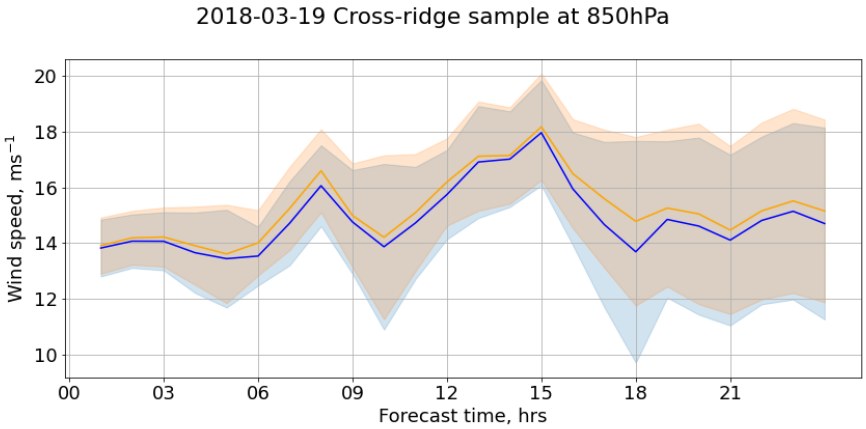

Figure 3.6: Time-series of U (orange) and v_{cb} (blue) sampled above ridge at 850hPa on case study date in the UM 0.5-km grid-spacing RA1M/control run, with one standard deviation over the sample area (shaded). Horizontal axis is forecast time in hours, and output is hourly.

bounds of the domain (Figure 3.4), even though the downstream profile from aircraft observations in Chapter 2 still shows an inversion-like discontinuity in the potential temperature gradient.

So while this disruption of the atmospheric stratification could persist until the flow rejoins the large-scale circulation, it could be a uniquely modelled effect; a weaker than observed stable layer aloft may be more susceptible to disruption than a strong inversion, for example. In the evening the hydraulic jump moves out to sea and gradually weakens until it largely loses coherence (Figure 3.4). After 20Z downslope winds retain speed, but the jet becomes more shallow, and overturning isentropes

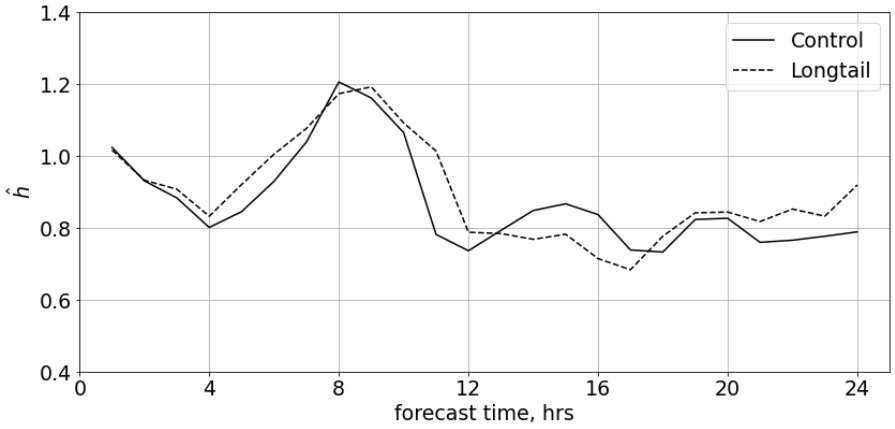

Figure 3.7: Time-series of non-dimensional mountain height, $\hat{h}$, for control (solid) and longtail (dashed) runs on case study date (19th March 2018) measured by the method described in Section 3.2.3.

become concentrated and move closer to mountain peak, though overturning still appears strong. The stagnant wave breaking region persists and extends closer to sea surface.

By 0Z on 20th March 2018 (+24 hrs integration time) the windstorm still persists, though weaker than in the afternoon, and short wavelength standing waves form in the near-surface jet and the hydraulic jump starts to recover out at sea (not shown). At 9Z and 21Z, and at 15Z only at the fringes of the storm, wave patterns are visible in the mean-sea-level pressure contours, which are in step with vertical velocity perturbations at 850-hPa, as shown in Figure 3.5. After 12Z two standing wave patterns come off mountain peaks at each end of the coastal ridge (Figure 3.3 and 3.5), with wave activity being suppressed in the centre, where the wave breaking occurs.

A wake visible in both 10-m and 850-hPa wind speed fields gradually curves eastward throughout day, and the deceleration from the wave breaking gradually lengthens into the bay area, clearly reaching the edge of the 0.5-km regional domain by 21Z (Figure 3.3 c and f). This long wake is bordered by a long banner of standing waves to the north at 21Z (Figure 3.5). Wave activity in the boundary layer is associated with wave-induced turbulent mixing (Hertenstein & Kuettner (2005); Doyle & Durran (2007)), so if a visible wave pattern extends for over 100 km downstream, we may see downstream changes to the atmospheric state field and influences in the large-scale flow because of it.

VARIABILITY OF v_{cb} AND $\hat{h}$

Figure 3.6 shows time series of cross-barrier velocity v_{cb}. The first half of the forecast shows a more variable v_{cb} and U over time, but a more homogeneous field over the crest than the second half of the forecast. Apart from a peak mean cross-barrier wind of 18 m s^{-1} at 15Z, speeds remain consistent within 12-18 m s^{-1} during the forecast. U and v_{cb} remain very similar, and almost entirely intersect, suggesting that the local atmospheric flow was consistently incident perpendicular to the mountain ridge, which is a favourable condition for downslope windstorm generation (Jackson *et al.* (2013)).

Figure 3.7 shows the non-dimensional mountain height $\hat{h}$. Referring back to Figure 3.6, the highest cross-barrier winds as evident in the upper first standard deviation correspond to a forecast period with the most consistent $\hat{h}$ of 0.8-0.9, while the first half of the forecast is defined by high temporal variability in the non-dimensional mountain height, during which $\hat{h}$ reaches 1.2, and relatively low cross-barrier wind speed as seen in the first standard deviation. The windstorm appears strongest during times when $\hat{h}$ is consistently close to 0.8, which suggests that this value is more favourable for a windstorm to form on this slope than for higher values calculated with h = 1000 m, despite the value range during the forecast being reasonably close to 1. This may suggest that flow blocking plays an important role in the Westfjords.

SUMMARISING CASE STUDY WINDSTORM EVOLUTION

The three phases can be described as follows:

- 9Z: The initial phase of the windstorm from 8Z to 10Z has relatively moderate cross-barrier winds with speeds between 11 m s^{-1} and 17 m s^{-1} within one standard deviation. A hydraulic jump has freshly formed and ambient flow conditions lead to multiple sizeable wakes across Western Iceland. The atmosphere is roughly equally stratified up- and downwind, and low-level lee-waves have formed across the ridge, though upwind conditions appear variable as shown in $\hat{h}$.

- 15Z: The second phase is characterised by a complete disruption of a newly formed stable layer through the windstorm, the largest seen jump in the

isentropes leading to strong overturning, a well-developed hydraulic jump near its peak, and a 850-hPa flow field locally dominated by the windstorm. Other low-level lee-waves appear to have dissipated. v_{cb} peaks at this time and upwind flow conditions appear to start to settle. A strong resolved vertically propagating gravity wave is also apparent.

- 21Z: The phase spanning 17Z to 21Z represents a period where cross-barrier winds are spatially most variable and moderate, and where the surface jet and hydraulic jump are more shallow than during the rest of the forecast. Lee-waves begin to reappear in the ABL. These lee waves extend for over 100 km downstream. Like the second phase a tight stable layer is completely disrupted by the windstorm, but not by a secondary windstorm that has formed upwind. Isentropes still show overturning, but less strongly, and the wavebreaking region has reduced in its vertical extent and moved closer to the surface. The vertically propagating gravity wave is also suppressed or dissipated at low level.

These three phases appear to represent distinct windstorm behaviours, although they all appear to generate a hydraulic wave to some degree. To answer the questions set out in the chapter introduction in more detail, the model output at 15Z will be examined, as it represents the windstorm at a mature stage, where the windstorm is at its most intense with the steepest isentropes and highest wind speeds.

3.4 RESOLUTION SENSITIVITY

At this point we recall the first two questions laid out in Section 3.1:what is the effect of resolution on model reproduction of the event, and does the event have a measurable effect on the large-scale flow? In the previous section we have identified three distinct phases of the downslope windstorm event's development throughout the forecast, of which the phase represented by the forecast time 15Z was the strongest. 21Z was also investigated during this study, due to its long lee wave signal, however, the inter-resolution and longtail differences at 21Z are very similar to 15Z and do not show any significant distinctions to warrant showing all of our atmospheric state and difference fields for both forecasts times. Therefore 21Z will not be discussed in detail in the following sections.

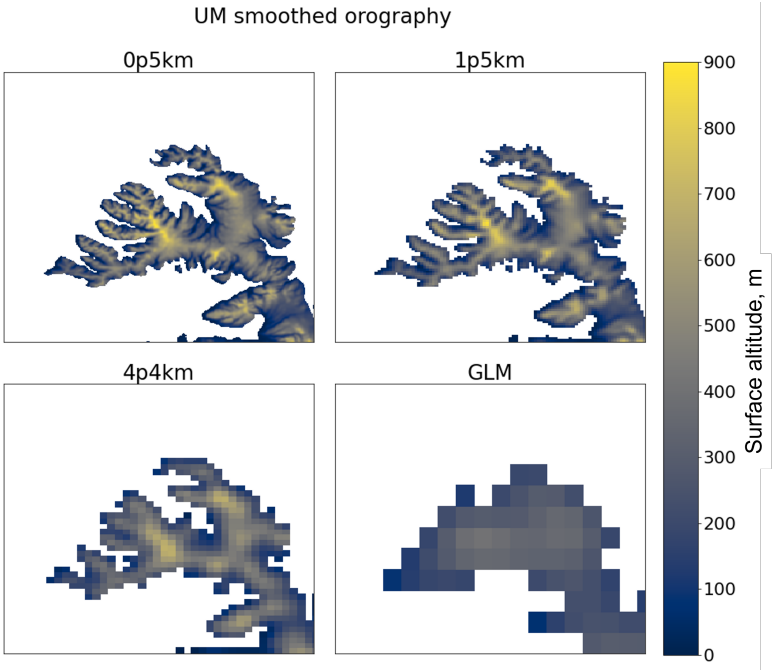

Figure 3.8: Maps of the smoothed orography over Westfjords for the 0.5-km (top left), 1.5-km (top right), 4.4-km (bottom left) and GLM (bottom right) UM configurations. The color scale represents surface altitude above sea-level.

3.4.1 COMPARISON OF OROGRAPHY FIELDS

Figure 3.8 illustrates the differences in orography between the different resolutions. As expected, 0.5-km grid-spacings return the greatest level of detail with fully expressed gaps, valleys, and promontories, and peaks reaching 900 m above sea level and higher in the peninsula, and 1.5-km looks reasonably similar. The 4.4-km grid-spacing does not show the gaps and valleys between the peaks seen at finer resolutions, and peak heights reach only about 600-700 m. The global driving model loses most detail, with all the fjords being lost likely due to the grid-spacings being so large that the grid-points had more land than water, classifying them all as land-points. Instead of a complex mountain range the peninsula resembles a smooth hill of 300-400 m height. The differences in representation will have a fundamental influence on the modelled flow over and around the Westfjords.

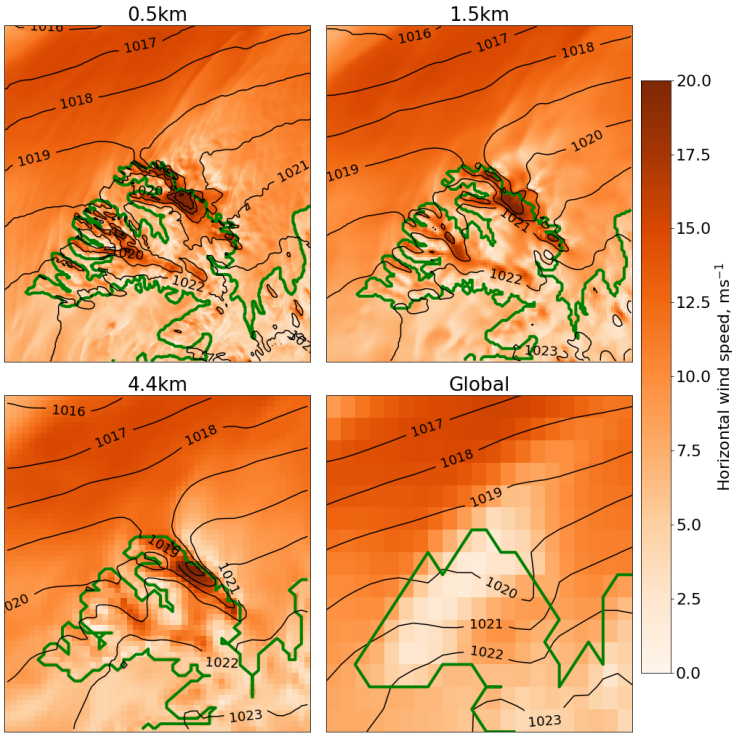

Figure 3.9: UM control horizontal slices of 10-m horizontal wind-speed for regional and global runs (as labelled) at 15Z forecast time subset over Westfjords. Contours are mean sea-level pressure (black) in hPa and model coastline (green).

3.4.2 COMPARISON OF WAKE IN WIND SPEED FIELDS

When comparing the wind speed fields over the region between the different domains we note significant differences in the representation of the wind event occurring on the northeastern coastal slope of the peninsula, as shown in Figures 3.9 and 3.10. The 0.5-km grid-spacing resolves complex lee-side wave patterns at the surface in both the wind field and mean-sea-level pressure contours, which correspond to similar patterns in the vertical velocity field at 850-hPa (Figure 3.5), and a jet protruding from the slope into sea corresponding to the hydraulic wave seen in Figure 3.4. The 4.4-km domain only shows the downslope acceleration, but no finer features. The 1.5-km grid-spacing still resolves the protruding jet, but loses the fine structure wave patterns.

While the regional domains all showed similar peak downslope wind speeds (20 m s^{-1} for 0.5-km, and about 18-19 m s^{-1} for 1.5-km and 4.4-km), the global domain does not show a downslope windstorm signature. Instead it shows an area of strong

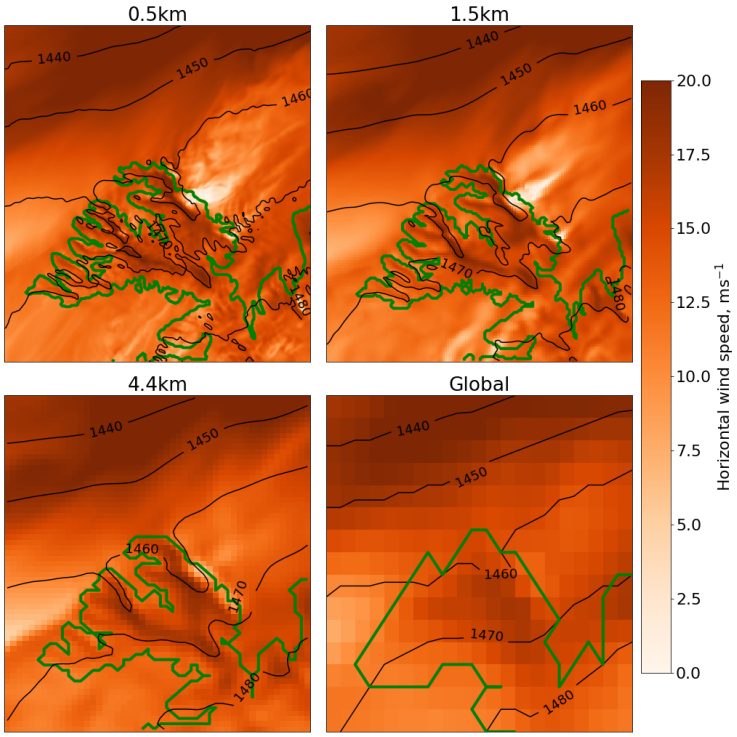

Figure 3.10: UM control horizontal slices of 850-hPa level horizontal wind-speed for regional and global runs (as labelled) at 15Z forecast time subset over Westfjords. Contours are geopotential height (black) in meters and model coastline (green).

deceleration with wind speed values approaching zero, possibly due to some form parametrised drag or flow blocking. One potential contributor to this effect is the gravity wave drag scheme, which is influential at typical GLM resolutions, but has been switched off for the 1.5-km and 0.5-km nests. The peninsula in all domains will be exerting drag on the atmosphere, regardless of the resolved localised downslope accelerations. This is to be considered when discussing the importance of small-scale unresolved phenomena, such as downslope windstorms, as they have independent effects on the flow, but could also be considered as part of the whole function.

At 850-hPa we see a similar difference between the different configurations, as seen in Figure 3.10, where the highest resolution domains show a well-expressed lee-side region of decelerated flow which coincides with the overturning region seen in Figure 3.4; this lee-side wave-breaking region flows over into a distinctive wake. The 4.4-km grid-spacing shows a diminished deceleration area, and it is difficult to attribute it to overturning, even though vertical cross-sections show that this still occurs (not shown). All regional configurations show similar wind speeds at or near

the peaks, with 0.5-km exceeding 18 m s^{-1} and 4.4-km and the GLM reaching wind speeds of about 16 m s^{-1} at the ridge, which is 2 m s^{-1} slower than the highest resolution (0.5-km). High cross-barrier wind speed, v_{cb}, is used as an indicator of downslope windstorm activity (e.g. Durran (1986); Reinecke & Durran (2009); Abatzoglou *et al.* (2020)), so we could reason that the cross-barrier wind speeds in the 4.4-km simulation (Figure 3.10) would produce a weaker downslope windstorm than 0.5-km.

Recalling the 10-m downslope winds in Figure 3.9, which are about 18-19 m s^{-1} for 4.4-km and over 20 m s^{-1} for 0.5-km, we find that the difference in-between the two regional simulation's downslope wind speeds is similar to the difference in their cross-barrier wind speeds in Figure 3.10. The effect of a lower cross-barrier wind speed may be proportional to the downslope wind speed, but we do not have enough simulations to prove that. What we do know is that both 0.5-km and 4.4-km show strong downslope wind speeds. Abatzoglou *et al.* (2020) found that for WRF simulations over meso-scale mountain ranges (like our own) a v_{cb}-threshold as low as 14 m s^{-1} was enough to detect downslope windstorm activity. Based on that all four domains show wind speeds suitable for the formation of a downslope windstorm.

A key difference between 4.4-km and the GLM, which show similar cross-barrier winds (around 16 m s^{-1}), is in the slope of the orography, since the GLM orography is significantly more smoothed than the 4.4-km orography (Figure 3.8). There are a number of resolution sensitivity studies that determined a link between underestimated slope steepness and underestimated 10-m wind speed (e.g Oltmanns *et al.* (2015); Moore & Imrit (2022)). For example, Oltmanns *et al.* (2015), who simulated two downslope wind events in south-east Greenland using the WRF model and found that a 60 km grid-spacing simulation underestimated local 10-m wind speeds by 20 m s^{-1} compared to a 5 km grid-spacing simulation. They attributed this underestimation in wind speed to the differences in topographical gradients (steepness of the slopes) between the different resolutions. Specifically, they argue that both a high-resolution model, to simulate the wave dynamics, and a high-resolution topography, to provide the steepness needed for strong wave responses, are needed to simulate downslope wind events with fidelity and we find that this argument applies to our own case study, too.

So far we can surmise the 0.5-km resolution is required to resolve many of the

distinctive features in this downslope windstorm. In Chapter 2 we saw that some key features, such as the flow reattachment in the lee expressed by the surface-level jet seen in Figure 3.9, are reasonably well captured by the 0.5-km resolution when compared to aircraft observations. The 0.5-km model also showed the lowest RMS biases compared to aircraft observations above the ridge and in the immediate lee (Figure 2.22). We consider what the differences are in the wake between the domains in which the windstorm is well resolved and the domains where it is poorly resolved or not at all modelled. We also ask the question if the presence of a well resolved downslope windstorm has measurable downstream impacts on the large-scale flow.

The global model field at 850-hPa surrounding the peninsula still depicts a wake (Figure 3.9 and 3.10), which we attribute to the orography as a whole. It is logical that the peninsula as a whole would also be creating its own wake in the higher resolutions, and that the resolved windstorm acts as a contributor to the wake. This question is asked in Section 3.1 and will be addressed in the following section, where we will look at the differences in the lee between the 0.5-km truth and the coarse GLM and 4.4-km simulations.

3.4.3 DIFFERENCES IN ATMOSPHERIC STATE FIELDS

We have determined that a downslope windstorm is reasonably well represented in the 0.5-km simulation, but has some features missing in the 4.4-km model and is not represented in the GLM. We discussed that the main contributors to this difference between resolutions are the wave resolving dynamics of different resolutions and the underestimation of slope steepness in the smoothed orography in the 4.4-km and GLM models, and this argument is supported by the findings of other resolution sensitivity studies (e.g. Oltmanns *et al.* (2015); Moore & Imrit (2022)). We recall the questions from Section 3.1, which were restated at the end of the previous section. The first question has already been partly addressed my comparing the model wind speed fields in the previous parts of this section. Now we will expand our analysis to other diagnostics and quantities to get a more complete picture of the effect of resolution on the representation of the event, and to assess the downstream impacts of the resolution sensitivity in the model representation of downslope windstorms.

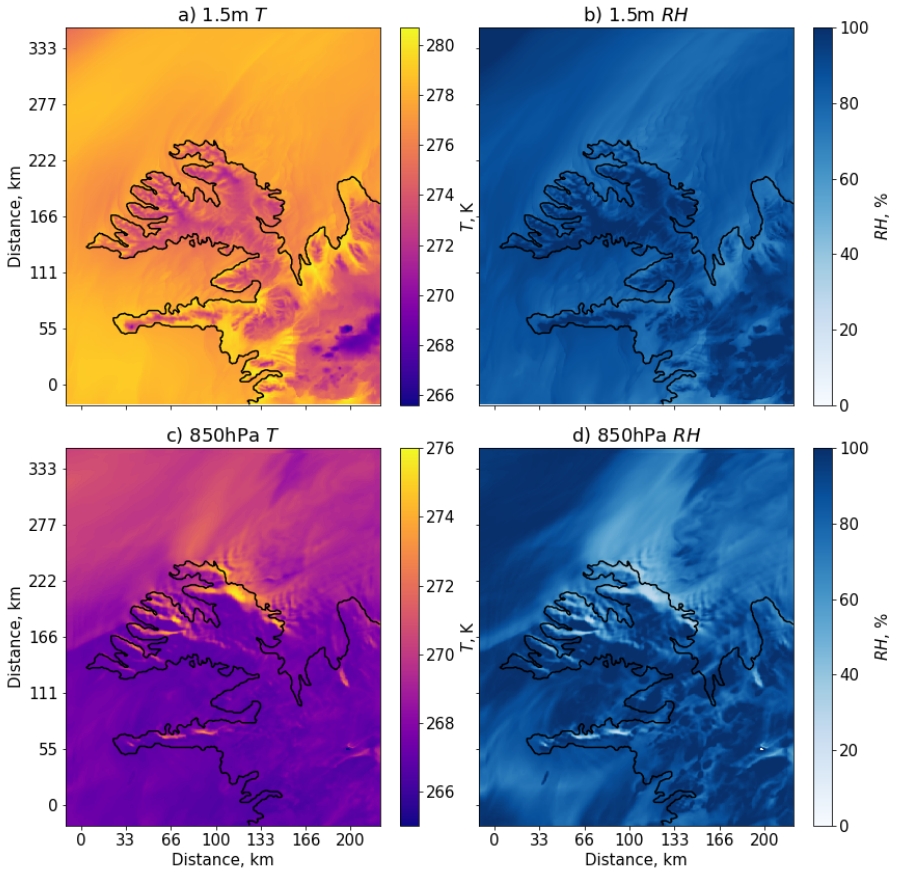

Figure 3.11: UM 0.5-km RA1M maps air temperature T at 1.5-m (a) and 850-hPa (c) and relative humidity RH at 1.5-m (b) and 850-hPa (d) at forecast time 15Z on case study date (19th March 2018). Horizontal axes are distance in kilometers. Note change in temperature colour scale.

Figure 3.11 shows the 1.5-m and 850-hPa air temperature T and relative humidity RH fields for the 0.5-km simulation at peak windstorm strength. The main point conveyed by Figure 3.11 is that there are strong lee-side warming and drying effects visible in the 0.5-km resolution; At 1.5-m there is a small build-up of cool (276 K compared to 278 K and higher further upstream) and moist (over 80 %) directly upstream of the peninsula followed by relatively warmer and dryer flow (278 K and about 60-0 %) in the lee. The effect is more pronounced at 850hPa where air aloft of the slope reaches temperatures of 276 K and humidity approaching 0 % compared to 266-268 K and 80-100 % upstream. Air flow warmer and dryer than the surrounding atmosphere continues downstream to the domain edge on both levels.

At 850-hPa RH also shows a moist (varies between 40 % and 90 %) wake structure which broadens from a narrow point near the slope as it moves downstream. This

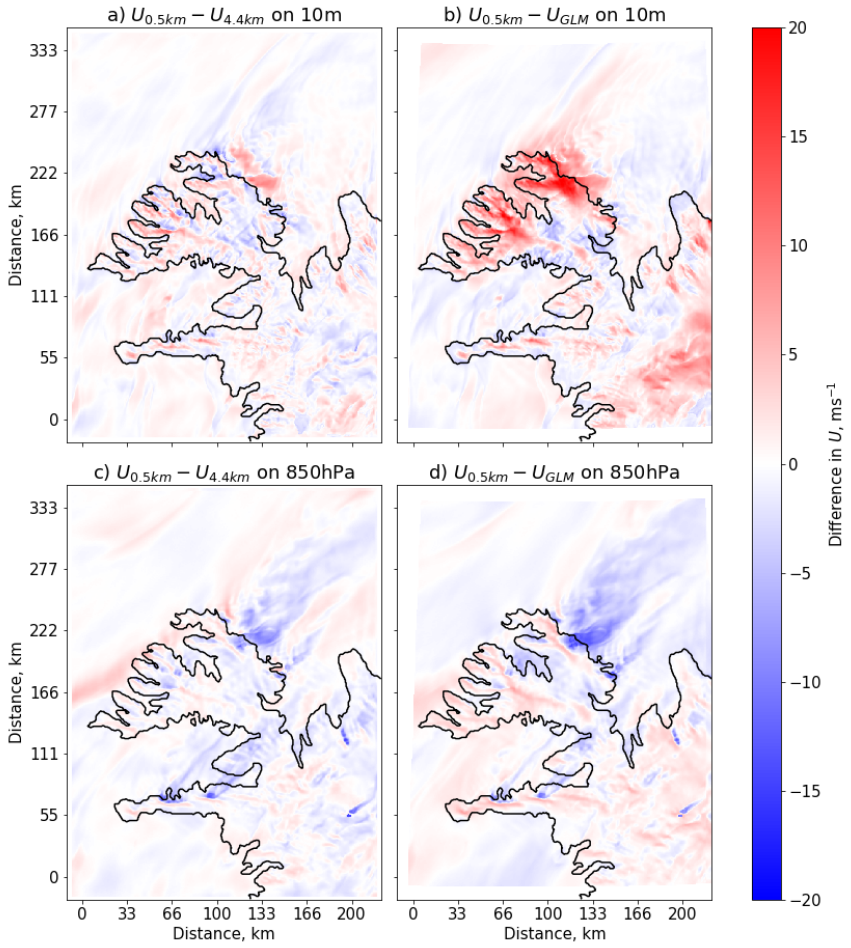

Figure 3.12: Horizontal slices of the horizontal wind speed difference (calculated by $U_{0.5\text{-}km}$–U_i where i is the coarse resolution) at 10-m (a, b) and on the 850-hPa pressure level (c, d) at 15Z forecast time. Left column (a,c) shows 4.4-km differences, right column (b,d) shows GLM differences. Negative differences mean the 0.5-km domain produced lower wind-speeds than the coarse domain, and positive differences show higher wind-speeds for 0.5-km. Units of y- and x-axis are kilometers.

structure corresponds to slightly cooler air in the 850-hPa temperature field and is flanked by wave patterns in the T and RH fields. Seeing these strong foehn-like effects and detailed lee-side features in the 0.5-km resolution T and RH fields we consider the differences relative to the coarser 4.4-km and GLM model fields.

Figures 3.12, 3.13 and 3.14 show the horizontal wind speed, air temperature and relative humidity differences (ΔU, ΔT, ΔRH), respectively, between a model simulation that resolves the mountain flow dynamic (the 0.5-km simulation) versus simulations that do not (the GLM and 4.4-km simulations) at 15Z. We recall from Section 3.2, equation 3.10 that the differences are calculated by $\Delta\Gamma_i = \Gamma_{0.5\text{-}km} - \Gamma_i$, where Γ is a variable such as U, T, or RH, and i denotes the coarse resolution, GLM or

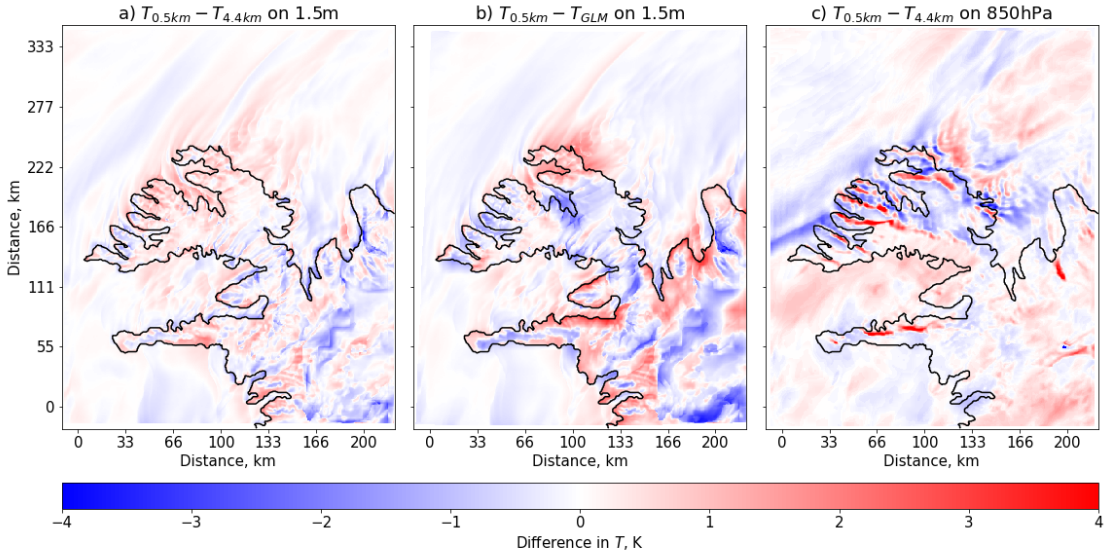

Figure 3.13: As in Figure 3.12, but for air temperature difference. Panels (a) and (c) show 4.4-km differences and panel (b) shows GLM differences at 1.5-m. Negative differences mean the 0.5-km domain produced lower temperatures than the coarse domain, and positive differences show higher temperatures for 0.5-km. 1.5-m temperatures (a, b) have been adiabatically adjusted to account for differences in model topography. This is not equivalent to calculating potential temperature, but instead the difference in surface elevation was accounted for using a constant adiabatic lapse rate of $6 * 10^{-3}$ K m^{-1}. Units for y and x-axis are kilometers.

4.4-km. At first glance at the difference fields we find that (i) the strongest differences are at the slope, and in all cases attenuate moving northeast out to sea, (ii) GLM differences are consistently higher than 4.4-km differences at the same level and and remain higher further downstream, and (iii) differences are consistently higher at 850-hPa than at surface level (10-m/1.5-m).

GLM differences in some cases reach magnitudes twice as high as the 4.4-km differences, particularly in the direct lee and above the slope, for example in Figure 3.12 the GLM difference in wind speed (ΔU_{GLM}) at 10-m is 20 m s^{-1} whereas it is 1-3 m s^{-1} for $\Delta U_{4.4\text{-}km}$ at 10-m. Similarly, the lee-side ΔU_{GLM} at 850-hPa varies between 10-15 m s^{-1}, while $\Delta U_{4.4\text{-}km}$ at 850-hPa falls between 5-10 m s^{-1}. At this point we note that the correspondence of negative wind-speed differences aloft and positive differences at 10-m (Figure 3.12) may point to a net downward flux of momentum in the 0.5-km domain.

Another example of the GLM differences being twice as high as the 4.4-km differences is in Figure 3.13 the GLM 1.5-m air temperature difference, ΔT_{GLM},

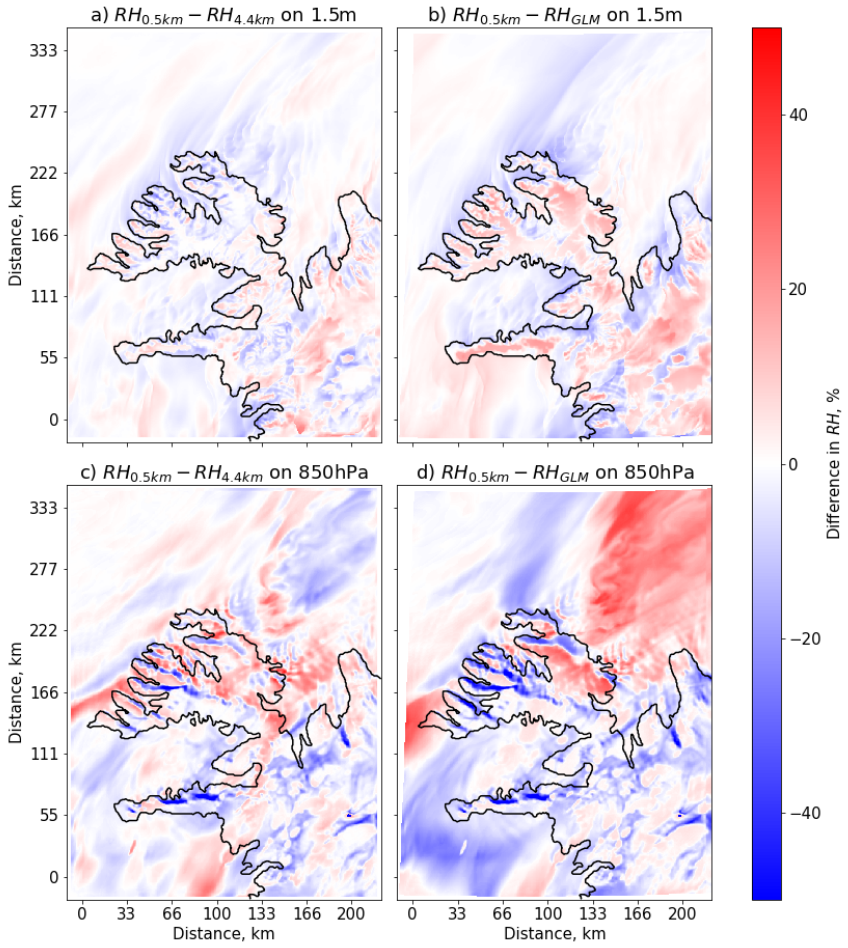

Figure 3.14: As in Figure 3.12, but for relative humidity difference. Negative differences mean the 0.5-km domain produced lower humidity than the coarse domain, and positive differences show higher humidity for 0.5-km. Note the difference in the colour-scales. Units for y and x-axis are kilometers.

reaches 2 K in the lee of the northern end of the ridge, while the corresponding 4.4-km difference, $\Delta T_{4.4\text{-}km}$, is at most 1 K in the same location. We note that ΔT_{GLM} and $\Delta T_{4.4\text{-}km}$ at 1.5-m level are both generally small (< 1 K) over the sea, which agrees with the findings that the temperature bias in the lower ABL discussed in Chapter 2 is relatively consistent across all domains (e.g. Figure 2.16, where all flight legs below 500 m altitude show a median θ-bias of 1.15 K). $\Delta T_{4.4\text{-}km}$ at 850-hPa varies between 3-4 K and -2- -3 K over the ridge and in the lee (Figure 3.13), supporting our finding that the differences at 850-hPa are more pronounced than at surface level.

The RH difference fields at 1.5-m in Figure 3.14 don't exhibit any significant variations between the 4.4-km and GLM differences, whereas they do reproduce contrasting patterns at 850-hPa. 4.4-km differences at 850-hPa shows an alternating

pattern of negative ($\Delta RH_{4.4\text{-}km} \geq -20$ %) and positive ($\Delta RH_{4.4\text{-}km} < 30$ %), potentially formed by the 0.5-km resolution resolving wave dynamics, which are not fully captured by the 4.4-km resolution. In contrast the GLM differences at 850-hPa show a horizontal plume with consistently positive ΔRH_{GLM} at 850-hPa ranging from 20 % to over 40 %, and it extends to the domain boundary (Figure 3.14).

The plume corresponds to the moist wake structure seen in Figure 3.11, suggesting that this structure is largely absent in the GLM RH field. This is the strongest example of resolution sensitivity affecting scalar transport (in this case of moisture) far downstream (i.e. over 100 km to the domain boundary) of a downslope windstorm. In Chapter 2 we saw vertical cross-sections of 0.5-km wind speed, potential temperature, and specific humidity; in Figure 2.11, which depicts the along wind cross-section showing the hydraulic jump in the horizontal wind speed panel, we can see in the specific humidity field that moisture is advected from the surface (where the hydraulic jump attaches to the surface) to the top of the ABL, producing a deep moist layer in the lee. Without a downslope windstorm with a hydraulic jump being reproduced by the GLM moisture won't be advected from the lower ABL in the GLM in the same way as in the 0.5-km simulation.

DECAY OF BIAS WITH DOWNSTREAM DISTANCE

Using the method from Section 3.2, the mean decay curves in Figure 3.15 were made. The purpose of this method is to account for the horizontal variability in the difference fields in the lee parallel to the ridge (illustrated by the black cross-section lines in Figure 3.1), and measure the mean differences parallel to the ridge as we move downstream. In order to determine how far the impact of the windstorm on the peninsula's wake reaches, we have to consider how quickly it recovers to the zero line (i.e. how quickly it *decays*). Alternatively, the lee-side differences may not tend to zero, but instead may tend to a different *equilibrium* value, if there is a systematic bias in the atmospheric state fields between the different resolutions.

We define this systematic bias in the differences across the whole domain as the mean domain difference. The mean domain difference is taken as the mean difference (for each 4.4-km and GLM) over the 0.5-km domain, and values are given in Table 3.1. We find that the mean domain differences are small compared to the differences seen in the cross-sections (Figure 3.12-3.14), e.g. $|\Delta U| < 1$ m s^{-1} for

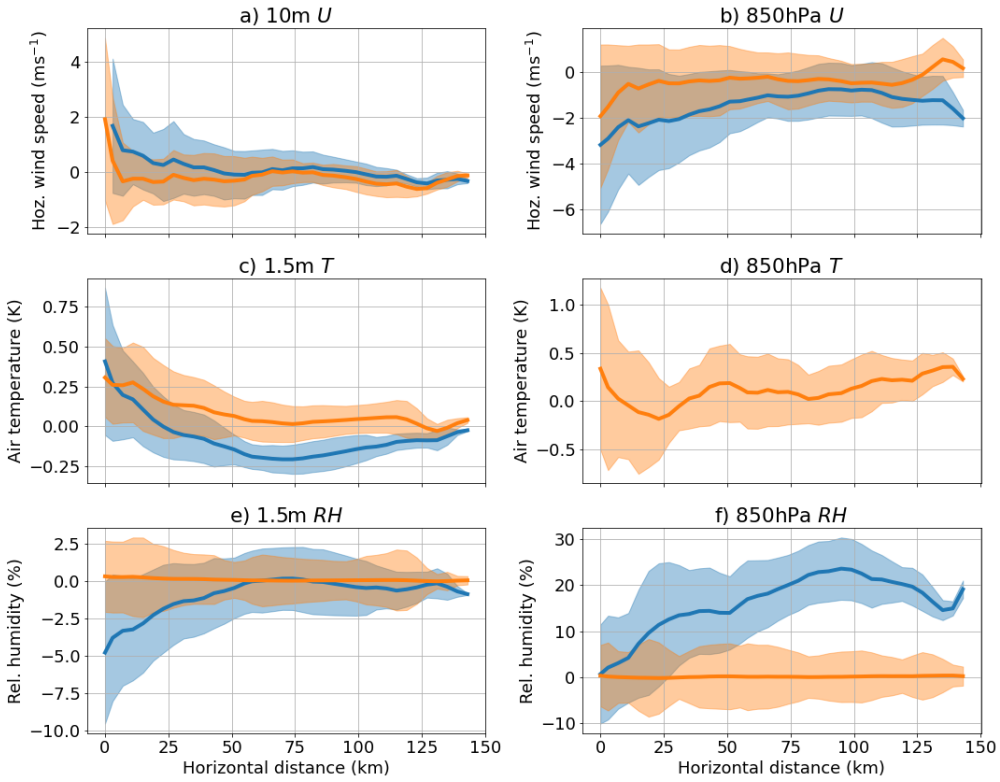

Figure 3.15: Decay lines of wind speed, air temperature, and relative humidity differences at 10-m/1.5-m level (a, c, e) and 850-hPa (b, d, f) and at at 15Z forecast time for 0.5-km - GLM (blue) and 0.5-km - 4.4-km (orange) with one standard deviation of each sample line (shaded) derived using the method described in Section 3.2.1. Due to a technical issue GLM air temperature at 850 hPa was unavailable (see panel d).

all resolutions and levels in Table 3.1, and that standard deviations in the field are generally several times larger than the magnitude of mean domain differences. This suggests that systematic biases in whole domain as a result of resolution sensitivity are not important, and we can still expect mean lee-side differences to decay to near zero in Figure 3.15.

At first glance, in most cases the highest mean difference is closest to the ridge shown in the decay lines in Figure 3.15, with the global driving model generally showing higher differences than 4.4-km, except for 1.5-m temperature. And generally both curves converge within 20 km to 130 km. This is in agreement with our assessment of the preceding horizontal cross-sections (Figure 3.12-3.14).

The steepness of the decay curves and the points at which they approach or cross the mean domain difference (or zero line) varies. For example, for 10-m wind speed in Figure 3.15 (a), mean $\Delta U_{4.4\text{-}km}$ falls from 2 m s^{-1} to just below zero over the first 5 km,

Variable, unit	10m/1.5m, 4.4-km	10m/1.5m, GLM	850hPa, 4.4-km	850hPa, GLM
ΔU, m s^{-1}	0.102 ± 1.47	0.838 ± 2.772	-0.27 ± 1.383	-0.308 ± 1.84
ΔT, K	0.014 ± 0.420	-0.034 ± 0.650	-0.002 ± 2.25	-
ΔRH, %	-0.592 ± 3.95	-0.191 ± 5.65	-0.431 ± 8.03	-0.338 ± 12.4

Table 3.1: Mean domain difference over 0.5-km domain at 15Z forecast time. Uncertainty given is the standard deviation of the difference field over the domain. Columns are named according to level (10-m/1.5-m for surface, and 850-hPa), and which grid the 0.5-km nested regional output is compared to (i.e. 4.4-km and GLM)

and roughly remains at that level until domain boundary, whereas mean ΔU_{GLM} falls more slowly than 4.4-km from about 2 m s^{-1} until it crosses the zero line at just below 50 km distance and converges with mean $\Delta U_{4.4\text{-}km}$. The decay curves in 10 wind speed (Figure 3.15 (a)) show a reasonably exponential decay towards the zero line, which is also seen in 1.5-m ΔRH_{GLM} (Figure 3.15 (e)), which exponentially decays from -5.0 % to 0 in just over 50 km.

However the behaviour of mean lee-side differences for T and 850-hPa RH do not follow this exponential decay pattern. For example, at 850-hPa (Figure 3.15 (d)) mean $\Delta T_{4.4\text{-}km}$ initially exponentially falls from less than 0.4 K t below zero, but then increases again after 25 km to near its initial value after 100 km. The mean lee-side differences in 1.5-m air temperature, where both curves are mostly parallel, suggest a systematic offset, which is greater than the equilibrium values Table 3.1 would suggest. Differences in RH for 4.4-km appear negligible compared to differences for the GLM, which increase until 100 km instead (Figure 3.15). This corresponds to the moist plume in RH at 850-hPa seen in Figure 3.11 and 3.14, which we suggested to have been formed by advection of moisture from the lower ABL to the top of the ABL based on our findings in Chapter 2.

Considering the curves seen in Figure 3.15, which we have discussed in this section, we find that the differences relative to coarse resolutions of the downslope windstorm in the 0.5-km simulation do not consistently reduce in an exponential manner from a maximum near the slope to zero downstream. Instead, the varying, and sometimes increasing, downstream differences seen in the decay-curves in Figure 3.15, imply that the reproduction of the downslope windstorm in the 0.5-km simulation could have an impact on the atmospheric state fields downstream, even if the differences initially appear to decay.

3.4.4 DIFFERENCES IN SUB-GRID TURBULENT HEAT FLUX

Oltmanns *et al.* (2015) found that resolution dependent differences in wind speed and temperature in the lee concur with differences in the modelled surface latent and sensible heat fluxes. They concluded that such changes in the strength and distribution of heat fluxes from the lack of well represented small-scale features, such as intense and narrow outflow from their valley system in Greenland, in their coarse resolution (e.g. 20 and 60 km) WRF models could have implications for correctly modelled deep-water formation over the Irminger Sea. Likewise, resolution dependent changes in surface heat fluxes in our model simulation could have similar implications for the modelled deep-water formation in the Iceland Sea.

The surface turbulent heat fluxes shown in Figure 3.16 show strong values on the lee-side slope where the downslope windstorm is most intense for both regional resolutions, but a key difference between the different runs appears on the slope-adjacent lee-side sea surface, where the 0.5-km run shows higher negative sensible heat flux values as well as higher positive latent heat flux values than the 4.4-km run, which shows a localised area of small turbulent heat fluxes instead. Oltmanns *et al.* (2015) found differences in lee-side surface sensible heat flux as high as 200 Wm^{-2} between their 60-km and 5-km WRF models and attributed it to resolved small-scale features like narrow outflow. Our lee-side surface sensible heat flux differences of $-$(30-40) Wm^{-2} (Figure 3.16) would suggest that even at comparatively high resolutions (i.e. 0.5-km and 4.4-km) the increase in resolving power is still important.

These fluxes may be attributable to the surface-level jets only resolved in the 0.5-km (and 1.5-km) simulation, which are notably dryer than the ambient flow (Figures 3.9 and 3.11). Further downstream both runs show similarly shaped wake structures, though the 0.5-km run shows fine structure patterns in sync with the 10-m wind speed differences in Figure 3.12. Stronger sensible surface heat flux values corresponding to higher 10-m wind-speeds are expected since the surface turbulent fluxes are related to the friction velocity $u_\star$ (labelled $v_\star$ in Lock *et al.* (2021)) which is a surface layer scaled velocity quantity (Lock *et al.* (2021)). The sensitivity of the surface flux field to fine structure in the wake is still noteworthy, and it is important to consider the impact of resolved surface jets or narrow outflows on the lee of mountains.

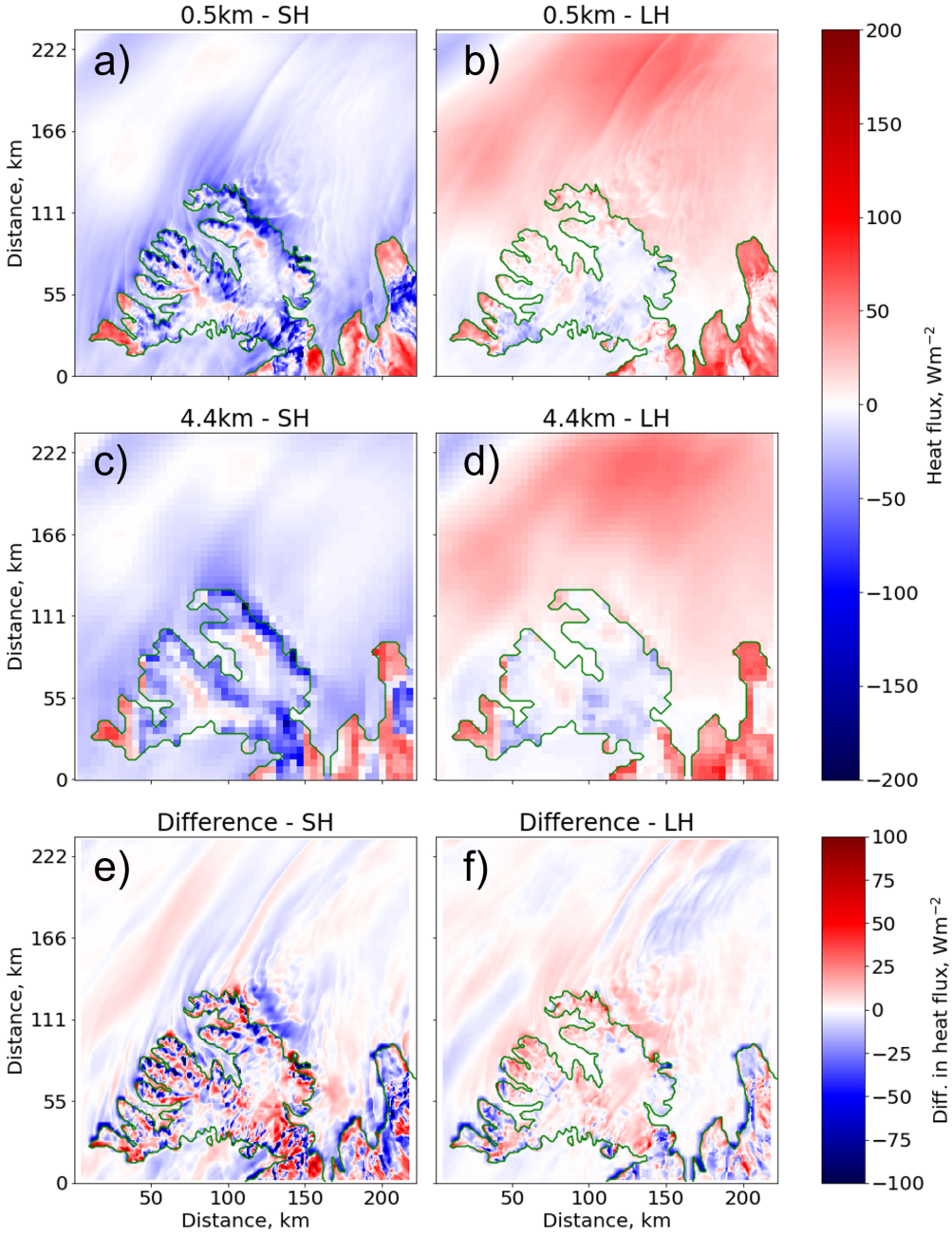

Figure 3.16: Maps of sub-grid upward surface sensible heat flux (SH, left) and upward latent heat flux (LH, right) at 15Z. a) and b) give the 0.5-km simulation, c) and d) the 4.4-km simulation, and e) and f) give the difference between the resolutions, where the coarse regridded field is subtracted from the 0.5-km field. The sign of the difference needs to be compared with the sign of the diagnostic flux. Negative (blue) difference on negative flux means amplification of flux. Horizontal axes given as distance in kilometers.

While the surface flux field appears to be sensitive to the fine structure in the wake, the surface flux parametrisation acts within a grid-cell and therefore does not have a horizontal dependency. However, some of the variables used in the flux parametrisation, in particular surface roughness, land use type, surface temperature and surface moisture, do vary horizontally. Some incorporated variables do not change during the model simulation, such as surface roughness and variables derived from the soil model - these quantities are set at the beginning of the simulation in the ancillary input. Low model level variables would also affect the flux parametrisations, and vary with time as well as horizontally, such as wind speed and temperature.

The relationship between all these input variables would give rise to the surface flux fields forming their own fine structures. Serafin *et al.* (2018) discuss that current micro-meteorological theory includes an assumption of horizontal homogeneity (as well as stationarity and near-constant turbulent fluxes along the vertical), which is violated over mountainous terrain. They go on to state that these assumptions could to be reassessed when studying turbulence in the future.

Elvidge *et al.* (2015) discussed that foehn jets in the Antarctic could have an enhanced warming effect on ice shelves if they are warm enough and occur frequently, potentially leading to increased melting. While there is no ice-shelf or sea-ice present in the bay during the time of the Iceland case study, or is there most of the year, coastal regions in higher latitudes, for example Greenland, have more semi-permanent sea-ice which could be affected.

Whether or not the modelled surface jets in the case study are a result of the downslope windstorm, or if they form more independently like traditional gap winds allowing air from lower layers to spill out onto the lee-side surface during more blocked conditions, they appear to be only resolved at a horizontal grid-spacing of 0.5-km in our case study. These jets modulate the lee-side surface energy budget, which has implications for environment processes and hazards, such as ice-shelf and sea-ice melt (e.g. Elvidge *et al.* (2015)), ocean deep-water formation (e.g. Petersen & Renfrew (2009); Oltmanns *et al.* (2015)), and wildfire generation (e.g. Smith *et al.* (2018)). A long-term or seasonal impact of the increased surface turbulent flux as a result of the modelled windstorm would need to be explored in a climatology (see Chapter 4).

3.4.5 SUMMARISING RESOLUTION SENSITIVITY

In this section we have investigated the downstream impacts of a downslope windstorm reproduced in the 0.5-km simulation relative to the 4.4-km and GLM simulations. We recall the first two questions set out in Section 3.1: (i) What is the effect of model reproduction of the downslope windstorm, and (ii) does the windstorm have a measurable effect on the large-scale flow? In order to answer these questions and determine the extent of the resolution-sensitivity in the lee-side effects of the reproduction of a downslope windstorm we assessed the differences between the 0.5-km and 4.4-km atmospheric state fields and sub-grid surface flux fields, and between the 0.5-km and GLM atmospheric state fields. We found that in many comparisons bands of measurable differences extended from the slope to the domain boundary: e.g. the 0.5-km simulation produced a wake 5-10 m s^{-1} slower than the GLM at 850-hPa (Figure 3.12), and it produced a broadening plume of moisture with RH values up to 40 % than in the GLM (Figure 3.14), while the 0.5-km also produced a wake 1-2 K warmer than 4.4-km at 850-hPa (Figure 3.13).

Examples of these cohesive bands of differences as well as the complexity in the lee-side mean differences, with some values increasing after falling to zero (Figure 3.15), imply that there are measurable downstream impacts of the reproduction of a downslope windstorm in the 0.5-km simulation relative to its representation in the 4.4-km and GLM simulations. Considering these differences often extended to the domain boundary, we cannot conclude that there is no effect on the large-scale flow in the Denmark Strait and Iceland Sea from the reproduction of a downslope windstorm over a mesoscale mountain range in a high-resolution simulation, since we do not know how far these differences extend beyond the boundaries of the 0.5-km domain.

We discussed that the coarser resolutions (4.4-km and GLM with 17 km grid-spacing) do not reproduce the resolved wave-dynamics of the 0.5-km model and that the smoothed topography of our coarser domains does not reproduce the steep slopes needed to induce the strong wave-response seen in the 0.5-km simulation; this is also discussed by Moore & Imrit (2022) and Oltmanns *et al.* (2015), who conducted similar resolution-sensitivity studies in the region. They also argued resolution-dependent differences in the model representations of downslope wind (here over Greenland) can have considerable downstream effects on the atmosphere.

For example Moore & Imrit (2022) showed that the ERA5 reanalysis (with 25 km grid-spacing) failed to reproduce the observed extreme wind conditions downwind of the steep topography in the Nares Strait, while Oltmanns *et al.* (2015) also argued that narrow bands of more intense wind and higher temperature flowing out from their valley, which are only resolved by their 5 km resolution WRF simulation, in south-east Greenland will modulate the surface energy balance in the Irminger Sea, with implications for modelled dense water formation in the area.

So far in this chapter and in Chapter 2 we have established the resolution-sensitivity of the downslope windstorm representation in our UM simulations. There are yet significant uncertainties in the downstream impacts investigated in this section, since we are only studying a single windstorm so far and modelled downslope windstorms are highly sensitive to initial conditions (e.g. Reinecke & Durran (2009)), which means that windstorms formed under slightly different atmospheric conditions may have very different downstream impacts. We will constrain this uncertainty, for example with a climatology in Chapter 4, and by changing the boundary layer parametrisation in our case study simulation, which will be discussed in detail in Section 3.5.

3.5 SENSITIVITY TO SUB-GRID TURBULENCE

The work in this section aims to address the final question of this chapter set out in Section 3.1: how sensitive is the windstorm's lee-side impact to changes in sub-grid-scale processes? To do so we will compare the wake structure in the 0.5-km longtail simulation (which we will denote as 0.5-km$_{\text{longtail}}$) to the control simulation (0.5-km$_{\text{control}}$) side by side for our atmospheric state variables, and use difference fields, which we recall from Section 3.2.2 are calculated by $\Gamma_{control} - \Gamma_{longtail}$, so we can compare the sensitivity in the reproduction of a downslope windstorm in the 0.5-km model with changes in the boundary layer stability function paramterisation and with its sensitivity to changes in resolution and dynamics.

We will also briefly evaluate the 0.5-km$_{\text{longtail}}$ simulation against the aircraft observations seen in Chapter 2 and compare its root mean square biases against those from the 0.5-km$_{\text{control}}$ simulation, to assess the relative fidelity of the two configurations. Studying the effect of turbulent flux parametrisations in the context

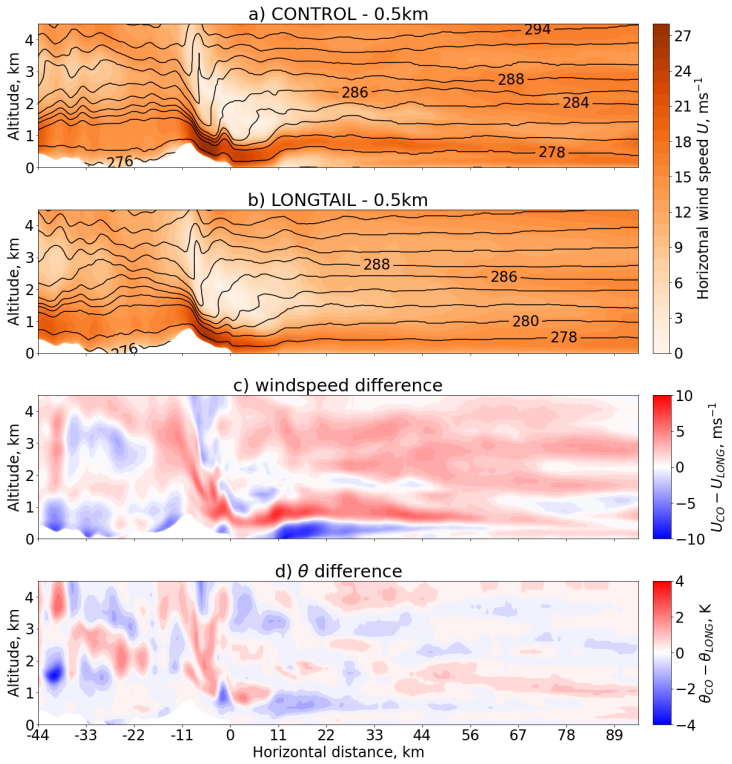

Figure 3.17: Along-wind vertical cross-sections of UM 0.5-km horizontal wind speed (colour scale) with potential temperature 2 K contours (black) for the control (a) and longtail (b) at 15Z forecast time, and their respective differences in wind speed (c) and potential temperature (d).

of orographic flow in the UM is one of the general aims of this thesis (Section 1.2.2), which the work in this section addresses and some of the findings may provide a direction for the development of potential parametrisations for lower resolutions.

DIFFERENCES IN WINDSTORM REPRESENTATION

To stay consistent with previous sections we will focus on outputs at 15Z forecast time. Figure 3.17 shows that the 0.5-km$_{\text{longtail}}$ windstorm at 15Z has a weaker hydraulic jump and a more diffuse wave-breaking region than 0.5-km$_{\text{control}}$. The key differences in the horizontal wind speed fields are a strong negative difference in the lee 10-40 km from the slope, where 0.5-km$_{\text{longtail}}$ produces a surface-flow up to 10 m s^{-1} stronger than 0.5-km$_{\text{control}}$. The control's resolution-based differences seen in Figure 3.12 do exceed that, but only close to the slope and not as far out as suggested in the longtail cross-section.

Higher up in the boundary layer at mountain crest level the impact is reversed and positive differences show 5-10 m s^{-1}. This appears to be a result of the weakening

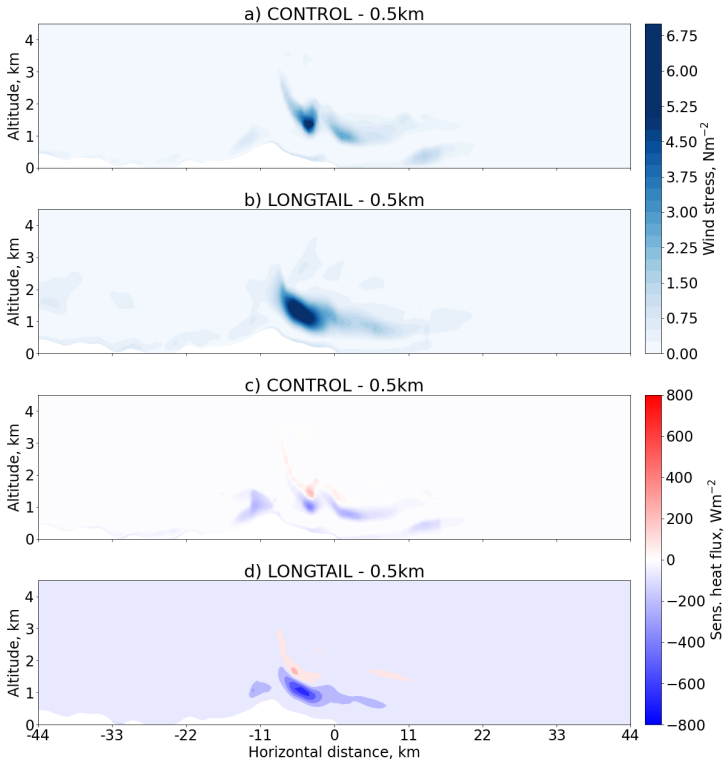

Figure 3.18: Along-wind vertical slices of windstress (a,b) and sub-grid (upward positive) sensible heat flux (c,d)in the UM 0.5-km horizontal grid-spacing runs for control (a,c) and longtail (b,d) configurations at 15Z forecast time.

of the hydraulic jump and an associated reduction in the altitude of the windstorm jet that forms downwind of the jump. Strikingly, this strong positive bias extends upward for several kilometers and continues horizontally downwind to the domain edge. Winds at slope are also weaker in 0.5-km$_{\text{longtail}}$, though not as dramatically as aloft. The potential temperature differences in Figure 3.17 show variable downstream differences of about 1-2 K, and an area of warmer air in 0.5-km$_{\text{longtail}}$ corresponds with the hydraulic jump.

The vertical cross-sections for windstress and sensible heat flux in Figure 3.18 demonstrate the key difference between the SHARPEST and longtail stability functions. As explained above, f_{stable} modifies the turbulent diffusivities by reducing their values, and by extension the sub-grid flux, in a stable atmosphere ($Ri > 0$). We can see that changing to longtail dramatically increases the extent and intensity of the area of high windstress indicative of the wave-breaking region aloft. The wave-braking region in the control formed a dipole in the sub-grid sensible heat flux, for which the negative flux region is has also significantly increased, suggesting

that the parametrisation is moving more heat downward into the slope than in the control run. Given this response, the longtail test can be considered suitable for the purpose of contextualising the variability and uncertainty of the model windstorm representation.

In terms of the previously discussed v_{cb} and $\hat{h}$, 0.5-km$_{\text{longtail}}$ also displays strong differences to the control. While 0.5-km$_{\text{control}}$ showed peak cross-barrier winds at 15Z, 0.5-km$_{\text{longtail}}$ demonstrates a gradually increasing cross-barrier wind from 6Z falling short of a mean cross-barrier wind speed of 18 m s^{-1} by 20Z (not shown). Despite that, the upstream conditions of both simulations as evident in the $\hat{h}$ time-series in Figure 3.7 appear to share the same variability and peaks. Both runs show highest cross-barrier winds during consistent values of $\hat{h}$ ~0.8-0.9 (not shown). Despite the upstream similarities the evolution of the windstorms diverges early in the forecast and the three-phase regime identified in 0.5-km$_{\text{control}}$ breaks down in 0.5-km$_{\text{longtail}}$, exemplified by the differences in the 0.5-km windstorm reproduction seen in Figure 3.17.

So far it is apparent that the differences in wind-speed and potential temperature between 0.5-km$_{\text{longtail}}$ and 0.5-km$_{\text{control}}$ (Figure 3.17) are comparable to some of the differences seen in the resolution sensitivity analysis in Section 3.4. To obtain a more comprehensive picture we will compare the horizontal cross-sections of 0.5-km$_{\text{control}}$ and 0.5-km$_{\text{longtail}}$ for wind speed, air temperature and relative humidity in Figure 3.19, 3.20 and 3.21, respectively. The two 10-m wind speed fields in Figure 3.19 look similar, with both 0.5-km$_{\text{control}}$ and 0.5-km$_{\text{longtail}}$ reproducing jet-like protrusions of relatively high wind speed from the base of the slope and a wave-like fine structure. The 0.5-km$_{\text{longtail}}$ wake does not get deflected like the 0.5-km$_{\text{control}}$ as described in Section 3.3. This is expressed as strong negative differences of up to 5 m s^{-1} (Figure 3.19 (c)) on the edge of the geostrophic jet flowing through the Denmark Strait. Conversely, a jet of positive difference (about 3 m s^{-1}) adjacent to this forms about 40 km downstream of the slope and continues to the domain edge.

At 850-hPa we see a similar contrast in the wakes, where 0.5-km$_{\text{control}}$ produces a more diffuse wake compared to 0.5-km$_{\text{longtail}}$'s more narrow bands of decelerated flow (Figure 3.19 (d,e)). In the 850-hPa wind speed difference field we see a band of negative difference (3-5 m s^{-1}) downstream flanked by positive difference to the south (Figure 3.19 (f)); this pattern is reminiscent of the wake in $\Delta U_{4.4\text{-}km}$ at 850-hPa seen

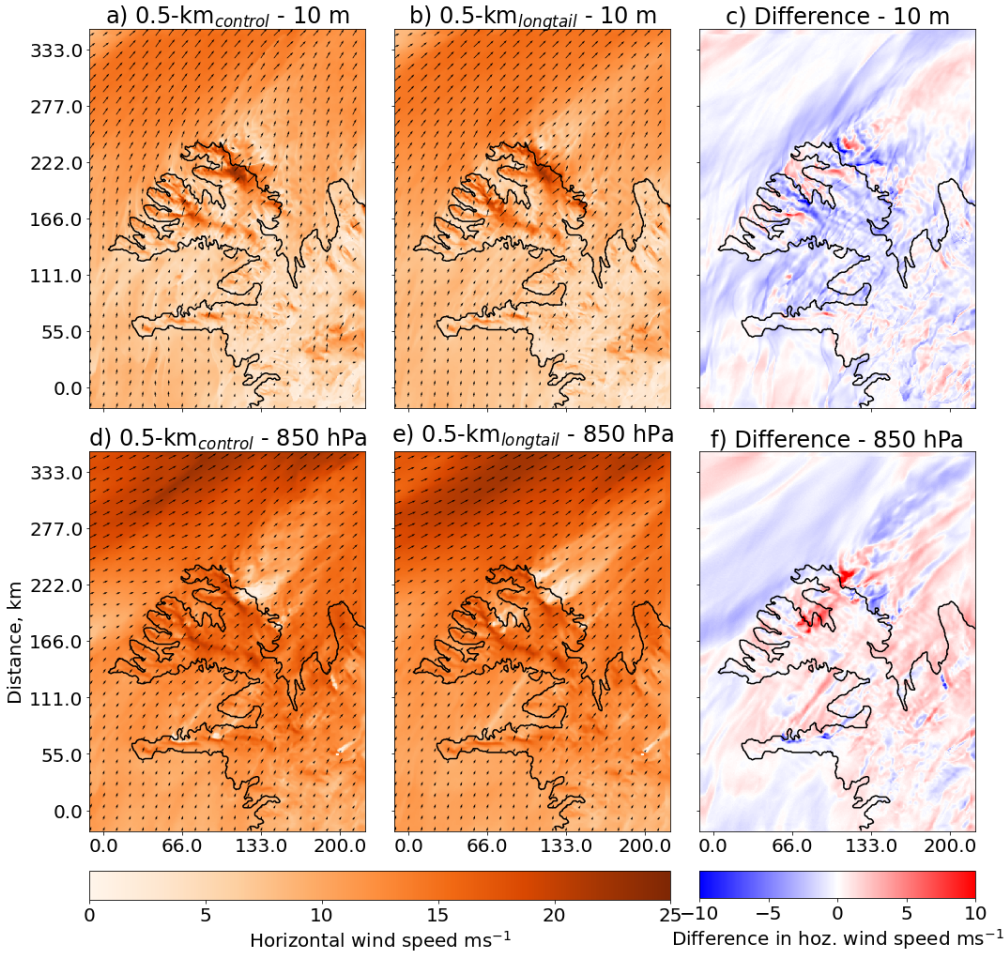

Figure 3.19: Horizontal slices for 0.5-km wind speed control fields (a,d), longtail fields (b,e), and 0.5-km$_{\text{control}}$-0.5-km$_{\text{longtail}}$ differences (c,f) on 10-m (a,b,c) and 850-hPa (d,e,f) levels at 15Z. Black contour is 0.5-km coastline. Axes are horizontal distance in kilometers. Quivers give horizontal wind speed and direction.

in Section 3.4 Figure 3.12, where a prominent band of negative (down to -5 m s^{-1}) wind difference extends from the slope to the domain edge and is also surrounded by ribbons of positive difference. At this point we note that the differences in wind speed between the 0.5-km and 4.4-km simulations and the differences between the 0.5-km control and longtail simulations produce similar magnitudes and patterns.

0.5-km$_{\text{control}}$ produces a cooler surface layer than 0.5-km$_{\text{longtail}}$ by up to 2 K difference, as seen by the predominantly negative differences at 1.5-m in Figure 3.20, which are similar magnitude differences as those seen in the 4.4-km- and GLM-differences in 1.5-m temperature discussed in Section 3.4 (Figure 3.13). Additionally, while both 0.5-km$_{\text{control}}$ and 0.5-km$_{\text{longtail}}$ show resolved wave patterns in the lee in the 850-hPa temperature fields, the corresponding difference field shows a plume of

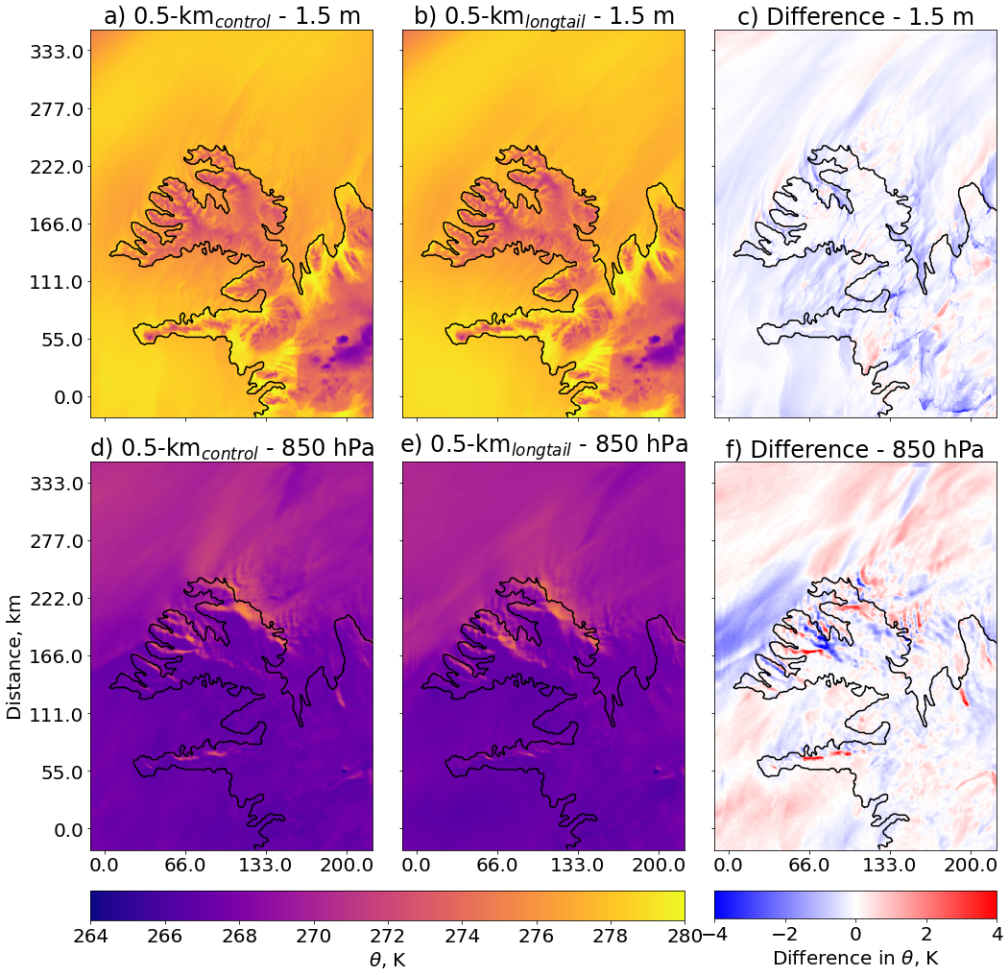

Figure 3.20: Horizontal slices for 0.5-km air temperature control fields (a,d), longtail fields (b,e), and 0.5-km$_{control}$-0.5-km$_{longtail}$ differences (c,f) on 10-m (a,b,c) and 850-hPa (d,e,f) levels at 15Z. Black contour is 0.5-km coastline. Axes are horizontal distance in kilometers.

predominantly positive difference (approximately 2 K) extending from the slope to the domain boundary, with some negative difference 20-30 km downstream (Figure 3.20 (d,e,f)).

This wake pattern in the 850-hPa temperature is also seen in the 4.4-km comparison (Figure 3.13) seen before, and both can be explained as follows: the hydraulic jump in 0.5-km$_{control}$ detaches from the surface and brings cooler air from the lower ABL aloft (as seen in Figure 3.17) creating a patch of negative difference 20-30 K downstream. Foehn-wind leads to warming near the slope and lee-waves like a hydraulic jump may encourage downward heat flux in the ABL by creating shear-generated turbulence (e.g. Hertenstein & Kuettner (2005)). Both the 4.4-km simulation and 0.5-km$_{longtail}$ reproduce a weaker hydraulic jump than 0.5-km$_{control}$ at 15Z and would not show the same effect. Nonetheless, the key point here is that the

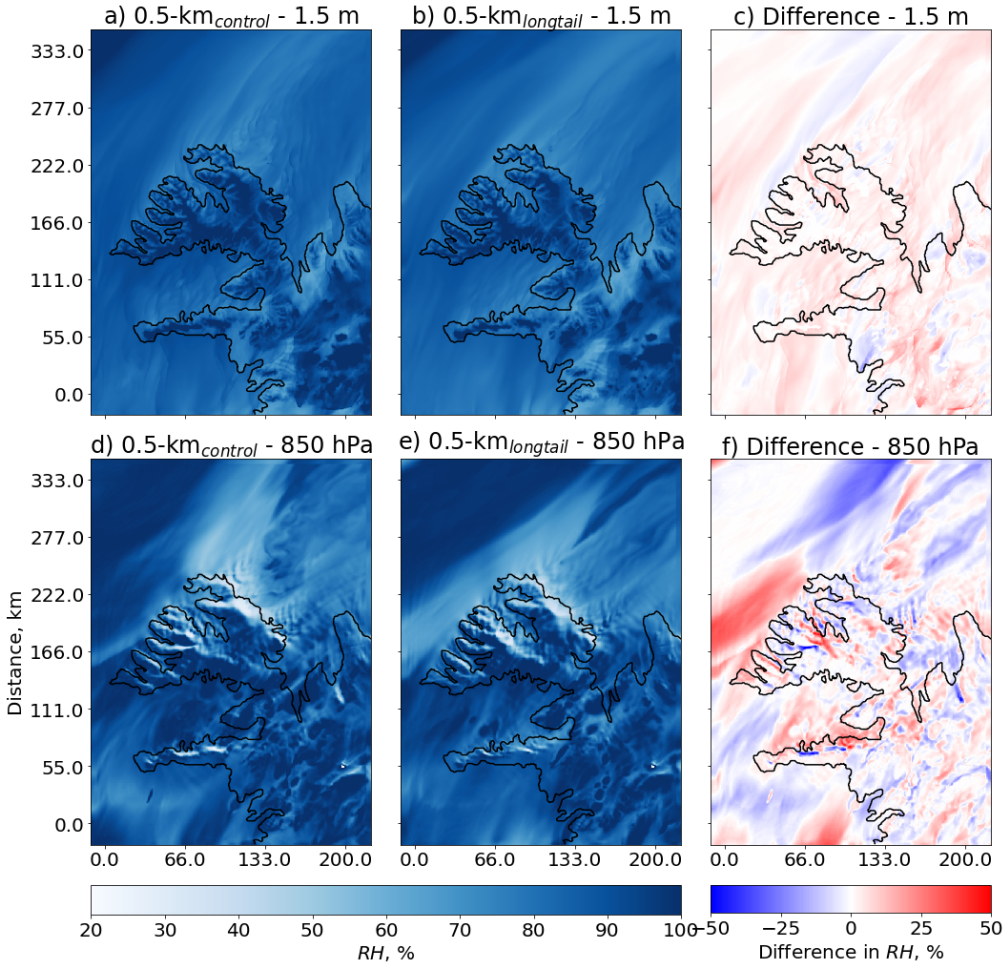

Figure 3.21: Horizontal slices for 0.5-km relative humidity control fields (a,d), longtail fields (b,e), and 0.5-km$_{\text{control}}$-0.5-km$_{\text{longtail}}$ differences (c,f) on 10-m (a,b,c) and 850-hPa (d,e,f) levels at 15Z. Black contour is 0.5-km coastline. Axes are horizontal distance in kilometers.

magnitudes and patterns in the temperature difference fields for the longtail analysis converge with those in the resolution sensitivity analysis.

0.5-km$_{\text{control}}$ and 0.5-km$_{\text{longtail}}$ produce very similar wake structures in the relative humidity fields at 1.5-m and 850-hPa (Figure 3.21, with foehn-drying clearly visible. The 1.5-m relative humidity difference field in Figure 3.21 (c) shows that the 0.5-km$_{\text{longtail}}$ atmospheric surface layer is up to 10 % dryer than 0.5-km$_{\text{control}}$ over most of the domain; we know that the presence of low-level moisture can strengthen a mountain-wave response (Jiang & Doyle (2009)), and if 0.5-km$_{\text{longtail}}$ has 10 % less relative humidity than 0.5-km$_{\text{control}}$ near the surface, it may partly contribute to the weaker wave response in 0.5-km$_{\text{longtail}}$ (Figure 3.17).

However, the 850-hPa relative humidity difference field (Figure 3.21 (f)) is more complex with an alternating pattern of positive and negative differences in the lee

reflecting the pattern seen in the 850-hPa temperature differences (Figure 3.20 (f)). This pattern bears a strong similarity with the difference-pattern seen in the 4.4-km relative humidity differences at 850-hPa (recall Figure 3.14 in Section 3.4). The 0.5-$km_{control}$ relatively dry wake encroaches on the moist flow (approaching 100 %) in the Denmark Strait producing negative differences up to 40 %near the northern domain boundary relative to the flow in 0.5-$km_{longtail}$. We recall from Section 3.4 Figure 3.14 that the GLM-difference in 850-hPa relative humidity also produced negative difference (around 20 %) adjacent to a large plume-like structure of positive difference in the lee of the ridge.

3.5.1 SUMMARISING TURBULENCE SENSITIVITY

We surmise that changes in the boundary layer stability function and changes to the resolution at a regional scale (i.e. a few kilometers at high resolution) seem to have a convergent effect. Similarities between the 0.5-$km_{control}$-0.5-$km_{longtail}$ and the 0.5-$km_{control}$-4.4-$km_{control}$ differences showcase a strong sensitivity of downslope windstorm representation in the UM to changes to the model sub-grid physics that is on par with the sensitivity to resolution and model dynamics. This means that there is significant uncertainty in the portrayal of downstream impacts of a resolved downslope windstorm on the boundary flow.

A mitigation method may be to run multiple sensitivity tests as an ensemble forecast. That technique would help to separate the inherent downstream impacts of downslope windstorms from the random noise produced in single forecasts. The perturbation conditions could be small changes in the initial conditions or changes in the boundary layer physics, as was done in the longtail test. The latter would be a valid way to account for the large differences in windstorm representation seen in this chapter, while still having the confidence that changes to the physics still produce downslope windstorms that can be integrated into an ensemble composite.

Another potential method to study the impact of downslope windstorms on the large scale circulation is through a climatology, using high resolution multi-year reanalyses that are capable of resolving a downslope windstorm on slopes like the one in this case study, and to use a sufficiently large number of events to account for the variability between them. This would be similar to the ensemble forecast method

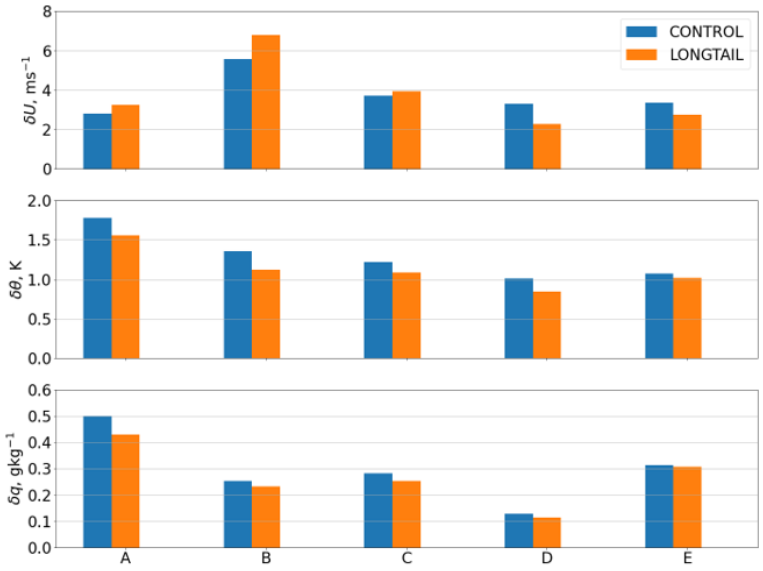

Figure 3.22: Root mean square biases for 0.5-km$_{\text{control}}$ (blue) and 0.5-km$_{\text{longtail}}$ (orange) compared to aircraft observations in five location dependent groupings used in Chapter 2. See Figure 2.10 for reference, but groupings are: (A) above mountain, (B) lee side within 20 km of ridge, (C) leeside along wind, (D) downstream MSA leg, (E) downstream saw-tooth. (A) includes flight legs above 2000 m altitude, while (B-E) are largely constrained to the lower 500 m of the lee-side ABL.

since naturally each event would be subject to a range initial and current conditions which can produce a downslope windstorm. This approach will be taken in Chapter 4.

3.5.2 LONGTAIL EVALUATION

Evaluating 0.5-km$_{\text{longtail}}$ against aircraft observations and comparing it to the results from Chapter 2 allows us to qualify the findings from Section 3.5 further. Figure 3.22 shows the root mean square (RMS) biases of the two high-resolution models (control and longtail) compared to aircraft observations for the same atmospheric state variables evaluated in Chapter 2 Figure 2.22. We note that 0.5-km$_{\text{longtail}}$ shows consistently lower RMS-biases than 0.5-km$_{\text{control}}$ for potential temperature and specific humidity in all areas of the flight, though differences between RMS-biases are comparatively small with the largest differences falling around 0.3 k for θ and less than 0.1 g kg^{-1} for q.

The control performs better than the longtail simulation for wind speed aloft of the mountains (group A) and in the immediate lee (groups B and C), with the strongest

difference in wind speed RMS-biases in the lee of about 1.5 m s^{-1} in favour of 0.5-$km_{control}$, but performs less well than the longtail simulation at the downstream legs in D and E. We recall that the inter-resolution differences in the control simulation's RMS-biases discussed in Chapter 2 are similar to the differences seen in Figure 3.22; for example, comparing 0.5-km and 4.4-km (Figure 2.22), wind speed RMS-biases differ by over 2 m s^{-1} at B and C, but are negligibly different elsewhere. Partly based on those RMS-biases in Chapter 2, we concluded that 0.5-km was a better simulation of the lee-side atmosphere than 4.4-km. We infer that 0.5-$km_{longtail}$ overall reproduces the atmospheric state over and in the lee of the Westfjords with slightly greater fidelity than 0.5-$km_{control}$.

The long-tail stability function was found to produce higher sub-grid scale turbulent mixing for high atmospheric stability than large eddy simulations and observations would resolve (Brown *et al.* (2008); Beare *et al.* (2006)), and was ultimately replaced in the MetUM operational configuration by the SHARPEST function (Lock *et al.* (2021)), which produces less sub-grid turbulence at a given stability (recall Figure 3.2). Despite this, the long-tail function has found recent applications, such as in Elvidge *et al.* (2017)'s modelling of clear air turbulence. At this point we recall one of the general aims of this thesis: to study the effect of turbulent flux parametrisations in the context of orographic flow in the UM. We have addressed this aim here: (i) we found that differences due to resolution-sensitivity and turbulence-sensitivity of the reproduction of a downslope windstorm are on par with each other, and (ii) we found that 0.5-$km_{longtail}$ reproduces the lee-side atmosphere with slightly greater fidelity than the control model (which uses SHARPEST).

We ask the question: Can a boundary layer stability function that produces more sub-grid turbulence than SHARPEST at a given stability effectively parameterise the downstream impacts of a downslope windstorm at lower resolutions if applied locally to the Westfjords? We do not know with certainty, and a more in-depth resolution-sensitivity study using the long-tail stability function would be needed to answer this.

3.6 CONCLUSIONS

In this chapter I have investigated the model representation of a downslope windstorm over the Westfjords on 19th March 2018 found in regional model simulations, with the aim to elucidate the lee-side impacts of downslope windstorms and their potential influence on the large scale flow. We described the windstorm's evolution through the 24 hour forecast and used the 0.5-km simulation as a truth for direct comparisons with the lower resolution configurations in the forecast run. Uncertainties in the model representation of the downslope windstorm were further considered by replacing the default boundary layer turbulence scheme with one employing a long-tail stability function that yields comparatively stronger turbulent mixing at a given atmospheric stability.

In the RA1M simulation the windstorm progresses through three distinct phases, with the later two at 15Z and 21Z forecast time identified by their high cross-barrier wind-speeds exceeding 18 m s^{-1}, deep hydraulic jump, and expanded wave-breaking zone aloft. The windstorm appears to be strongest during a period of consistent non-dimensional mountain height values varying minimally around 0.8, which suggest favourable conditions for downslope windstorm generation (Jackson *et al.* (2013)); consistent upstream conditions allow for a relatively strong windstorm to persist.

The regional atmosphere simulations capture a downslope windstorm, a hydraulic jump, and a wave-breaking region, but the 4.4-km simulation fails to resolve a surface jet spilling out to sea seen in the 0.5-km and 1.5-km simulations. The 0.5-km is necessary to resolve additional fine structure not seen in the other runs, such as short wavelength lee-wave signatures in the wake.

Inter-resolution differences in the wind, temperature, and relative humidity fields are strongest in the direct lee and close to the slope base, and most appear to attenuate to mean-field-difference levels within 100 km downstream. Complex interactions with the synoptic flow make this decay difficult to quantify. An aspect of the windstorm's downstream impact is the complete disruption of an elevated stable layer, that produced a more homogeneously and stably stratified boundary layer that extended to the 0.5-km domain edge.

The downslope windstorm evolution and representation differ greatly with increased sub-grid boundary layer turbulence. Differences due to the change in

sub-grid turbulence appear interchangeable with differences due to changes in resolutions of horizontal grid-point sizes of less than 10 km, though some similarities between the differences from longtail and those derived from the global driving model remain. This implies large uncertainties in the assessment of downstream impacts from the windstorm representation in the 0.5-km control simulation, since the representation of a downslope windstorm is shown to be highly sensitive to both changes in the model parametrisations as well as the different model dynamics emergent from different resolutions and the different complexities of orography at each resolution.

It is suggested that the uncertainty in the downstream impact analysis could be constrained by way of ensemble forecasts or a multi-year climatology using a high-resolution ($\ll$4.4-km grid-spacing) reanalysis product. The Met Office's current strategic aim is to move towards ensemble focused research (personal communication with Peter Sheridan (2022)), which is an encouraging convergence with my conclusions.

The key finding of this case study analysis is that the representation of a downslope windstorm and its impacts in a high resolution regional atmosphere simulation is highly sensitive to the model physics, dynamics, and orography, corroborating results from Reinecke & Durran (2009) and Oltmanns *et al.* (2015), while it still has measurable differences over 100 km downstream. The influence of the windstorm's wake on the large scale flow is difficult to quantify, however most notably the representation of the windstorm affects the relative humidity field in the lee and in the Denmark Strait, which has implications for precipitation, and moisture and heat transport further downstream. For example, future work could aim to quantify the difference in the mass of water that is precipitated over the Iceland and Greenland seas in the presence of upwind downslope windstorm activity.

4

CLIMATOLOGY OF STRONG WIND EVENTS IN THE WESTFJORDS

4.1 INTRODUCTION

Previously we evaluated a short-range NWP forecast from the Met Office Unified Model in Chapter 2 and used its high-resolution regional simulations to study the downstream impact of varying representations of a southwesterly downslope windstorm on the coastal slopes of the Westfjords and its implication on downstream momentum and scalar transport in the lower atmosphere in Chapter 3. The aim of this chapter is to give climatological context to the case studies, and to evaluate the impact of such windstorms on the climate in the region.

4.1.1 HIGH-RESOLUTION WINDSTORM CLIMATOLOGY

Our results from our UM model evaluation in Chapter 2 showed an increase in fidelity with increasing resolution, providing evidence that a similar improvement in the representation of downslope wind events can be expected from increasing resolution of reanalyses. Moore (2021) verified the surface-level wind fields in the Nares Strait off northwest Greenland from the eERA5 (an ensemble reanalysis), ERA5 (reanalysis) and ECOA (operational analysis) datasets (60 km, 31 km, and 9 km grid-

spacing respectively) against ground-based observations, and concluded that high resolution models are required to model the wind fields with fidelity, emphasizing that higher resolutions are needed to resolve the local topographic gradients and the mean sea-level pressure field to reproduce the observed ageostrophic winds. While the Nares Strait is far away from Iceland and exhibits a relatively unique geography, meaning optimal resolutions may differ between the regions, these results reflect what is described in Chapter 2 and 3.

A relatively new high-resolution (2.5-km horizontal grid-spacing) dataset is the C3S Arctic Regional Reanalysis data-product (CARRA), which uses the HARMONIE-AROME model, an operational non-hydrostatic NWP model used by the Danish- and Norwegian Meteorological Institutes (Bengtsson *et al.* (2017); Køltzow *et al.* (2022)). CARRA also uses ERA5 reanalysis fields for the lateral boundary conditions on the borders of its two regular Lambertian grid domains, CARRA-East and CARRA-West.

Since it is a novel product, the CARRA dataset has not been extensively tested in published work. Notwithstanding, Køltzow *et al.* (2022) has evaluated CARRA's performance compared to ERA5 (Hersbach *et al.* (2020)), against ground-based observations in the European Arctic spanning Norway and Svalbard and found that it represented surface-level air temperature and wind speed significantly better than ERA5. They also found that it improved on the representations of specific weather events, such as polar lows, although there is some regional heterogeneity in the level of bias shown compared to observations. Moore & Imrit (2022) built on the work of Moore (2021) and applied the CARRA dataset to their climatology of extreme ageostrophic winds in the Nares Strait northwest of Greenland, concluding that a sufficiently high resolution model is needed to represent the flow through the Strait well enough; particular value is added from CARRA's ability to resolve the narrow channel (40-100 km width) and the steep slopes of Greenland banking it with greater accuracy than ERA5 and similar coarse global reanalysis products.

4.1.2 CHAPTER OUTLOOK

The motivation for this chapter is to use a novel high-resolution reanalysis product to study downslope windstorms, like the one detailed in Section 4.1.1, which need small horizontal grid-spacing of order 1 km to be effectively represented in a NWP

model. I chose the Copernicus Arctic regional reanalysis (CARRA) for this purpose, as it has a resolution of the same order of magnitude as the UM regional high-resolution simulations in Chapters 2 and 3 and covers the area around Iceland. I have explored ERA5 reanalyses and ASCAT satellite observations to compliment the high-resolution reanalysis product, however due to the coarse resolution (31 and 25 km grid-spacing), and the limited spatio-temporal availability of the latter, I have determined they do not add sufficient value to the analysis at this time and decided to exclude them.

The questions addressed in this chapter are:

- What is the climatological context of the case study presented in Chapter 2 and 3?
- How useful are available diagnostic tools for indicating a strong wind event?
- What are the downstream impacts of downslope windstorms in the Westfjords?
- Can a climatology using a high-resolution atmospheric reanalysis mitigate the uncertainties from the boundary layer turbulence sensitivity, spatial heterogeneity, and synoptic influence discussed in Chapter 3?

The site of interest is the Drangajokull Glacier at the north-eastern coastal stretch of the Westfjords, shown in Figure 4.1; the windstorm studied in the previous chapters takes place on and above its northeastern slopes. The glacier sits at the crest of the ridge and, for simplicity, will be referred to as "the ridge" for the remainder of this chapter.

4.2 METHODS

4.2.1 REANALYSIS

This climatology study uses the novel high-resolution C3S Arctic Regional Reanalysis data-product (CARRA), which has a horizontal grid-spacing of 2.5 km and 3-hourly diagnostic outputs. It is hoped to reproduce downslope windstorms that occur on the Northwestern slopes of the Westfjords. While the CARRA-West domain (Figure 1.1) covers much of the Arctic seas, Greenland, Jan Mayen, and Iceland, the domain shown in Figure 4.1 is a subset for the purposes of this study. The

CARRA dataset is created using the HARMONIE-AROME non-hydrostatic regional NWP (Bengtsson *et al.* (2017)), forced at the boundaries by ERA5 and constrained by observations where available. It should be noted that in the coastal area of the Westfjords there is a relative lack of ground-based monitoring sites, compared to other regions of Iceland which see strong wind events occur with regularity; this is largely due to the remoteness of the region and lack of settlements and infrastructure along the slope that would otherwise be affected.

CARRA offers reanalysis and forecast products on single, model, height, and pressure levels, however due to the data volume I chose to be selective, settling for reanalysis fields on 2-m, 10-m, 850-hPa and 900-hPa levels for my analysis. This choice of levels harmonises with the case study analysis in Chapter 3, where most horizontal fields shown were cross-sections at the 850-hPa and 10-m or 1.5-m levels. The UM scalar surface variables, such as air temperature and relative humidity, are calculated at 1.5-m height, whereas the CARRA single level scalar fields are calculated at 2 m.

To minimise computational cost and to save time, the CARRA dataset will be briefly evaluated against the UM case study from Chapters 2 and 3, which in turn has already been evaluated against aircraft data as well as other observation sources, and is therefore a suitable truth simulation to compare CARRA against.

4.2.2 CRITERIA SAMPLING AND DERIVATION

The three main criteria used in the detection of downslope windstorms (Abatzoglou *et al.* (2020)) are the cross-ridge velocity v_{cb} measured just above crest height, stratification of the layer above crest height $\frac{\delta\theta}{\delta z}$, and the non-dimensional mountain height $\hat{h}$ ($\frac{Nh}{U}$) measured upstream. To minimise computational load v_{cb} is simply evaluated using the same method as in Chapter 3 on the 850-hPa level, which has a typical altitude of 1400 m, about 400-600 m above the typical mountain height in the peninsula. The v_{cb} sample is constrained to grid-points above the ridge, where the surface altitude is above 500 m. $\frac{\delta\theta}{\delta z}$ and $\hat{h}$ are evaluated using both the 850-hPa and 900-hPa surfaces which varies around crest height. $\frac{\delta\theta}{\delta z}$ is calculated the same sampling area as for v_{cb} for use as a criterion. $\hat{h}$ is sampled upstream in the area defined by Figure 4.1. Recall $\hat{h}$ derived from UM data is calculated using the method

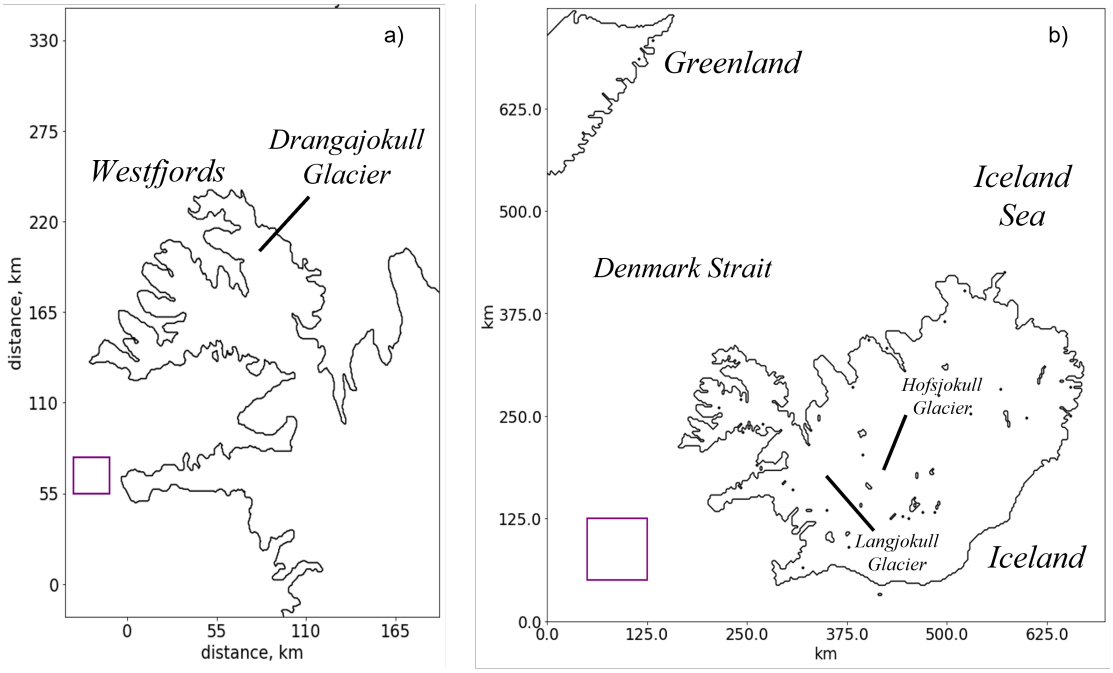

Figure 4.1: Maps of model regions with the upstream sampling area (purple rectangle) used for $\hat{h}$ marked for the UM 0.5-km simulation (a) and CARRA reanalysis (b). Axes are horizontal distance on a regular grid. Key geographical locations are labelled for reference, and will be referred to in this chapter.

described in Section 3.2.3.

In this climatology we will also use U_{slope} sampled on the lee-side slope below 700 m as an indicator of windstorm activity. In Chapter 3 a strong downslope acceleration was seen in the case study event, and while it is not a criterion based in windstorm theory, it is often either considered alongside other variables or directly measured with ground-based instruments and therefore available to researchers (Abatzoglou *et al.* (2020)).

4.2.3 CONDITIONAL SAMPLING

The CARRA reanalysis data is passed through several conditional sampling stages. The first stage is directional sampling, where time-points with wind components sampled above the ridge of interest (using the same sample area as for the v_{cb} derivation) returning a mean wind direction between 202.5° and 247.5° (using convention) are passed. The range of wind direction selects southwesterly winds in a reasonably narrow 45° arc. The cross-barrier wind speed v_{cb} is the component of the wind field U at crest height that is normal to the long axis of the mountain ridge.

The next stage of conditional sampling sees the data subjected to one of or a combination of the following conditions:

- cross-barrier wind speed: $v_{cb} > a$,
- 10m downslope wind speed: $U_{slope} > b$,
- stratification aloft: $\frac{\delta\theta}{\delta z} > c$
- and non-dimensional mountain height: $d < \hat{h} < e$,

where a, b, c, d and e are threshold constants to be determined.

The last conditional sampling stage used in this chapter is to only count individual events that have at least two consecutive time-points satisfy the conditions above, but have no more than three time-points of interruption in their duration; events that have several time points that satisfy the windstorm conditions, but have short breaks dispersed in them are considered single events rather than a collection of multiple closely spaced events. This means that sampled events are always over 9 hours spaced apart and that single random time-points satisfying conditions are isolated as noise. The case study event studied in the previous chapter appeared to last most of the forecast day, with the most intense periods spanning about 6-9 hours, so the above rules are reasonable.

4.2.4 CALCULATING HORIZONTAL WIND SPEED

When horizontal wind speed is averaged across time, for example for a composite, it is calculated in a particular order across all chapters in this thesis. For horizontal wind velocity components u (northward) and v (eastward) at time t we apply quadrature to obtain

$$U(t) = \sqrt{u(t)^2 + v(t)^2} \tag{4.1}$$

where $U(t)$ is the scalar wind speed at a particular grid-point or flight run at time t. U is sometimes notated as wsp, and is sometimes also spatially averaged, depending on application - this will be clarified when done so. To obtain the time-averaged composite, $U(t)$ is then simply averaged across all defined time-steps.

4.3 EVALUATION OF CARRA DATASET AND CRITERIA VALIDATION

In this section and Section 4.3.2 and 4.4 only springtime (MAM) data will be shown and discussed, since in most cases MAM and DJF produced results that are visually difficult to distinguish, and our case study took place in March. In Section 4.6 events will be counted in both seasons, and the longest three cases between both seasons are discussed as examples.

In this section, the reproduction of the 19 March 2018 downslope windstorm by CARRA will be explored and evaluated using the UM RA1M 0.5-km regional model simulation. The UM 0.5-km regional simulation has been extensively evaluated against ground-based and aircraft observations in Chapter 2 where Figures 2.11 and 2.14 in particular support the existence of a downslope windstorm with a hydraulic jump. We concluded that a downslope windstorm was modelled with reasonable fidelity. The resolution and longtail sensitivity experiments in Chapter 3 then demonstrated the high sensitivity of the windstorm model representation to parametrisation in the boundary layer physics and changes in the model dynamics and orography. While both the UM regional atmosphere and HARMONIE-AROME use a non-hydrostatic dynamical core with a deep atmosphere, CARRA has more smoothed orography than the UM 0.5-km simulation, and a horizontal grid-spacing five times larger than set up for the MetUM here. These factors will influence the representation of the windstorm in the reanalysis, especially since observation sources in the area are sparse, which would otherwise be assimilated into the reanalysis. Evaluating the CARRA reanalysis against the UM 0.5-km simulation will allow us to determine appropriate conditional sampling thresholds to count downslope windstorm events in the dataset.

4.3.1 EVALUATING THE CASE STUDY ATMOSPHERE

SELECTING WIND DIRECTION

Figure 4.2 indicates the prominence of winds at the ridge of interest that may allow for the formation of a downslope windstorm. There is a bimodal wind direction distribution on roughly the NE-SW axis. For a southwesterly downslope windstorm

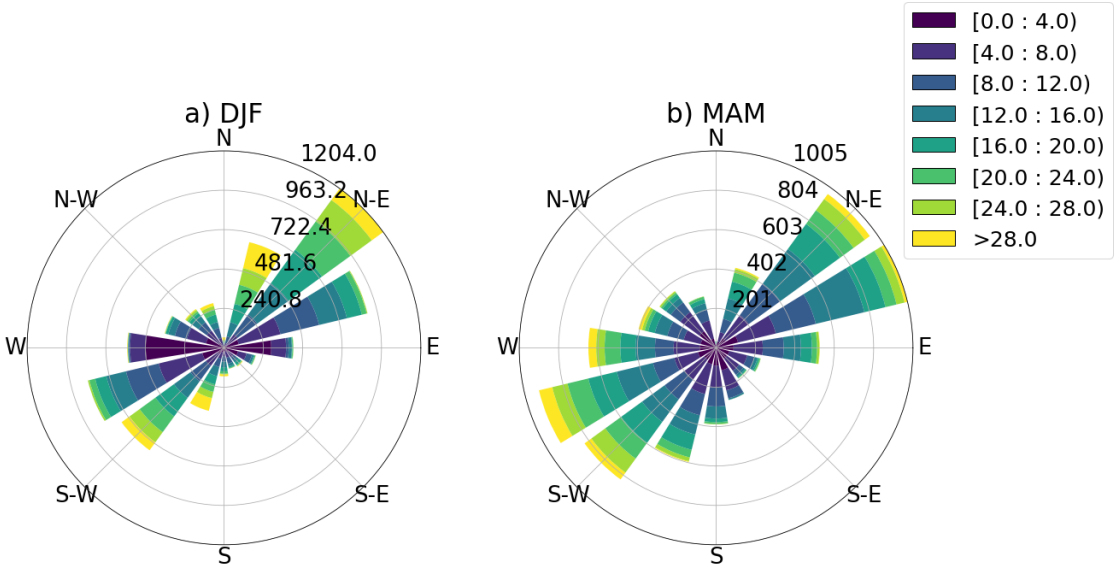

Figure 4.2: Windroses of CARRA horizontal wind, U, at 850-hPa over the ridge using grid-points with surface-altitude above 500 m, sampled from DJF and MAM seasons over 2010-2020. Colour-values are in m s^{-1} and bin-values are number of 3-hourly CARRA-outputs. The legend shows the wind speed values of the bin edges.

as seen in the previous chapters to be generated we need to select for time-points where the mean wind direction was roughly perpendicular to the ridge, which is approximately 45° to the y-axis of the reanalysis's regular x-y grid, to allow for high values of v_{cb} to be resolved, and where the wind direction is in the southwesterly quadrant. The data shown in Figure 4.2 further supports the chosen range of wind angles is 202.5° and 247.5° and all subsequent results shown will have been conditionally sampled with it. Out of approximately 8000 available time-points in the MAM dataset, 1595 time-points are selected, representing about 20% of the data.

MODEL COMPARISON DURING CASE STUDY

On the case study date, the CARRA dataset shows similar progression of upstream $\hat{h}$ to the UM, with a peak between 1.1 and 1.2 in the morning around 8-9Z, and a reduction in $\hat{h}$ around midday to values of 0.8 and below (Figure 4.3). While the UM remains roughly stable around 0.8, CARRA drops as low as 0.6 before rising to 1.0 again. This could suggest a regime shift in CARRA as the day progresses, while the windstorm in the UM simulation entered it's strongest state in the afternoon. One non-model specific explanation of the divergence is the different sampling locations for $\hat{h}$, as shown in Figure 4.1: the sampled atmosphere in the UM could have been significantly influenced by the nearby orography.

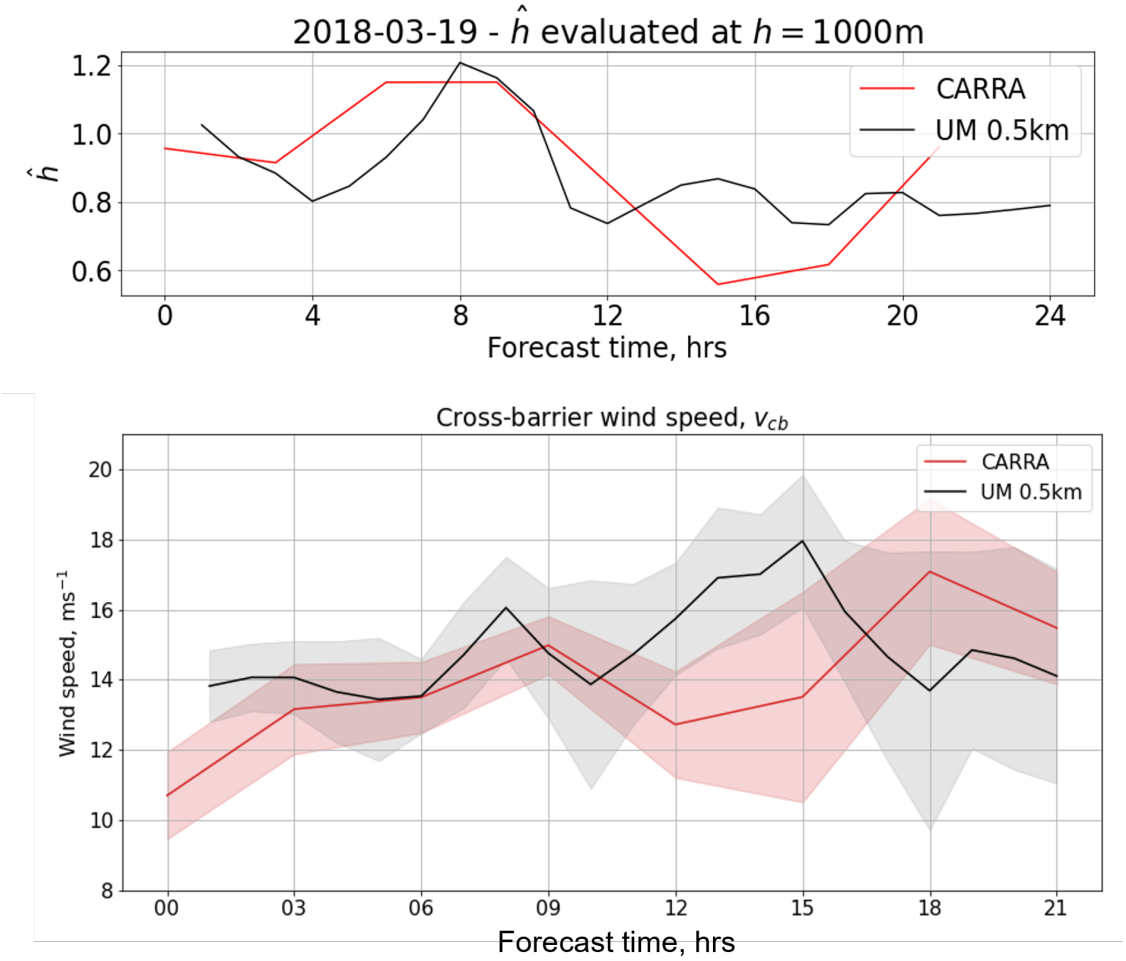

Figure 4.3: $\hat{h}$ (top panel) and mean v_{cb} (bottom panel) comparison between CARRA reanalysis (red) and UM 0.5-km regional simulation (black) over the case study date (19th March 2018). $\hat{h}$ is evaluated for a mountain height of 1000 m for both models. Shaded area in v_{cb} panel represents one standard deviation from the ridge sample used in the calculation and is included to account for spatial heterogeneity of flow acceleration across the ridge. X-axes represent time of day in hours.

This arose due to the domain constraints and the need to remove the sampling area away from the land when possible for more accurate sampling. It is also important to note the different methods of derivation for the quantity, where CARRA used a simplified two-point method using the 850-hPa and 900-hPa surfaces to derive the Brunt-Väisälä frequency N, while we took averages over several closely spaced model levels for the UM. Nonetheless, both models show a similar evolution through the day.

Both models also show a similar start to the case study for v_{cb}, although CARRA generally produced lower cross-ridge wind velocities, except after 15Z. The standard

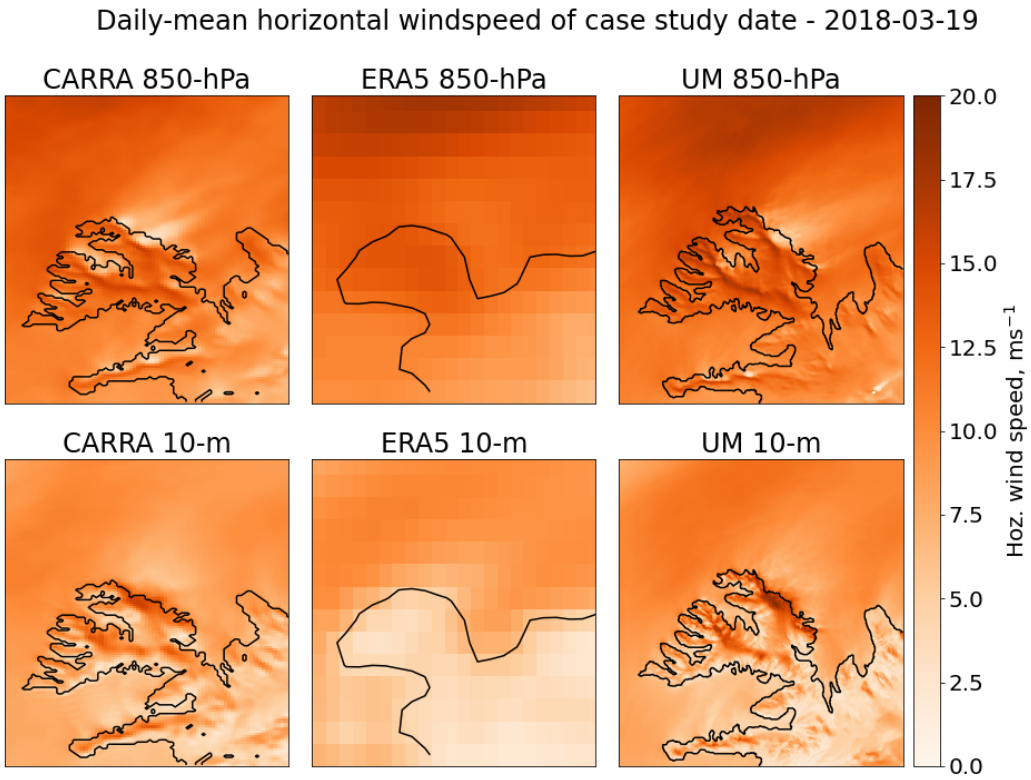

Figure 4.4: Horizontal slices of horizontal wind speed U at 850-hPa (top row) and 10-m (bottom row) averaged across available outputs across the case study date (19th March 2018). Models compared are the CARRA (left) and ERA5 (middle) reanalyses with 2.5 km and 31 km horizontal grid-spacing respectively, and the UM regional 0.5-km grid-spacing simulation (right).

deviations of both samples also show that the UM almost consistently produced faster wind-speeds during the day. CARRA $\hat{h}$ is very similar to the UM $\hat{h}$ in Figure 3.7 in Chapter 3. This hints at the high sensitivity of downslope windstorm representation in NWP models to the model physics and initial conditions, also seen in other studies (e.g. Reinecke & Durran (2009)).

On average through the day CARRA and the UM 0.5-km simulation show similar downslope acceleration and a zone of stagnant air at 850-hPa directly aloft of the slope reminiscent of wave-breaking, with a wake trailing at least 100 km downstream, as shown in Figure 4.4. We cannot say for certain that CARRA models wave-breaking, since we would need detailed vertical cross-sections showing overturning in the isentropes for that. Despite these similarities, CARRA produces mean slope 10-m wind speeds almost 5 m s^{-1} lower at the crest than the UM, similarly to the 4.4-km resolution regional atmosphere simulations in Chapter 3. Very similar to the

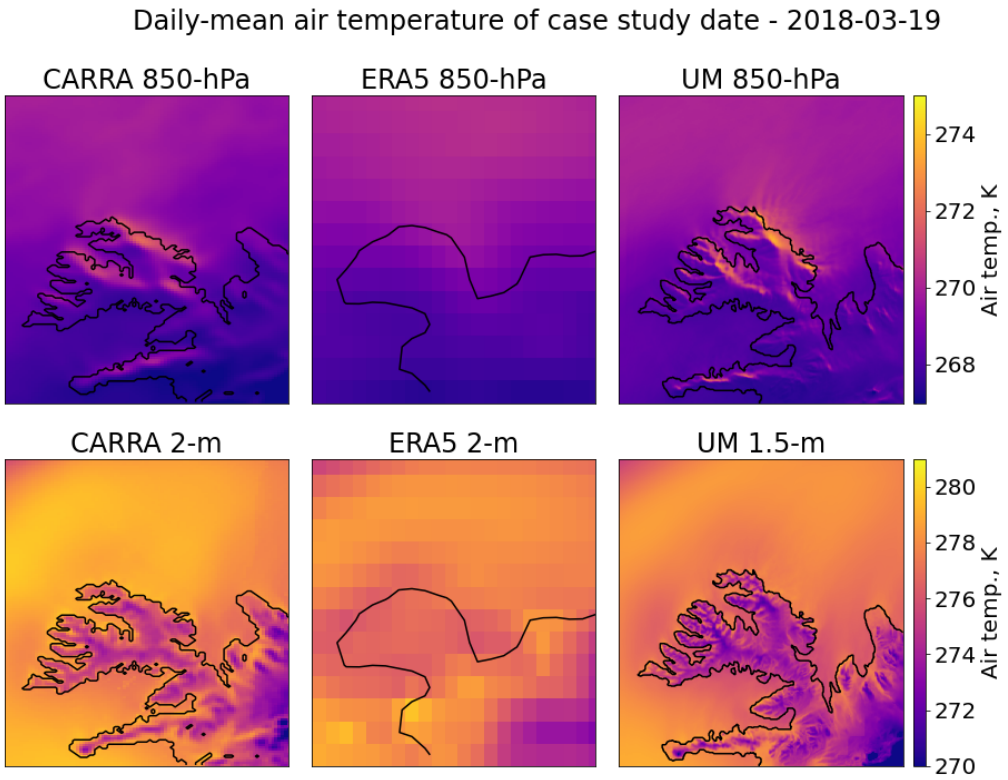

Figure 4.5: Horizontal slices of air temperature T at 850-hPa (top row) and 10-m (bottom row) time-averaged across available outputs across the case study date (19th March 2018). Models compared are the CARRA (left) and ERA5 (middle) reanalyses with 2.5 km and 31 km horizontal grid-spacing respectively, and the UM regional 0.5-km grid-spacing simulation (right).

UM global driving model discussed in the previous chapter, the ERA5 reanalysis, which provides the lateral boundary conditions for the CARRA domain, does not reproduce any visible downslope windstorm signatures in the horizontal wind-field, demonstrating the need of high-resolution reanalysis products to study windstorm events of this scale.

Both CARRA and UM show Foehn warming in the lee near the slope, shown in Figure 4.5, although the UM shows temperature values in the wake at 850-hPa at least 2 K higher than CARRA, as well as more fine structure, while CARRA has an overall warmer mean temperature field above the sea surface at 2-m. ERA5 also shows some lee-side warming, and appears to agree with the higher resolution datasets further downstream, illustrating the limited nature of the foehn wake in this case.

Considering both the temperature and wind fields, the CARRA dataset reproduces a downslope windstorm on the case study date, with a decelerated region and

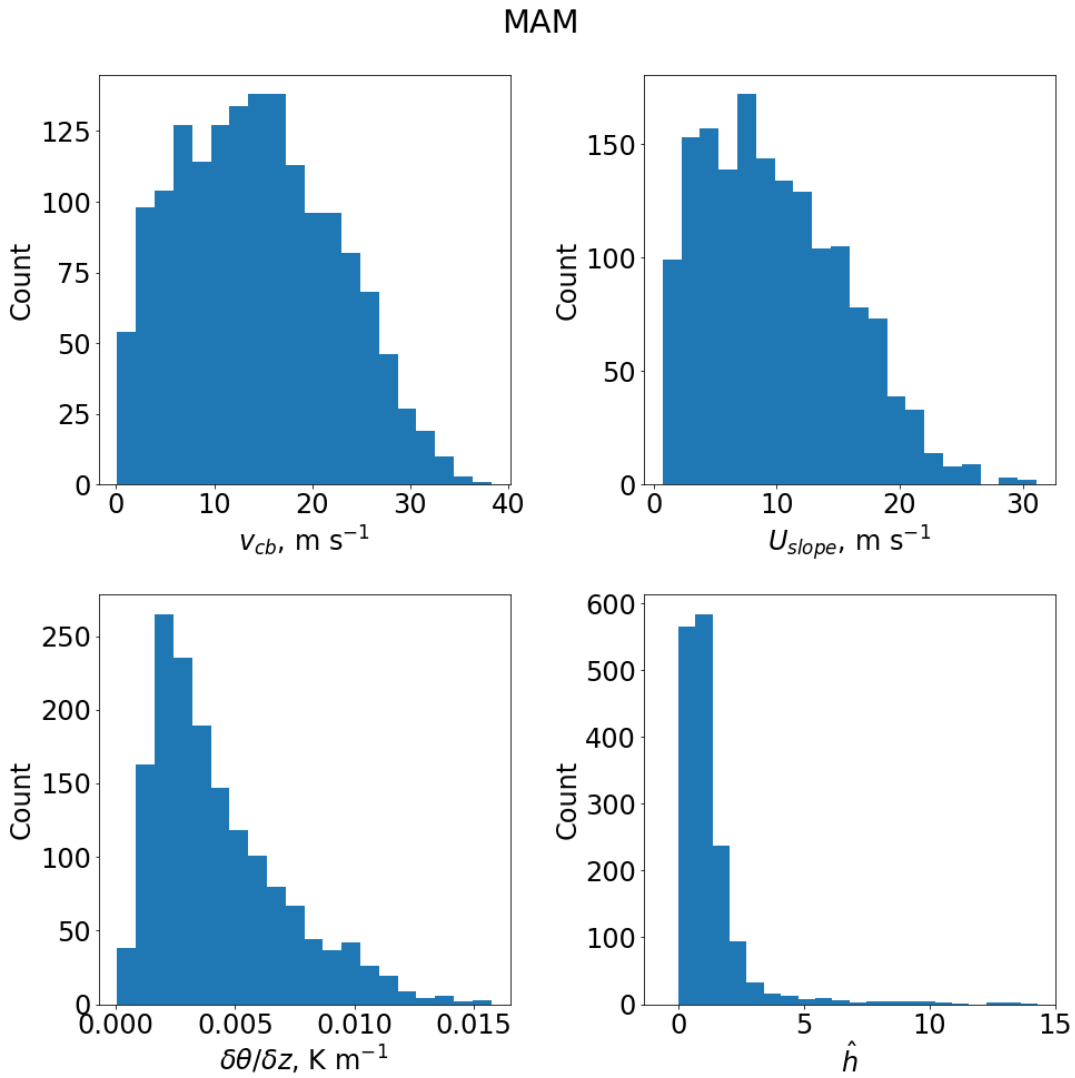

Figure 4.6: Histograms of derived CARRA 3-hourly springtime (MAM) cross-ridge velocity v_{cb} (top left), 10-m downslope wind speed U_{slope}, atmospheric stratification between 850-hPa and 900hPa layers $\delta\theta/\delta z$, and non-dimensional mountain-height $\hat{h}$ across the 11-year reanalysis period spanning 2010-2020.

wake structures resembling those seen in the UM 0.5-km simulation, but with key differences akin to those of lower resolution (1.5-km, 4.4-km) UM simulations.

4.3.2 VALIDATING DOWNSLOPE WINDSTORM CRITERIA

It is necessary to assess what ranges the aforementioned criteria take in the CARRA dataset, and how they compare against the UM case study as a reference point, as they will be used to count and select the points in time in which the CARRA dataset would be considered to have a downslope windstorm occurring. We want

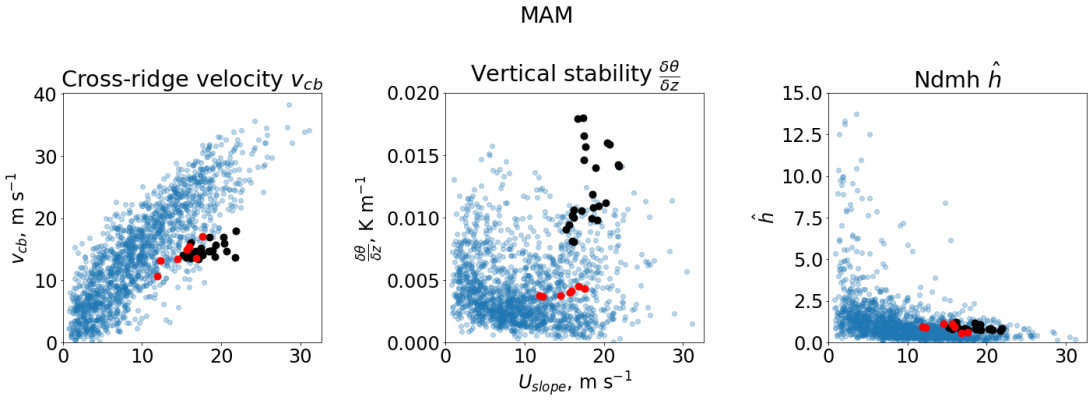

Figure 4.7: Scatter diagrams comparing derived CARRA 3-hourly springtime (MAM) v_{cb} (left), $\delta\theta/\delta z$ (middle), and $\hat{h}$ (right) against U_{slope} on lee-side slope across 2010-2020. The outputs on the case study date (19th March 2018) are highlighted for CARRA (red) and UM 0.5-km regional simulation (black).

to make sure that the conditionally sampled dataset is as clean from false-positives as possible, while not losing too many events as false-negatives. Referring back to the questions set out in Section 4.1: getting an accurate count of relevant time-points will reduce uncertainty in the abundance and duration of windstorm events in the region, removing false-positives will reduce noise in the downstream impact analysis, and by setting suitable thresholds the criteria themselves can be assessed as indicators for downslope windstorms.

DISTRIBUTION OF CRITERIA

Both v_{cb} and U_{slope} are distributed broadly across the dataset with values concentrated around 10-20 m s^{-1} and 5-10 m s^{-1} respectively, with a large proportion of data points reaching relatively high wind-speeds above 20 m s^{-1}, as shown in Figure 4.6, before tapering off approaching 40 m s^{-1} for v_{cb} and 30 m s^{-1} for U_{slope}. In contrast $\frac{\delta\theta}{\delta z}$ and $\hat{h}$ show a peak concentration near the low end of their range and a strong fall in number of points with increasing values.

A key variable used in downslope windstorm studies is wind gust at the surface; it is often easily measured using ground-based weather monitoring stations and a leading cause of damage during strong wind events (Lilly & Zipser (1972)). While some models provide a sub-grid gust diagnostic, they tend to be derived from other diagnostic fields. If we treat U_{slope} as an important factor from the perspective of a surface-bound observer and know that the higher the value of U_{slope} (or U_{10}) is the stronger the gusts are, then it makes sense to investigate the relationship between the

other three criteria and U_{slope}. This may help identify which criteria work as good indicators of downslope windstorm events.

DESCRIBING THE CRITERIA IN THE CASE STUDY CONTEXT

The application of scatter-graphs in a windstorm climatology has a diverse range of uses, including to infer the presence of shear in the vertical structure of the atmosphere during downslope windstorm events in Ólafsson & Ágústsson (2007). In Figure 4.7 scatter diagrams are used to assess the relative influence of key criteria with established importance in the theory of downslope windstorm generation (Smith (1985); Durran (1986); Jackson *et al.* (2013)) in producing downslope surface wind speeds indicative of a downslope windstorm.

The strongest correlation is seen in the v_{cb}-U_{slope} relationship, with a Pearson correlation coefficient of 0.846 in the MAM dataset. Generally higher wind speeds aloft concur with higher surface wind speeds, though there is moderate scatter with a range of 10-20 m s^{-1} for each axis, and the relationship may not be linear. The case study date data points in CARRA appear typical in the mid-range of values ranging from the 35th to the 64th percentile for v_{cb} and between the 66th and 89th percentiles for U_{slope}. The UM case study produced higher wind speeds with the highest values of U_{slope} appearing to be outliers. This could be explained due to the steeper orography in the 0.5-km grid-spacing simulation allowing for stronger gravity wave responses and downslope acceleration.

The weakest relationship is seen for $\frac{\delta\theta}{\delta z}$-$U_{slope}$ with a correlation coefficient -0.054 in MAM and generally very high scatter. While CARRA case study points are typical for the dataset, UM values produce outliers with the highest value of $\frac{\delta\theta}{\delta z}$ exceeding 0.0175 K m^{-}, which is above the highest threshold for synoptic windstorm detection (>10 K K m^{-}) used by Abatzoglou *et al.* (2020). Encouragingly, the highest values of $\hat{h}$ ($\gg 2$), which would suggest a flow regime strongly influenced by flow blocking, thus suppressing gravity wave generation above the lee-side slope (Jackson *et al.* (2013)) are confined to the lowest values of downslope wind speed.

Conversely $\hat{h}$-U_{slope} shows a roughly exponential decay with a small number of extremely high $\hat{h}$ values rapidly dropping off into a tangential approach to $y = 0$. Both CARRA and UM case study points fall within the abundant 1-2 range and are clustered close together, which is also seen in Figure 4.3,where the evolution of $\hat{h}$ in

CARRA roughly follows the curve for the UM. Both $\hat{h}$ and stratification aloft play an important role in the formation of gravity wave structures associated with downslope windstorms, especially for inversion-strength stable layers (Vosper (2004)). While neither CARRA or the UM simulation produced a discontinuity strong enough to be considered an inversion, the presence of a stable layer in the UM simulation has been studied in detail in Chapter 3. The fact that the UM $\frac{\delta\theta}{\delta z}$ values exceed the range of the CARRA MAM dataset despite being a moderate event in terms of wind speed brings into question the reliability of $\frac{\delta\theta}{\delta z}$ of being an effective indicator for our purposes.

SUMMARISING THE CRITERIA VALIDATION

In this section we have established that about one fifth of the time points in the CARRA dataset have southwesterly winds at the ridge in a 45°arc, allowing for up to 200 days per seasonal dataset, cumulative over the 2010-2020 period, to contain potential downslope windstorm candidates. We have also established that CARRA performs similarly to the UM in modelling the upstream synoptic conditions, and models downslope acceleration, a decelerated region above the wave, and a wake, but underestimates wind speeds at the ridge and on the slope slightly. A significant divergence between the models is seen in the vertical atmospheric structure at the ridge, where the UM estimates values of $\frac{\delta\theta}{\delta z}$ three times larger than CARRA. Utilising more layers in CARRA may help to refine this result. Otherwise, CARRA models the windstorm with reasonable fidelity and we can proceed with conditional sampling of the dataset for events.

4.4 CRITERIA COMPARISON

We remind ourselves of the question set out at the beginning of this chapter on how the conditional sampling criteria perform as indicators of downslope windstorms. To pursue this question the CARRA dataset is conditionally sampled with each criterion, and the time-averaged composite of the returned time-points is used to search for horizontal signatures that have been explored in Chapter 3: strong downslope acceleration, an area of strong deceleration above the slope reminiscent of wave-breaking aloft, and a distinctive wake signature.

The wake signature is particularly important, since detecting a long wake

signature that could convey perturbations in the field far downstream would help answer the other questions of what the impacts of downslope windstorms in this region are on the large-scale circulation, or if this climatological approach is providing the necessary alleviation of uncertainty encountered in Chapter 3.

4.4.1 DEFINING THE THRESHOLDS

The next step in this investigation is to conditionally sample a selection of diagnostics by the above discussed criteria individually and to search the resulting composites for downslope windstorm related signals. Considering the range of values used in similar climatologies (e.g. Ágústsson & Ólafsson (2010); Abatzoglou *et al.* (2020)), the values of the case study event on the 19th March 2018, and the need to balance those findings with the need to produce a sufficiently large sample size, the criteria thresholds are chosen to be as follows:

- $v_{cb} > 13$ m s^{-1}
- $U_{slope} > 13$ m s^{-1}
- $\frac{\delta\theta}{\delta z} > 0.004$ K m^{-}
- $0.7 < \hat{h} < 2.6$.

The wind speed thresholds are significantly lower than the typical wind speeds associated with downslope windstorms hydraulic jumps and wave breaking, which are usually greater than 20 m s^{-1}. Durran & Menchaca (2017) predicted a downslope wind speed of 26 m s^{-1} in their 3D idealised simulations of a cyclonic system interacting with an isolated ridge of 2km height. Alpers *et al.* (2009) found satellite derived observed lee-side jets with wind speeds as high as 25 m s^{-1} for at least one case of the Adriatic Bora, where the Dinaric Alps have peaks ranging between 1-2km. Lawson & Horel (2015) show in their WRF simulations of a downslope windstorm that a wind of 20 m s^{-1} is incident on the Wasatch Front (2-2.5 km height above sea-level).

However, the ridge in the Northeast Westfjords is relatively small at 0.8-1 km height above sea-level and the distributions in Figure 4.7 suggest the case study windstorm is a moderate event for the ridge. Abatzoglou *et al.* (2020) also found that for smaller ridges when v_{cb} fell below 14 m s^{-1} other indicators still suggested

the existence of downslope windstorms, and ultimately settled on a $v_{cb} > 13$ m s^{-1} threshold as well.

Additionally, the UM predicts wind speeds of 20 m s^{-1}, but this is not sustained for the whole forecast during which wave-breaking, a hydraulic jump, and distinctive wake signatures occur (Chapters 2, 3). The chosen 13 m s^{-1} represents a mid-range value of the case study event slightly below its mean v_{cb} (14.1 ± 1.9 m s^{-1}; error is 1 s.d.) and U_{slope} (15.0 ± 2.0 m s^{-1}) values, and represents the 71st percentile of U_{slope} and 45th percentile of v_{cb} in the MAM dataset. This means it is a high threshold for downslope wind speed, and the difference between the percentiles implies that v_{cb} is not necessarily a strong factor in indicating downslope windstorms at this location.

Lastly, the choice for the $\hat{h}$ range based on linear theory; it indicates that, for airflow over a long ridge oriented perpendicular to the flow, values of $\hat{h}$ between approximately 0.7 and 2.6 are associated with mountain wave-breaking (Smith (1989)), and is well known from numerical studies of mountain waves.

4.4.2 LEE-SIDE SIGNALS AFTER CONDITIONAL SAMPLING

Figures 4.8 to 4.11 show time-averaged spring-time diagnostic and derived fields over the lee of the Westfjords for each sample of reanalysis outputs sampled by the above thresholds. In this section we omit the surface-level air temperature and relative humidity composites, as the wake signal is quite weak in them. We will show them in our combined conditionally sampled composites in Section 4.5, where they feature more distinguishable wake features. After sampling based on the thresholds given in Section 4.4.1 we obtained time-averaged composites composed of 462, 877, 702 and 883 3-hourly outputs for the U_{slope}, v_{cb}, $\delta\theta/\delta z$ and $\hat{h}$ conditions, respectively. The latter three return a similar number of constituent time-points, whereas U_{slope} returns about 400 fewer time-points than the other conditions.

This implies that the three criteria generally used as indicators of downslope windstorm activity (e.g. Durran & Menchaca (2017); Abatzoglou *et al.* (2020) individually sample 3-hourly output times that include a significant number of times that do not reproduce high enough downslope winds. In this chapter we treat a high U_{slope} as a characteristic of downslope windstorms (see Section 4.3.2). This implication will become apparent in the composites.

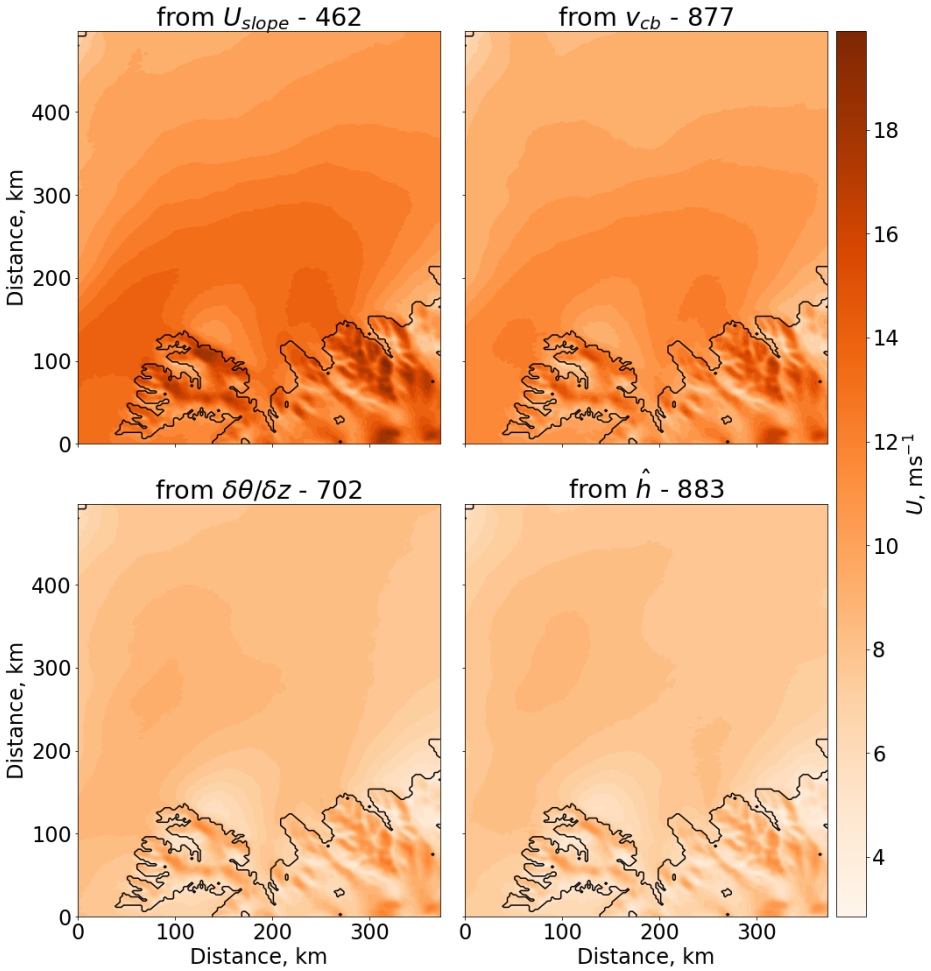

Figure 4.8: Horizontal slices of springtime CARRA 10-m horizontal wind speed composites over leeside Iceland-Greenland Sea area sampled for wind-direction and $U_{slope} > 13$ m s^{-1} (top left), $v_{cb} > 13$ m s^{-1} (top right), $\delta\theta/\delta z > 0.0004$ K m^{-} (bottom left), and $0.7 < \hat{h} < 2$ (bottom right) respectively. Horizontal axes are horizontal distance on the regular x-y grid. The number of sampled time-points used in the composite is given in the panel heading (e.g the U_{slope} composite used 462 3-hourly CARRA outputs).

WIND SPEED COMPOSITES

10-m wind speed in Figure 4.8 shows highest ambient and slope-winds for the U_{slope}- and v_{cb}-samples, though much lower wind speeds for the $\frac{\delta\theta}{\delta z}$- and $\hat{h}$-samples. We note here that this expected as those criteria are not specific to downslope windstorms, particularly $\frac{\delta\theta}{\delta z}$, but we analyse them as certain value ranges of the criteria are known to occur concurrently with downslope windstorms.

All four fields show a diffuse wake signal spanning the width of the ridge and extending 50-100 km out to sea. This may be a sign of strong hydraulic wave activity in all samples. Surface deceleration in the lee suggests vertical dispersal of momentum;

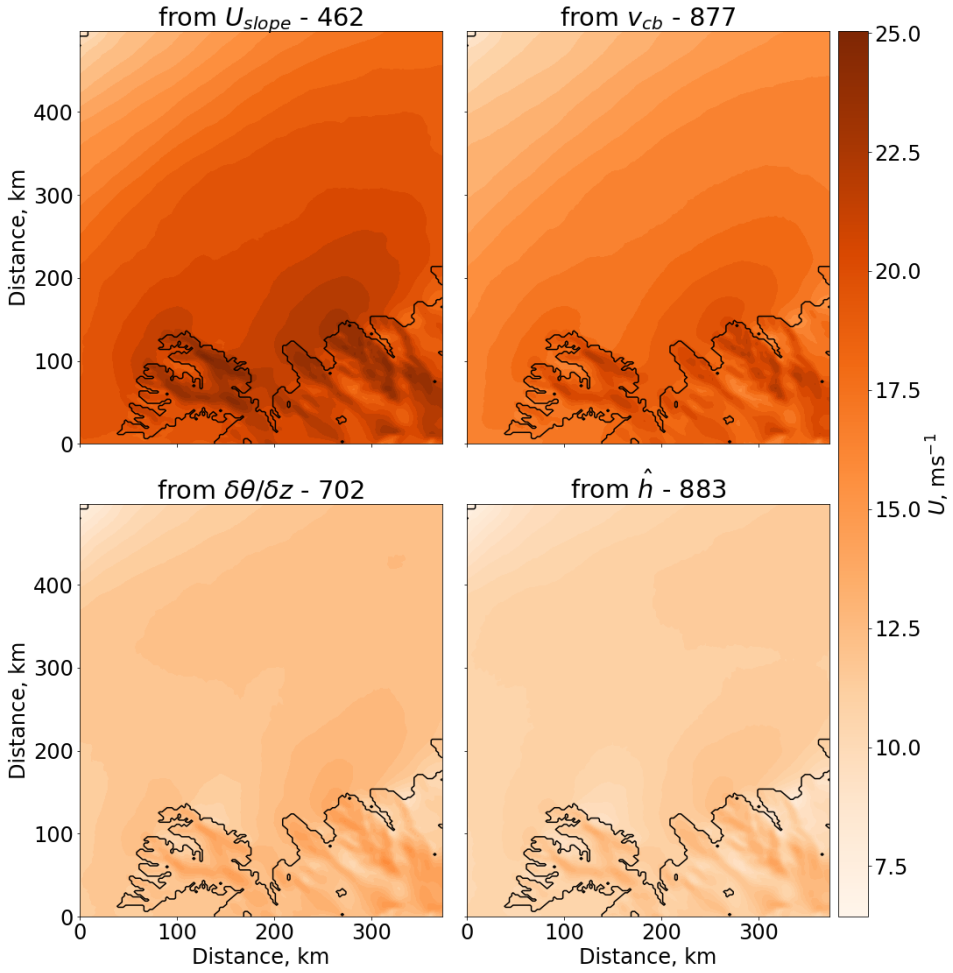

Figure 4.9: As in Figure 4.8, but for 850-hPa horizontal wind speed, U_{850hPa}.

this is accomplished by vertically propagating gravity waves, as discussed in Chapter 1. In the vertical cross-section in Chapter 3 we also see a hydraulic jump *lifting* the jet from the surface, as the flow lines recover to a level of equilibrium and lee waves are attenuated.

A second wake is noticeable to the East, potentially coming off an internal glacier; while Langjokull and Hofsjokull Glacier lie outside the frame in Figure 4.8, they are the two highest peaks in Iceland's interior directly upstream of the secondary wake signature (recall the map in Figure 4.1). Wind speed at 850-hPa in Figure 4.9 appears similar to the 10-m fields, though the wake signatures lose distinctiveness and appear to merge into the ambient flow, leaving localised areas of apparently accelerated flow flanking the lee of the ridge. One of these areas could be the signature of a jet emanating from Iceland's internal orography, echoing the secondary wake in the 10m

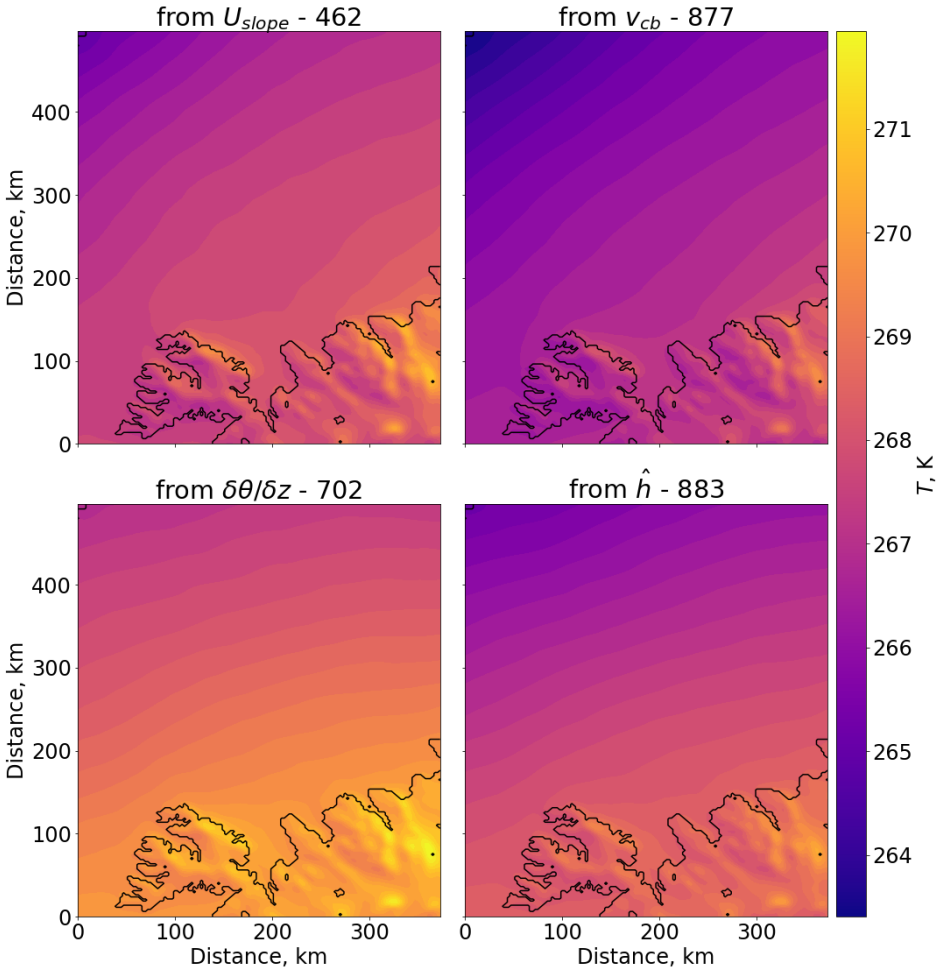

Figure 4.10: As in Figure 4.8, but for 850-hPa air temperature, T_{850hPa}.

wind field.

TEMPERATURE COMPOSITES

The 850hPa air temperature fields in Figure 4.10 show Foehn warming above the slope with temperature differences between the warming area and the surroundings being about 2-3 K, but no noticeable jets of Foehn extend from the ridge. The highest ambient temperatures are in the $\frac{\delta\theta}{\delta z}$ composite, which could suggest that instances of strong stratification may correspond with a compaction of the boundary layer.

All four samples suffer from the noise generated from the latitudinal dependence of temperature. Even temperature difference fields (subtracted from the time-averaged field that was not conditionally sampled, or raw mean field) show a very noisy environment, and show predominantly warmer averages than the raw mean field (not shown). Air temperature at 2-m also suffers from the latitudinal dependence

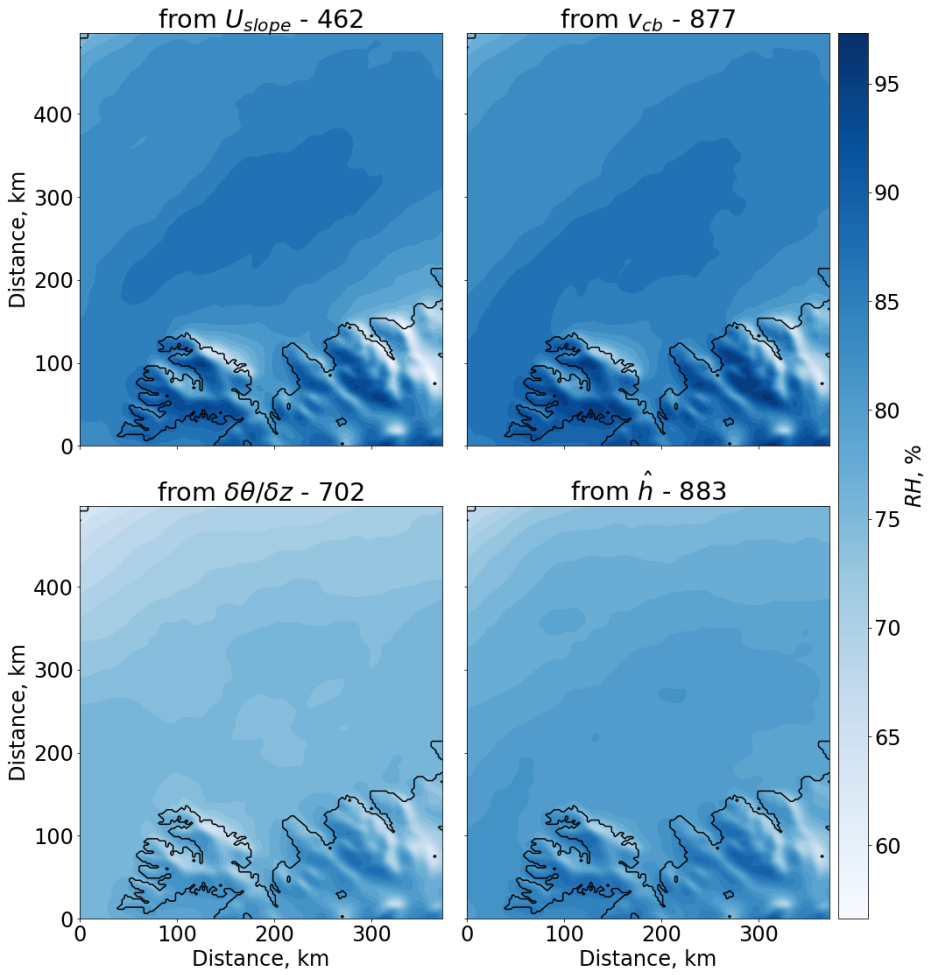

Figure 4.11: As in Figure 4.8, but for 850-hPa relative humidity, RH_{850hPa}.

as well as the surface-altitude dependence. Due to the nature of the grid in the CARRA dataset calculating and subtracting zonal means for the entire domain proved prohibitive in the available time-frame.

RELATIVE HUMIDITY COMPOSITES

The relative humidity fields in Figure 4.11 show drying at the slopes, corresponding with the air temperature fields, with differences between aloft of the slope and the ambient flow ranging between 15-25 %. Although barely perceptible, a dry wake-like signal extends 20km downstream in the wind speed sampled composites. Similar drying is seen East where the other storm signature is seen in the previous figures.

The downstream contrast, where the contrast is defined as the difference between the minimum of the wake and the adjacent ambient flow is difficult to attribute to the

wakes of the windstorm, since the peninsula as a whole may be redirecting upstream moist air around the land-mass into the Denmark Strait. This structure is absent in the $\frac{\delta\theta}{\delta z}$ and $\hat{h}$-sampled composites, and the relative drying above the slope is weaker.

We see this phenomenon in our case study in Chapter 3, where a strong westerly jet in the Denmark Strait with wind speeds exceeding 20 m s^{-1} coincides with relative humidity values reaching 100 % at 850-hPa. We remind ourselves of the synoptic meteorology in Figures 2.3 and 2.4, where we saw that a geostrophic jet formed between a low pressure center north off the east-coast of Greenland and a high pressure center south of Iceland; the cyclonic low pressure system contributed moisture over Greenland.

Instances of higher geostrophic wind speed, as is seen in the U_{slope} and v_{cb} composites, could be linked to strong cyclonic activity from a northern low pressure system bringing in moist air from the North Atlantic and the Davis Strait west of Greenland, explaining the structure seen in Figure 4.11. The synoptic situation is reminiscent of Hughes & Hall (2010)'s finding of a high pressure anomaly directing flow perpendicular into a Californian coastal mountain range, contributing to the generation of hot dry Santa Ana winds sourced from the North American interior.

In our case study we found that a high pressure system to the south of Iceland and a low pressure center to the North acted together to direct geostrophic flow at a high angle into the Westfjords. However, this synoptic situation brings in moist air from the West, in contrast to the Santa Ana winds in Southern California.

DISCUSSION OF CRITERIA SAMPLED COMPOSITES

A further climatological study may be able to develop a generalised approach to indicating downslope windstorm generation in the Westfjords by constraining the synoptic conditions needed to form it, and might address downstream impacts of the windstorms by focussing on the modulation of moisture flux in its wake.

We recall the questions set out in Section 4.1 and the suggestion made in Chapter 3 to use ensemble forecasts or reanalyses to elucidate the impact of resolved downslope windstorms further downstream than the UM 0.5-km simulation in the previous chapters could show.

Additionally, by sampling a significant number of windstorms, we hoped that the downstream impact would become more pronounced and independent of the

spatial heterogeneity of the filament-like wakes that we saw in the case study fields leading to fast attenuating mean-difference decay lines in Figure 3.15. The panels in the time-averaged conditionally sampled composites in this section show a domain about twice as large in each horizontal dimension for this purpose.

None of the criteria produce a composite wake signature that extends far enough downstream to interact with the large-scale circulation in a meaningful way. Zones of leeside deceleration in the 10-m and 850-hPa wind speed fields extend only about 100 km into the bay area, which would still be within the UM 0.5-km simulation's domain in Chapter 3, which skims, but does not reach into the flow through the Denmark Strait.

Regarding the performance of the criteria as indicators, the conditionally sampled atmospheric state fields show windstorm or mountain wave signatures for each criterion: U_{slope} and v_{cb} show the strongest downslope acceleration and the highest wake-contrasts at 850-hPa for wind speed, with differences of around 5 m s^{-1} for both U_{10} and U_{850hPa}.

All criteria also show a a sharp increase in the $\frac{\delta\theta}{\delta z}$ field at the slope suggesting a compaction of the flow lines which is a sign of gravity wave activity (not shown). All criteria produce a Foehn warming- and drying signature above the slope, with contrasts of order 1-2 K for temperature and around 20 % for relative humidity. These warming signatures are weaker than those seen for the case study in the previous chapters, illustrated in Figure 3.11, where we record cross-ridge jumps in air temperature closer to 8 K and a change in relative humidity of 60-80 %. This may be because these criteria are not sufficiently specific for downslope windstorms, and other flow conditions dilute the composites.

These cross-sections also show distinctive wakes where the dry and warmed state of the layer is maintained for at least 100 km downstream. The conditionally sampled composites show warming and drying at the slope only, and no wake in temperature or relative humidity with a contrast the same magnitude as the case study extend further than a few kilometers.

Given these findings, and the relationships seen in the scatter diagrams in Figure 4.7, where v_{cb} and $\hat{h}$ appear to show some level of correlation with U_{slope}, and $\frac{\delta\theta}{\delta z}$ does not due to very high scatter, and given the difference between $\frac{\delta\theta}{\delta z}$ case study values between CARRA and the UM, we consider U_{slope}, v_{cb}, and $\hat{h}$ as potentially suitable

indicators of the type of windstorm signatures we hope to find when combined in Section 4.5.

One expected result from combining some of the criteria is that more false-positives, or time-points that do not contain a downslope windstorm, are removed, making the resulting signal less noisy.

4.5 COMBINED CRITERIA SAMPLING

At this point of the chapter we have not seen a signal of a long wake large enough to reach into the synoptic flow in any of our composites, although there may be interaction through lateral mixing. A likely cause of this apparent non-interaction with the synoptic flow is that the time-averaged composites (Section 4.4.2) contain noise that interferes with the signal; i.e. there are too many false-positives (times when there is no windstorm) and they erase any strong emerging contrasts the atmospheric flow in the lee of the ridge would have with the ambient flow.

COMPOSITES FROM COMBINED CRITERIA

To clean up the signals discussed in Section 4.4 we combine three of the conditional sampling criteria: v_{cb}, U_{slope}, and $\hat{h}$ which have been chosen as suitable indicators above. We recall that the aim of this process is to isolate a distinct signal of a wake extending far downstream, and to find evidence of measurable downstream transport of momentum, heat, and moisture occurring in the presence of a downslope windstorm relative to a field that is not sampled for windstorm events. This study has also not investigated conserved quantities in depth, such as potential vorticity, which may show more definite flow interaction.

The time-averaged fields from the springtime dataset resulting from the combined conditional sampling are shown in Figure 4.12. The U_{10} field shows a diffuse zone of deceleration off the base of the slope extending about 100 km out to sea, echoing the U_{10} fields seen in the previous section. Close clustering of 1 m s^{-1} contours marks this time-averaged wake structure and there likely is no further downstream signal judging from the more widely spaced contours out at sea standing in a strong contrast to the wake. The strong deceleration in the lee of the ridge suggests an upward removal of momentum over the sea, suggesting significant gravity

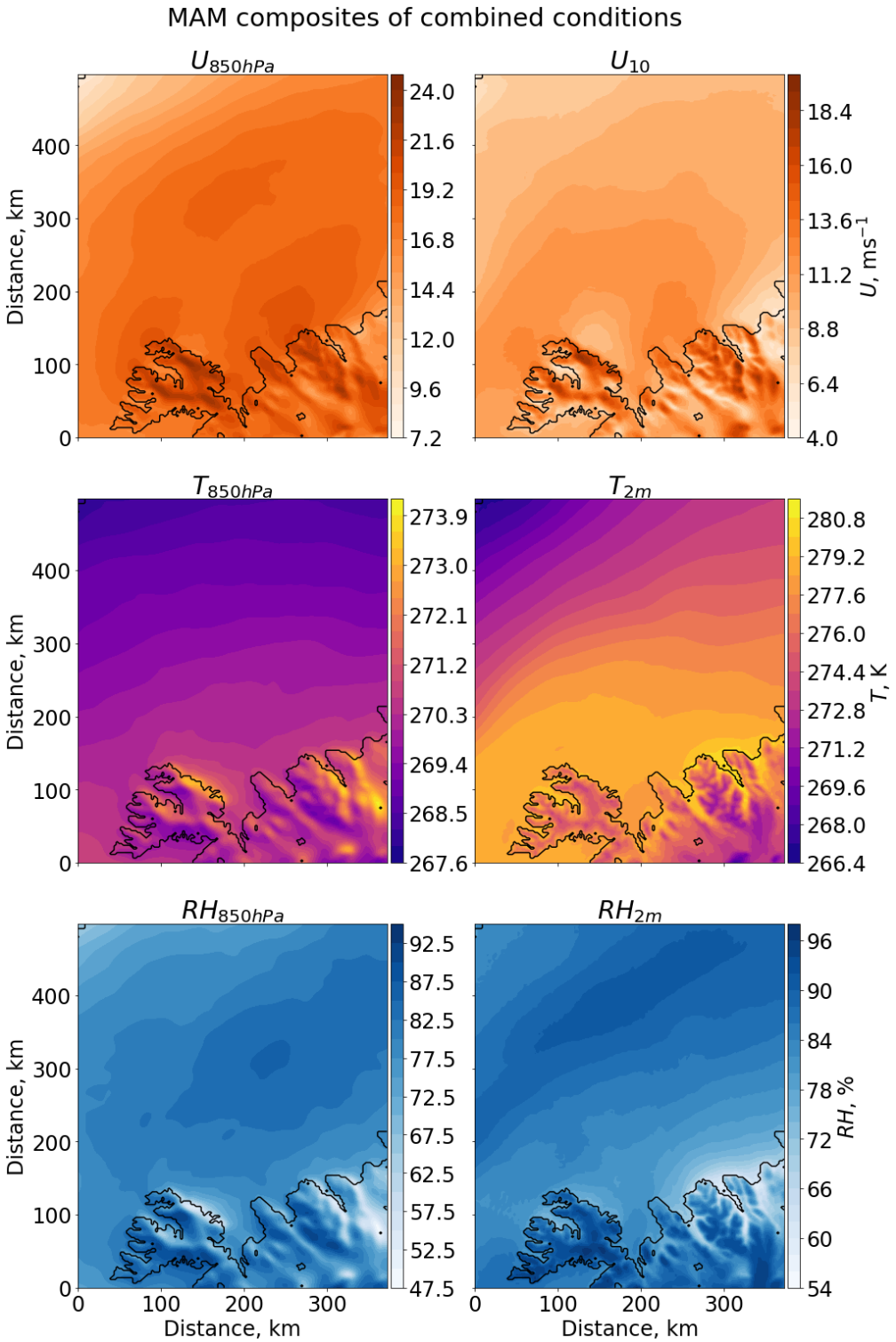

Figure 4.12: Maps of springtime CARRA horizontal wind speed (top row), air temperature (middle row) and relative humidity (bottom row) composites at 850-hPa (left column) and surface level (right column). Diagnostics are sampled by wind direction and for the unity of $U_{slope} > 13$ m s^{-1}, $v_{cb} > 13$ m s^{-1} and $0.7 < \hat{h} < 2$.

wave activity in the conditionally sampled dataset.

We see a long extension of a decelerated band extending from the ridge in the U_{850hPa} marked by two wind speed maxima shown in the flanking the band. The wind speed depression is less than 0.5 m s^{-1}, which seems very little. It is also notable that the U_{850hPa} does not show a strongly decelerated flow zone above the slope region, which is seen in the case study.

While there is warming at the slope as seen in the T_{850hPa} and T_{2m} fields in Figure 4.12, and corresponding drying in the RH fields, the Foehn effect appears confined to the area closely around the ridge and there is no evidence of Foehn jets, like those seen on the Antarctic Ice Shelf by Elvidge *et al.* (2015) being prominent in the dataset. But those types of jets are gap-jets and are highly susceptible to variations in wind direction and do not always extend down to the surface, which would make them less likely to appear in the T_{2m} fields.

DIFFERENCES IN COMBINED CRITERIA COMPOSITES

We adapt the method of using difference-fields in Chapter 3 to the climatology, where instead of subtracting the high resolution *truth* simulation from the coarse global driving model, we subtract the time-averaged composite of the directionally-sampled, but not criteria-sampled, time-points from the criteria-sampled fields. The non-conditionally sampled field represents the mean state of the atmosphere during southwesterly flow over the peninsula, and may include structures that are common to the region during times when no downslope windstorm is generated, such as a wake produced by the peninsula blocking flow, or trapped lee-waves.

The difference fields in Figure 4.13 show the relative mean impacts downslope windstorm events have on the mean flow. The wind speed and air temperature composites show zero negative difference. Positive differences in U_{850hPa} reach 10 m s^{-1} at the ridge and up to 5 m s^{-1} in the lee, but the wake contrast seen in the mean composite field in Figure 4.12 is equally small. The contours representing the original sampled U_{850hPa} field also do not highlight any particular areas of notable difference.

Differences in T_{850hPa} reach 6 K above the slope, but fall to 2-3 K downstream, and differences in T_{2m} also peak at the slope with 3-4 K, but fall to 1-2 K downstream, though there is a structure of marginally warmer air extending from the ridge. The isotherm contours in the T_{2m} roughly follow the U_{10} contours, in that they are

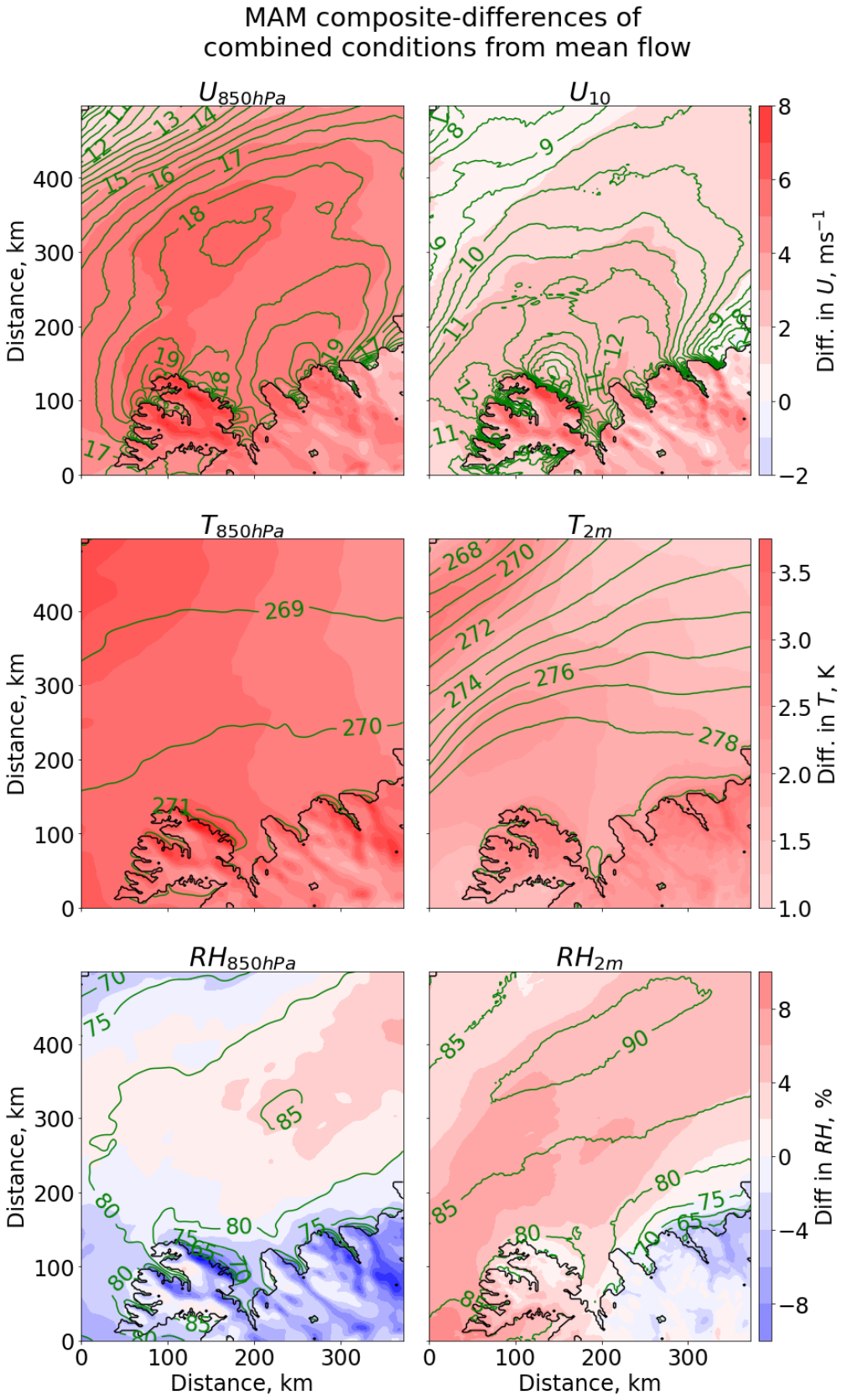

Figure 4.13: Maps of springtime CARRA horizontal wind speed (top row), air temperature (middle row) and relative humidity (bottom row) difference composites at 850-hPa (left column) and surface level (right column). Diagnostics are sampled by wind direction and for the unity of $U_{slope} > 13$ m s^{-1}, $v_{cb} > 13$ m s^{-1} and $0.7 < \hat{h} < 2$. Differences are calculated by subtracting the directionally sampled mean from the criteria- and directionally-sampled 3-hourly outputs, and then taking the average. Green contours represent the composite fields shown in Figure 4.12 and are included to highlight areas of notable overlap; contour units for the fields are the same as for the differences.

relatively compact in the Denmark Strait and then spread out as the Strait opens up to the Iceland Sea. This is reminiscent of geostrophic wind accelerating along isobars being compacted by a bottleneck in the geography and then decelerating as momentum is distributed as the isobars spread out. If the wake structure interacts with these contours it could be considered an interaction with the large-scale circulation.

The positive differences in the T_{2m} field correspond roughly with positive differences in RH_{2m} of up to 10 % downstream and in the Denmark Strait. While we cannot say for certain, both positive T_{2m} and U_{10} differences would lead to more surface evaporation and surface heat flux also scales with U_{10}, so both increase surface heat fluxes, which can lead to more moisture being induced into the atmosphere.

The slope and immediate lee of the ridge show a different process: relative to the positive difference in the surrounding sea and upstream orography, the difference at the slope is near zero, and corresponds with the drying seen in the contours representing the non-difference conditionally sampled RH_{2m} field. For RH_{850hPa} the slope-side drying is strong enough to produce negative differences of up to 20 %.

These anomalies do not extend far at 10-20 km from the slope, but highlight a significant amount of moisture and latent heat transport taking place at the top of the atmospheric boundary layer. This may indicate stronger impacts further aloft, since downslope windstorms are generated by vertically propagating gravity waves. These waves transport momentum, but not mass, under normal conditions in which they do not break. Heat and moisture are transported through turbulence (as well as advection) so they require vertically propagating gravity waves to break, which is what we see at the boundary layer.

The overall positive differences throughout the domain show that southwesterly windstorms typically coincide with conditions that are warmer and moister than normal. This would be expected, as southerly synoptic flow will carry warmer and moister air from lower latitudes. The strong relative drying seen in Figure 4.12 would suggest that the windstorms could suppress precipitation on the fringes of weather systems passing through the Denmark Strait, where relatively dry air mixes with the relatively moist air in the synoptic flow and lowers RH.

In this section we have combined three criteria for our conditional sampling

and explored the resulting time-averaged composites. We found that generally the strongest differences occur at the slope (e.g 4 K for 850-hPa temperature differences and −20 % for 850-hPa relative humidity differences) and then attenuate to background-level difference within 100 km downstream, which is in agreement with our results from Chapter 3.

We found that the humidity and temperature fields over the sea are dominated by near homogeneous positive differences, which may be a result of southerly synoptic flow bring in warmer and moister air from lower latitudes. It was suggested that the drier wakes of downslope windstorms would mix with the large scale flow at its edges and lower RH. This may have implications for precipitation occurring offshore of Iceland.

4.6 DOWNSLOPE WINDSTORM EVENTS

In this section we will revisit one of the questions set out in the introduction to this chapter: What is the climatological context of the case study presented in Chapter 3? This allows us to subsequently select the most prolonged events in the combined wintertime and springtime dataset, as a means of constraining our selection to events that likely had the greatest impacts on the surrounding meteorology at the time. This provides an additional approach to answering the question of what the downstream impacts of downslope windstorms at this location are, complementing our time-averaged composite approach in the earlier sections. Finally, this approach may also highlight a cause of noise in the composites, which will be discussed.

FINDING AND COUNTING WINDSTORMS IN THE DATASET

To identify the events we conditionally sampled the combined winter- and springtime dataset using the criteria discussed earlier in this chapter, which gave a distribution of time-points. These time-points were grouped by adjacency, and groupings 9 hours or fewer apart were counted as the same event. Lone time-points were omitted, limiting the estimated duration of an event to a minimum of 6 hours, as described in Section 4.2.

Figure 4.14 shows the distribution of the counted events across the 11 year climatology. Most events have a duration between 6 and 12 hours. In extreme value

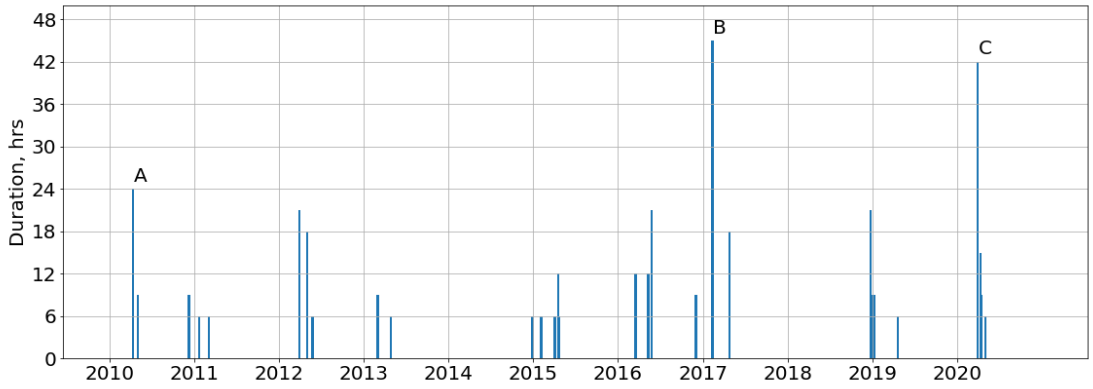

Figure 4.14: Timeline of conditionally sampled events over the whole 2010-2020 wintertime and springtime climatology using CARRA reanalysis. Conditions applied are wind direction and unity of $U_{slope} > 13$ m s^{-1}, $v_{cb} > 13$ m s^{-1} and $0.7 < \hat{h} < 2$. Y-axis represents the estimated event duration in hours, which are multiples of three of the number of consecutively counted output times. The three longest duration events are labelled A, B and C. A total of 31 events of two or more consecutive output times passed the criteria, with 21 events occurring in springtime (MAM).

theory an extreme event is usually above the 90th to 99th percentile of the dataset, depending on the dataset size. We can define a *prolonged* event by an extreme value threshold. The 90th percentile of event duration in our sample is 21 hours.

There are three events above this threshold, which are designated A, B, and C (Figure 4.14). In alphabetical order, their start dates (and estimated duration) are 12th April 2010 (24 hours), 11th February 2017 (45 hours), and 29th March 2020 (42 hours), and their respective criteria values, and how they compare to the UM and CARRA representation of the case study event, are shown in Table 4.1.

The case study event did not pass the sampling condition, though if the wind speed thresholds are lowered to 12 m s^{-1}, then it would show as a 6 hour event. The UM representation of the case study event passes the criteria returning a 24 hour duration (the UM simulation was a 24 hour forecast, which limits the measurable duration to that time period).

The absence of the case study event implies that there is a number of false negatives contributing to the uncertainty in the composite fields, and further investigation of the criteria thresholds would be appropriate. A study that tests a range of thresholds could define the criteria for downslope windstorm actiy more precisely.

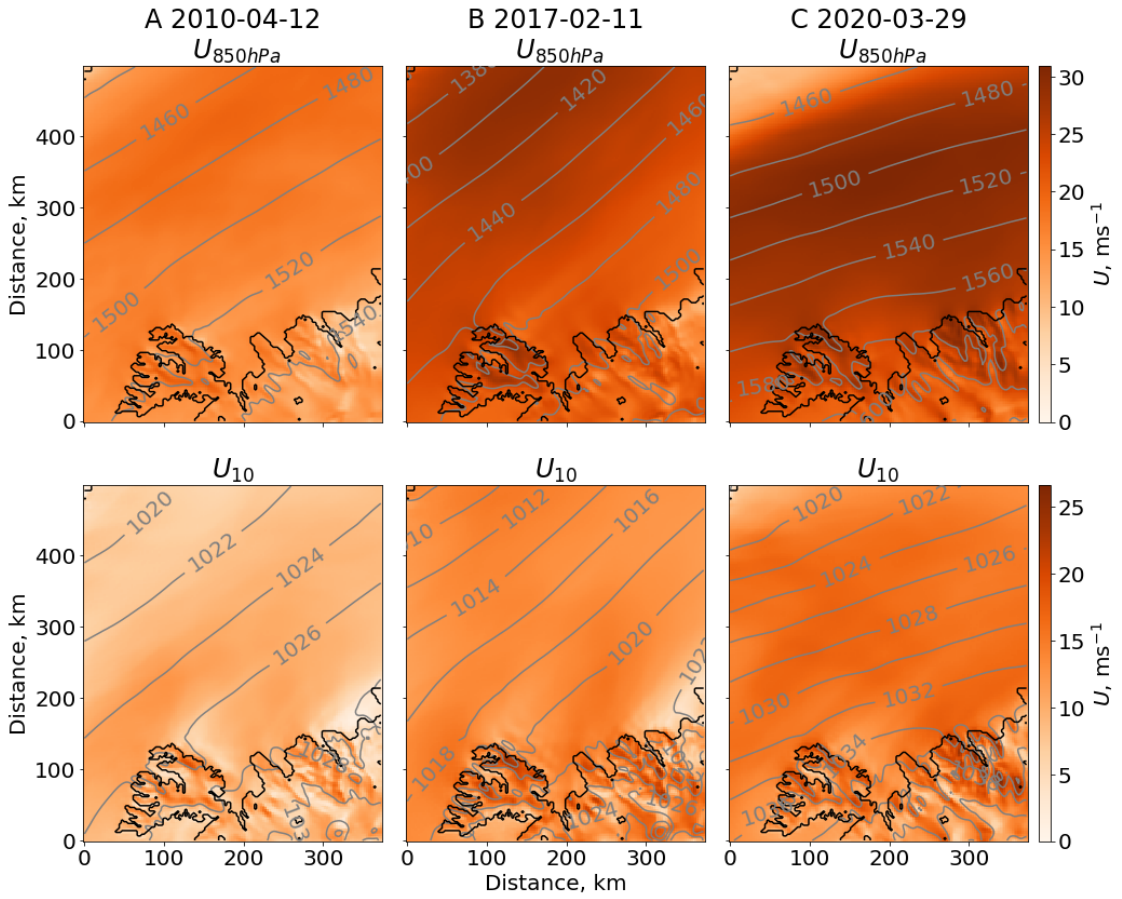

Figure 4.15: Horizontal wind speed maps at 850-hPa (top row) and 10-m (bottom) for events A (left column), B (middle), and C (right), defined in Figure 4.14, averaged across event duration. Contours in 850-hPa panels show geopotential height in 20 m steps and contours in 10-m fields show mean-sea level pressure in 2 hPa steps. Horizontal axes are horizontal distance in kilometers.

COMPARING THREE EXAMPLE WINDSTORM EVENTS

Figure 4.15 shows the time-averaged wind speed fields and 4.16 shows the corresponding air temperature and relative humidity fields for events A, B, and C. Event A looks most similar to the case study event, with moderate wind speeds not exceeding 20 m s^{-1}, and a surface wake being deflected and constricted along mean sea-level pressure contours, which was seen in the U_{10} fields in Chapter 3. The ambient wind direction in A is almost perpendicular to the ridge, and similarly for event B. Events B and C show higher wind speeds than A, showing a large jet at 850-hPa in the Denmark Strait reaching 30 m s^{-1}, and show ambient U_{10} values 5-10 m s^{-1} than event A. Events B and C also show a small wave pattern and a larger wake structure extending at least 100 km downstream at both 10-m and 850-hPa.

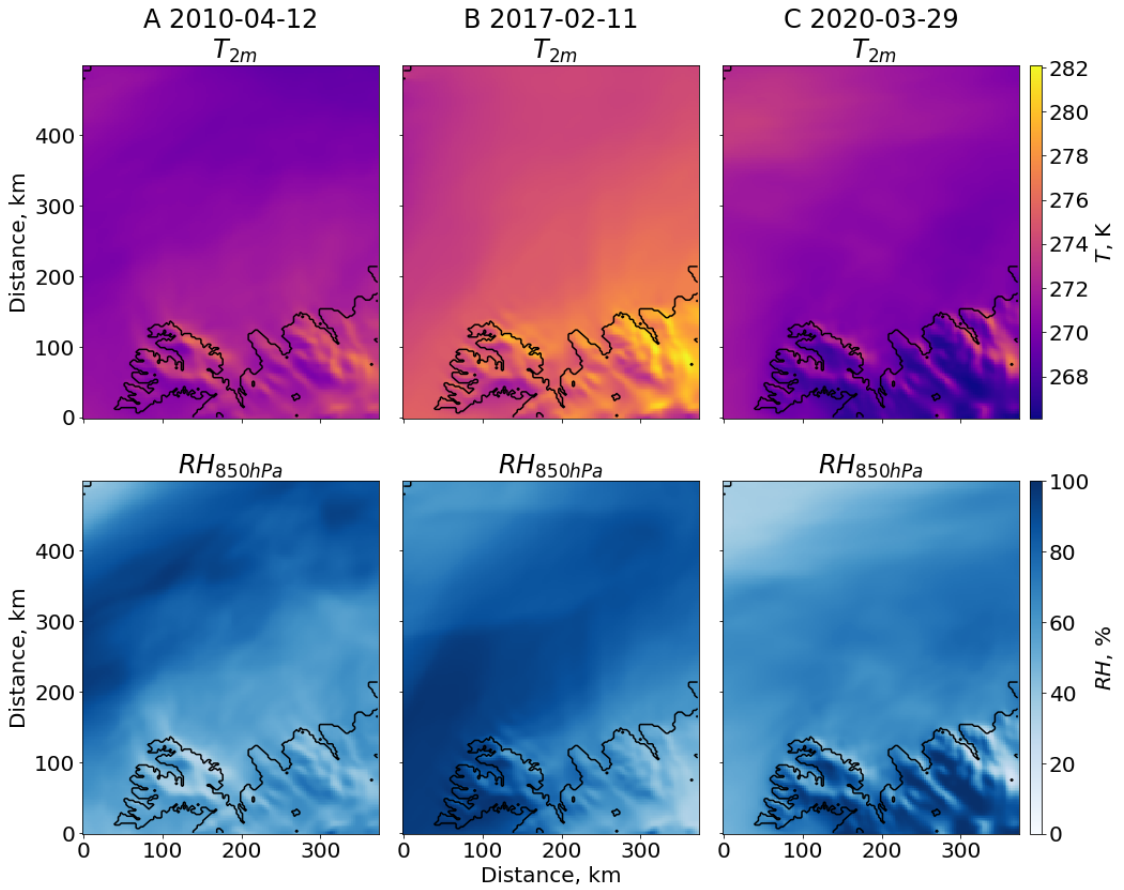

Figure 4.16: Air temperature at 850-hPa (top row) and relative humidity (bottom) for events A (left column), B (middle), and C (right), defined in Figure 4.14, averaged across event duration. Horizontal axes are horizontal distance in kilometers.

The wakes of B and C affect the geopotential contours at 850-hPa: if the wind in the Denmark Strait is geostrophic, then the wakes producing dent-like perturbations 100-200 km downstream and adjacent to the wake could be considered influencing the large-scale circulation. This perturbation does not seem to continue far downstream, and the geopotential contours recover to their original trajectory about 100-200 km downstream of the ridge.

Event B coincides with the warmest atmosphere between the events, with typical temperatures in the composite 4-6 K higher than for events A and C. It also seems to produce the largest lee-side warming with temperatures at the slope about 5 K higher than the adjacent flow, compared to warming contrasts closer to 2-4 K for A and C. Events A and B both produce noticeable patches of ambient warmer air that extend downstream from the ridge and mix into the surrounding atmosphere. All three events show drying in the lee, with event A showing the lowest relative humidity

Event	Duration	mean v_{cb}	mean U_{slope}	mean $\delta\theta/\delta z$	mean $\hat{h}$
A	24	19.4 ± 1.5	16.5 ± 1.6	0.009 ± 0.001	1.18 ± 0.25
B	45	27.5 ± 5.0	21.4 ± 4.9	0.012 ± 0.003	1.00 ± 0.25
C	42	27.5 ± 3.2	17.5 ± 3.4	0.007 ± 0.002	1.07 ± 0.18
CS/CARRA	-	14.1 ± 1.9	15.0 ± 2.0	0.0040 ± 0.0003	0.90 ± 0.22
CS/UM	-	15.4 ± 1.3	18.0 ± 2.0	0.012 ± 0.003	0.87 ± 0.13

Table 4.1: Time-averaged criteria values for three selected events given in Figure 4.14, and their respective standard-deviations in time. The duration is an estimate in hours based on the number of consecutive output times that fulfilled the sampling conditions. The estimated start dates and times for events A, B, and C are 2010-04-12T15, 2017-02-11T09, and 2020-03-29T00 respectively. The corresponding IGP case study (CS) values are given for both CARRA and UM outputs. Since the case study event (2018-03-19) did not pass the sampling conditions, the duration is omitted. U_{slope} and v_{cb} are given in m s^{-1}, $\delta\theta/\delta z$ in K m^{-1}, and $\hat{h}$ is dimensionless and evaluated for a mountain height $h = 1000$ m.

values at the slope approaching 0 %, while event B shows overall higher relative humidity in the region often exceeding 80 %.

The mean values of the criteria used for the conditional sampling of the dataset are given in Table 4.1, which reinforce the observation that event B is the strongest event, and event A is the weakest of the three. Considering the one standard deviation errors, we find that only v_{cb} and U_{slope} are significantly different between the events, while they show general agreement for $\frac{\delta\theta}{\delta z}$ and $\hat{h}$. Recalling the broad wind speed distributions in the Figure 4.6 histograms compared the sharply falling distributions of the latter two criteria, that is not unexpected: the identified downslope windstorms in Figure 4.14 can assume a large range of wind speeds with near even probability, while they are much less likely to have extreme atmospheric conditions described by $\frac{\delta\theta}{\delta z}$ and $\hat{h}$.

COMPARING EXAMPLE EVENTS TO CASE STUDY

One exception we are aware of is the CARRA representation of the case study event shows significantly lower stratification aloft with little variation in the day, while the UM representation is akin event B. It may be that the UM-simulated results for $\frac{\delta\theta}{\delta z}$ would be higher for events A, B, and C.

In Chapter 3 we saw wave patterns, and filaments of air slower, warmer, drier, or less stratified than the ambient atmosphere extending for over 100 km from the base of the mountains. We also recall the decay-curves of the mean difference between the UM global driving model and the 0.5-km simulation, and note that the

mean differences generally attenuated to the zero-difference line within 40-100 km (Figure 3.15). This was because the lee-waves and wake-filaments were spatially constrained and followed unique paths, i.e. they were narrow and not diffuse. Our time-averaged composites of conditionally sampled windstorm events do not take the spatial heterogeneity of wakes into account, and the lack of a long wake signal means what it shows: there is limited impact downstream on scales of hundreds of kilometers on a climatological time scale from small downslope windstorms such as the one on the slopes of Drangajokull Glacier in the Westfjords.

The downslope windstorm in Chapter 3 and the example events extracted from the CARRA dataset seen in Figures 4.15 and 4.16 will have a real impact on the regional weather on the day, and therefore improving the representation of small-scale downslope windstorms in NWP models is still important.

One of the lead questions of this chapter is if the uncertainties discussed in the previous chapter, such as synoptic noise and spatial heterogeneity, can be addressed by a high-resolution atmospheric reanalysis product, such as CARRA. Not only does spatial heterogeneity in the lee of the ridge continue to be a source of uncertainty, but if the reanalysis systematically underestimates downslope windstorm strength, as it did with the case study event to the point it did not meet the sampling conditions, it may not be sufficient to address the uncertainties in the contribution of small downslope windstorms to the the large-scale circulation on climatological time-scales.

A key message of Chapter 3 was that if downslope windstorms are not resolved in operational global driving models and climate models with horizontal grid-spacings of 17 km and larger, then there could be a significant impact on climate forecasts. With the present uncertainty this is difficult to determine.

4.7 CONCLUSIONS

In this chapter we performed a winter- and springtime climatological investigation of southwesterly downslope windstorms in the Westfjords for the period spanning 2010-2020 by analysing the novel high-resolution CARRA dataset.

We found that given a set of criteria employed in other climatologies (e.g. Abatzoglou *et al.* (2020)) the number of identified windstorms is 31, with the most

typical duration being 6 hours. However, given that the reanalysis's representation of the case study event analysed in the UM simulation in Chapter 3 did not fulfill the sampling conditions we set, there may be significantly more events that escaped identification.

Following on from the above, the criteria used (v_{cb}, U_{slope}, $\frac{\delta\theta}{\delta z}$ and $\hat{h}$) indicate the occurrence of a downslope windstorm with mixed results. Since only few events would record strong static stabilities at the boundary layer top ($\frac{\delta\theta}{\delta z}$), we note its strongly skewed distribution in the dataset, and the disagreement between the UM and CARRA, $\frac{\delta\theta}{\delta z}$ is a weak indicator of downslope windstorm activity in the CARRA dataset.

Conversely, due to the broad distribution of v_{cb} and since its threshold had to be set as low as 13 m s^{-1} (and lower still to capture the case study event), to study a significant sample of strong wind events, it may also be weak on its own. Using a combination of v_{cb}, U_{slope} and $\hat{h}$ produced time-averaged composites of conditionally sampled data with stronger windstorm signals than the composites sampled by each criterion individually achieved.

Addressing the question of what the downstream impacts of downslope windstorms on the synoptic flow are, the composites showed strong wake signatures in the lee of the ridge, although notable differences compared to the ambient flow or structures dissipated within about 100 km from the coastline. On average there is significant drying in the lee, and mixing of air at the boundaries of larger scale flow systems, such as the accelerated flow through the Denmark Strait, could have a potential impact on precipitation, convection, and advection downstream.

A limitation of the study with respect to the downstream impact question are that conserved quantities, for example potential vorticity, were not explored, and the scope of the analysis focussed on the atmospheric boundary layer (ABL); a more in-depth analysis could explore the lee-side vertical structure of the atmosphere to ascertain if momentum, heat, moisture, and vorticity are effectively transported and dissipated aloft interacting with the large-scale circulation in a meaningful way, or if a shear layer, such as the one seen by Ólafsson & Ágústsson (2007), traps some of the quantities within the ABL.

We finally address the question if the uncertainties highlighted in the boundary layer turbulence sensitivity in Chapter 3 have been mitigated by the climatology,

specifically by using a high-resolution reanalysis. Due to the limited scope of this study, this is uncertain. While CARRA reproduced the horizontal downslope acceleration and wake structures reasonably well compared to the regional UM simulation, it has underestimated wind speed, lee-side warming, and stratification aloft.

We discussed in Chapter 3 that key contributors to the resolution-sensitivity in the UM reproduction of our windstorm are the wave-resolving dynamics of higher resolutions and the underestimation in topographical slope gradients in the coarser resolutions (e.g. Oltmanns *et al.* (2015); Moore & Imrit (2022)).

If these negative biases are systematic a number of events would escape detection using our method, and a more sophisticated method, such as the statistical techniques used by Shestakova *et al.* (2020), would need to be employed, or we could evaluate the CARRA dataset against long-term observations (e.g ground-based measurements and profiles) to determine the magnitude of a potential systematic bias and adjust the criteria thresholds accordingly.

5

CONCLUSIONS

In this thesis we have investigated how a downslope windstorm in the Westfjords in northwestern Iceland influences the lee-side atmosphere. With a focus on the atmospheric boundary layer we evaluated kilometer-scale and sub-kilometer-scale numerical weather prediction (NWP) models against rare in-situ aircraft observations, used the evaluated simulations for a case study of a strong wind event, and sought to establish the case study's position in a climatological context using a sub-kilometer-scale reanalysis product. During this work we tested the sensitivity of the reproduction of downslope windstorms to resolution and boundary layer turbulence.

5.1 MODEL EVALUATION

We evaluated the Met Office Unified Model (UM) against novel in-situ aircraft observations from the Iceland-Greenland Seas Project (IGP) for two regional 24-hour forecasts on the 11th March 2018 (Case 1) and 19th March 2018 (Case 2) over coastal western Iceland. Two key geographical features in that area are the mountainous Snæsfellsnes and Westfjords peninsulas, and it was the lee-side orographic flow of these peninsulas that was probed in the IGP flights. To compliment the aircraft observations, radiosonde and ground-based observations were also used. Three

regional simulations were run for each case, using 4.4-km, 1.5-km, and 0.5-km horizontal grid-spacings.

The model evaluation addressed the following aims: to introduce the meteorology of the case studies, to evaluate the model for the state variables and existing parametrised and derived flux variables using available in-situ observations, and to establish the 0.5-km simulation as a suitable control simulation for subsequent sensitivity tests.

The regional model simulations reproduced a downslope windstorm with a hydraulic jump in Case 2. This strong wind event provided the motivation for the case study and climatology chapters. As a result, the model was not only evaluated for its general performance, but also for its representation of the downslope windstorm and hydraulic jump.

We found a temperature bias in the lower atmospheric boundary layer (ABL) below 500 m altitude with a median potential temperature offset of (-1.15 ± 0.51) K in the 0.5-km simulation, which meant that the model underestimated potential temperature in the lower ABL. This bias was consistently present in all regional simulations in both cases, and comparing the global driving model (with roughly 17 km grid-spacing) to ground-based observations revealed that this bias in the regional atmosphere simulations was sourced at the lateral boundary conditions. A systematic bias like this near the surface can affect the surface energy budget and influence the modelling of air-sea exchange processes. Conversely, the temperature bias may be caused by surface fluxes, and a combination of both effects is not unlikely. Further investigation of simulations with a long-tailed ABL parametrisation may clarify the physical source of the bias.

The model struggled to reproduce an observed inversion above 2 km altitude in Case 2, instead showing a stable layer that was weaker than the observed temperature gradient and at a lower altitude. The Case 2 1.5-km simulation (used instead of 0.5-km here, for which its domain did not encompass the radiosonde location) captured the upstream atmospheric conditions reasonably well with Froude number values varying between 0.76 and 1.14. These values were consistently lower than observed Froude number values (1.07-1.61), however both value ranges imply non-linear flow and do not suggest significant regime change (Smith (1989)). There is also significant uncertainty in the calculation of the observed Froude numbers, as they were sampled

from radiosonde data from Keflavik, which is on land. Sub-grid momentum and heat flux diagnostics in the ABL were underestimated and negligible above the mountains. It was argued the model under-represented unresolved fluxes, but also that more turbulent flux is resolved at increasing resolution.

Model performance was spatially heterogeneous, with some of the largest mean and root mean square (RMS) biases recorded above the mountain ridge and in the immediate lee, particularly for the 4.4-km simulation. Overall, the 0.5-km simulation performed consistently better than the other resolutions in capturing the orographic flow above and in the lee of the mountains, and RMS bias values in downstream flight legs showed hat the improvement from a higher resolution is maintained further downstream in the wake, even if the effect is lessened. It was argued that the 0.5-km resolution resolves flow structures in the 1-10 km scale, possibly leading to improved performance. We concluded that the 0.5-km simulation reproduced a downslope windstorm and hydraulic jump seen in Case 2 with reasonable fidelity, and could be used as a truth simulation in the subsequent resolution- and boundary layer turbulence-sensitivity analysis.

5.2 WINDSTORM CASE STUDY

We conducted a case study analysis of a downslope windstorm, which took place on the slopes of Drangajokull Glacier in the Westfjords on the 19th March 2018. The regional atmosphere simulations captured strong downslope winds (of 20 m s^{-1}), a hydraulic jump, and a wave-breaking region aloft, as evidenced by zero flow speed and reversal in the isentropes. The gravity wave was likely induced by a strong stable layer at crest height undergoing a transition to supercritical flow on the slopes. The presence of wave-breaking may have contributed to the downslope acceleration. The windstorm in the 0.5-km simulation was strongest during a period of relatively consistent upstream conditions where model non-dimensional mountain height values remained around 0.8, which are ideal conditions for downslope windstorm generation (Jackson *et al.* (2013)).

The case study analysis aimed to address the following questions: what is the effect of resolution on model reproduction of the downslope windstorm, does the windstorm have measurable effect on the large-scale flow, and how sensitive is the

windstorm's lee-side impact to changes in sub-grid-scale processes?

We showed a strong sensitivity to resolution in the reproduction of the windstorm features. Resolutions lower than 0.5-km produced a weaker windstorm and a weaker hydraulic jump with fewer resolved features, such as surface jets and lee-wave patterns. The global driving model (with 17 km grid-spacing) did not reproduce a windstorm. This sensitivity was attributed to the poorer wave-resolving dynamics of coarse resolutions (compared to 0.5-km) and that coarse resolutions smooth the orography more, and therefore do not reproduce the steep slopes necessary for a strong wave response. This argument was also made by Oltmanns *et al.* (2015), who tested the resolution sensitivity of downslope windstorms in southeast Greenland in the WRF model.

Inter-resolution (i.e. 0.5-km−4.4-km and 0.5-km−GLM) differences in the wind, temperature, and relative humidity fields were strongest within 20 km of the slope. Some comparisons showed measurable downstream differences at a distance of over 100 km from the ridge, but most attenuated to the mean difference in the domain. Differences at 850-hPa were generally more pronounced than at the surface-level.

To constrain the uncertainty in the windstorm's downstream impacts, we replaced the default boundary layer turbulence scheme with one employing a long-tail stability function that yields comparatively stronger turbulent mixing in the ABL at a given atmospheric stability. We found that the 0.5-km simulation employing the long-tail function produced a weaker downslope windstorm and hydraulic wave at a given time than the 0.5-km control simulation. The differences between the the control and long-tailed 0.5-km simulations and the control 0.5-km and 4.4-km simulations were strikingly similar. This showcased a strong sensitivity of downslope windstorm reproduction in the UM to changes to the boundary layer turbulence parametrisation that is proportionate with the sensitivity to resolution and model dynamics. This implies significant uncertainty in the downstream impacts of a resolved downslope windstorm on the boundary flow. Other sources of uncertainty that were identified were that the lee-side atmospheric state field were highly heterogeneous, so it was difficult to determine where the wake interacted with which part of the flow.

We concluded that due to the small number of available events and simulations, and due to the limitation of the 0.5-km domain size and positioning, the influence of the windstorm's wake on the large scale flow could not be determined at this point.

It was suggested that an ensemble forecast analysis or a climatology using a wave-resolving reanalysis could account for the turbulence sensitivity discussed.

5.3 WINDSTORM CLIMATOLOGY

We conducted an 11-year winter- and springtime climatology of downslope windstorms on the northeastern slopes of the Westfjords using the state-of-the-art Copernicus Arctic Reanalysis (CARRA) product. With this climatology we addressed the following questions: what is the climatological context of the case study event, how useful are available diagnostic tool for indicating a strong wind event, what are the downstream impacts of downslope windstorms in the Westfjords, and can a climatology using a high-resolution reanalysis mitigate the uncertainties from the boundary layer turbulence sensitivity, spatial heterogeneity, and synoptic influence found during the case study?

A set of diagnostic criteria were used as indicators of downslope windstorm activity (e.g. Abatzoglou *et al.* (2020)) to identify strong wind events at the mountain ridge. By comparing both UM and CARRA derived values of these diagnostic criteria for the case study event on the 19th March 2018, we found that the case study event represents a moderate event in the climatological context of the area. The criteria were: the 10-m wind speed at the slope (U_{slope}), the cross-barrier wind speed component normal to the ridge (v_{cb}), the static stability at boundary layer top ($\delta\theta/\delta z$), and the non-dimensional mountain height ($\hat{h}$).

Time-averaged composites of the conditionally sampled events were used to investigate the downstream impacts of downslope windstorms on the large-scale flow through the Denmark Strait and the Iceland Sea. The composites showed strong wake signatures in the lee of the ridge. Clear differences compared to ambient flow dissipated within about 100 km from the coastline, which may imply that there is influence on the large scale flow downstream, since energy and mass must be conserved. The dissipation of momentum, heat and moisture would change the state of the field downstream. At this stage we are not able to quantify this influence, or comment on its significance. It was however suggested in Chapter 3 that changes in precipitation over the Iceland Sea in the presence of upwind windstorms could be quantified in future work.

The composites also revealed that U_{slope}, v_{cb} and $\hat{h}$ were reasonably effective indicators of downslope wind activity, while $\delta\theta/\delta z$ was found to be a weak indicator of downslope windstorm activity in the CARRA dataset. Combining the sampling conditions for U_{slope}, v_{cb} and $\hat{h}$, 31 independent events were identified in the dataset with a duration of at least 6 hours. However the CARRA representation of the case study windstorm discussed in Section 5.2 did not fulfill the diagnostic thresholds set for the sampling, implying that many moderate strong wind events were not identified, and downslope windstorms are more common than the 31 identified events suggest. Instead the identified sample represented the strongest events captured in the dataset.

The three most prolonged strong wind events, selected from the sample, highlighted a strong heterogeneity in the lee-side atmospheric state fields between the events. Nonetheless, the overall positive differences throughout the domain in the composites as well a the prolonged events show that southwesterly windstorms typically coincide with conditions that are warmer and moister than normal. This was expected, as southerly synoptic flow will carry warmer and moister air from lower latitudes. It was suggested that windstorms, which see significant drying (down to 0-20 % RH) at the slope and in the lee, would mix with the flow in the moist flow in the Denmark Strait (typically 60-100 % during events) and reduce RH at its edge.

5.4 DISCUSSION

The work in this thesis addressed the general aims set out at the beginning of the thesis with some success: (i) To improve understanding of the role and significance of scalar turbulent exchange in the lee of mountains, (ii) to study the effect of turbulent flux parametrisations in the context of orographic flow representation in the UM, and (iii) to investigate the impacts of mountain-modulated flow on the downstream scalar atmospheric state fields and the large-scale circulation in the Iceland-Greenland Seas. Many open questions still remain and will need to be addressed in future work.

We found that increasing the amount of turbulent flux in the ABL produced a weaker downslope windstorm in our case study in a similar way that decreasing the model resolution from 0.5-km to 4.4-km did. This means that turbulent exchange in the ABL does play an important role in the reproduction of downslope windstorms,

but we were unable to determine how much of this effect was contributed by turbulent momentum flux and scalar turbulent flux, which were both enhanced by the parametrisation.

We recall the relative weakening of the downslope windstorm by reducing the resolution from 0.5-km to 4.4-km. But if we consider that a sub-kilometer-scale model (i.e. 0.5-km) would resolve more turbulent flux than lower resolutions (e.g. van Niekerk *et al.* (2020)), then given our finding that increased sub-grid turbulent flux also weakens the windstorm (like the 4.4-km model) we surmise that the model dynamics and resolved orography still play a more important role in the reproduction of downslope windstorms than turbulent exchange. However we do not have enough evidence to conclude that with certainty. A study that investigates a larger number of boundary layer and sub-grid turbulence parametrisations at different sub-kilometer and kilometer-scale resolutions may clarify this relationship. Furthermore it was suggested that ensemble forecasts are applied, which have already been used in downslope windstorm research with reasonable success (e.g. Reinecke & Durran (2009)). Constituent model forecasts in the ensemble would use a large range of different turbulence parametrisations and may reduce the uncertainty in the downstream impacts on the large-scale flow.

While we did employ a sub-kilometer-scale NWP (0.5-km) this is till far off the high resolutions of order 100-m recommended by Vosper *et al.* (2018) to simulate small-scale lee-side features in full detail. 200-m scale resolutions have been used by Sheridan & Vosper (2005) in idealised rotor simulations using non-idealised Falkland's orography, and by Gohm *et al.* (2008) (267-m resolution) to investigate the onset phase of a bora. However, some more recent downslope windstorm and gap flow studies still used kilometer-scale simulations with reasonable success, such as Lawson & Horel (2015) applied 1.3-km grid-spacing to their Wasatch windstorm simulation, and Elvidge *et al.* (2015) used a 2-km resolution model to study gap flows over the Larsen C ice shelf. It raises the question of how much more can be gained from increasing NWP resolution far beyond kilometer-scale grid-spacings, and an expanded resolution-sensitivity study over the Westfjords would help address that. Testing increasingly smoothed orography in the 0.5-km simulation would also help decouple the impact of resolved orography for the model physics and dynamics on downslope windstorm reproduction.

The research in this thesis showed that the impact of a resolved downslope windstorm in the 0.5-km simulation relative to its representation in coarser resolutions sometimes produced measurable differences in the 10-m and 1.5-m/2-m atmospheric state fields as far as 100-km downstream. It did not address the direct impacts resolution- and turbulence dependent differences in the atmospheric state fields have on the air-sea interaction as a result of these differences. A detailed analysis of the surface heat budget in the wake may reveal what influence downslope windstorms have on the currents in the Denmark Strait and the Icelandic shelf, if any. We also did not analyse conserved diagnostics in detail. The high-resolution windstorm climatology could be adapted to analyse cumulative potential vorticity (PV) shedding into the Denmark Strait area. PV banners in the lee of mountain ranges are linked to cyclogenesis (e.g. Schär *et al.* (2003)), which is applicable in the context of the high energy environment in and around the Denmark Strait, due to the strong winds seen in Harden & Renfrew (2012), for example.

To conclude, this thesis has made some efforts towards understanding the role of scalar turbulent flux in the lee of mountains, and broadened the scope to sensitivity in model resolution and dynamics. Yet more research needs to be conducted to qualify and quantify the downstream impacts of downslope windstorms in NWP models.

BIBLIOGRAPHY

Abatzoglou, John T., Hatchett, Benjamin J., Fox-Hughes, Paul, Gershunov, Alexander, & Nauslar, Nicholas J. 2020. Global climatology of synoptically-forced downslope winds. *International Journal of Climatology*, **41**(1), 31–50.

Aebischer, Urs, & Schär, Christoph. 1998. Low-Level Potential Vorticity and Cyclogenesis to the Lee of the Alps. *Journal of the Atmospheric Sciences*, **55**, 186–207.

Almansi, M., Haine, T. W. N., Gelderloos, R., & Pickart, R. S. 2020. Evolution of Denmark Strait Overflow Cyclones and Their Relationship to Overflow Surges. *Geophysical Research Letters*, **47**(4), 1–10.

Alpers, Werner, Ivanov, Andrei, & Horstmann, Jochen. 2009. Observations of Bora Events over the Adriatic Sea and Black Sea by Spaceborne Synthetic Aperture Radar. *Monthly Weather Review*, **137**(3), 1150–1161.

Aslam, Tahmeena, Hall, Rob A., & Dye, Stephen R. 2018. Internal tides in a dentritic submarine canyon. *Progress in Oceanography*, **169**, 20–32.

Beare, Robert J., Macvean, Malcom K., Holtslag, Albert A. M., Cuxart, Joan, Esau, Igor, Golaz, Jean-Christophe, Jimenez, Maria A., Khairoutdinov, Marat, Kosovic, Branko, Lewellen, David, Lund, Thomas S., Lundquist, Julie K., Mccabe, Anne, Moene, Arnold F., Noh, Yign, Raasch, Siegfried, & Sullivan, Peter. 2006. An Intercomparison of Large-Eddy Simulations of the Stable Boundary Layer. *Boundary-Layer Meteorology*, **118**, 247–272.

Bengtsson, Lisa, Andrae, Ulf, Aspelien, Trygve, Batrak, Yurii, Calvo, Javier, de Rooy, Wim, Gleeson, Emily, Hansen-Sass, Bent, Homlied, Mariken, Hortal, Mariano, Ivarsson, Karl-Ivar, Lenderink, Geert, Niemelä, Sami, Nielsen, Kristian Pagh, Onvlee, Jeanette, Rontu, Laura, Samuelsson, Patrick, Muñoz, Daniel Santos, Subias, Alvaro, Tijm, Sander, Toll, Velle, Yang, Xiaohua, & Køltzow, Morten Ødegaard.

2017. The HARMONIE-AROME Model COnfiguration in the ALADIN-HIRLAM NWP System. *Monthly Weather Review*, **145**, 1919–1935.

Beusch, Lea, Raveh-Rubin, Shira, Sprenger, Michael, & Papritz, Lukas. 2018. Dynamics of a Puelche foehn event in the Andes. *Meteorologische Zeitschrift*, **27**(1), 67–80.

Billings, Brian J., & Grubišić, Vanda. 2008. Climatology of the Sierra Nevada Mountain-Wave Events. *Monthly Weather Review*, **136**(2), 757–768.

Brown, A. R., Beare, R. J., Edwards, J. M., Lock, A. P., Keogh, S. J., Milton, S. F., & Walters, D. N. 2008. Upgrades to the Boundary-Layer Scheme in the Met Office Numerical Weather Prediction Model. *Boundary-Layer Meteorology*, **128**, 117–132.

Doyle, James D., & Durran, Dale R. 2007. Rotor and Subrotor Dynamics in the Lee of Three-Dimensional Terrain. *Journal of the Atmospheric Sciences*, **64**(12), 4202–4221.

Durran, Dale R. 1986. Another Look at Downslope Windstorms. Part I: The Development of Analogs to Supercritical Flow in an Infinitely Deep, Continuously Stratified Fluid. *Journal of the Atmospheric Sciences*, **43**(21), 2527–2543.

Durran, Dale R., & Klemp, Joseph B. 1987. Another Look at Downslope Winds. Part II: Nonlinear Amplification beneath Wave-Overturning Layers. *Journal of the Atmospheric Sciences*, **44**(22), 3402–3412.

Durran, Dale R., & Menchaca, Maximo Q. 2017. Mountain Waves, Downslope Winds, and Low-Level Blocking Forced by a Midlatitude Cyclone Encountering an Isolated Ridge. *Journal of the Atmospheric Sciences*, **74**(2), 617–639.

Elvidge, Andrew D., & Renfrew, Ian A. 2016. The Causes of Foehn Warming in the Lee of Mountains. *Bulletin of the American Meteorological Society*, **97**(3), 455–466.

Elvidge, Andrew D., Renfrew, Ian A., King, John C., Orr, Andrew, Lachlan-Cope, Tom A., Weeks, Mark, & Gray, Sue L. 2015. Foehn jets over the Larsen C Ice Shelf, Antarctica. *Quarterly Journal of the Royal Meteorological Society*, **141**(688), 698–713.

Elvidge, Andrew D., Vosper, Simon B., Wells, Helen, Cheung, Jacob C. H., Derbyshire, Steve H., & Turp, Debi. 2017. Moving towards a wave-resolved approach

to forecasting mountain wave induced clear air turbulence. *Meteorological Applications*, **24**(3), 540–550.

Gaberšek, Saša, & Durran, Dale R. 2004. Gap Flows through Idealized Topography. Part I: Forcing by Large-Scale Winds in the Nonrotating Limit. *Journal of the Atmospheric Sciences*, **61**, 2846–2862.

Gohm, Alexander, Mayr, Georg J., Fix, Andreas, & Giez, Andreas. 2008. On the onset of bora and the formation of rotors and jumps near a mountain gap. *Quarterly Journal of the Royal Meteorological Society*, **134**(630), 21–46.

Guzman-Morales, Janin, Gershunov, Alexander, Theiss, Jurgen, Li, Haiqin, & Cayan, Daniel. 2016. Santa Ana Winds of Southern California: Their climatology, extremes, and behavior spanning six and a half decades. *Geophysical Research Letters*, **43**(6), 2827–2834.

Harden, B. E., & Renfrew, I. A. 2012. On the spatial distribution of high winds off southeast Greenland. *Geophysical Research Letters*, **39**(14), 1–6.

Hersbach, Hans, Bell, Bill, Berrisford, Paul, Hirahara, Shoji, Horányi, András, Muñoz-Sabater, Joaquín, Nicolas, Julien, Peubey, Carole, Radu, Raluca, Schepers, Dinand, Simmons, Adrian, Soci, Cornel, Abdalla, Saleh, Abellan, Xavier, Balsamo, Gianpaolo, Bechtold, Peter, Biavati, Gionata, Bidlot, Jean, Bonavita, Massimo, De Chiara, Giovanna, Dahlgren, Per, Dee, Dick, Diamantakis, Michail, Dragani, Rossana, Flemming, Johannes, Forbes, Richard, Fuentes, Manuel, Geer, Alan, Haimberger, Leo, Healy, Sean, Hogan, Robin J., Hólm, Elías, Janisková, Marta, Keeley, Sarah, Laloyaux, Patrick, Lopez, Philippe, Lupu, Cristina, Radnoti, Gabor, de Rosnay, Patricia, Rozum, Iryna, Vamborg, Freja, Villaume, Sebastien, & Thépaut, Jean-Noël. 2020. The ERA5 global reanalysis. *Quarterly Journal of the Royal Meteorological Society*, **146**(730), 1999–2049.

Hertenstein, Rolf F., & Kuettner, Joachim P. 2005. Rotor types associated with steep lee topography: influence of the wind profile. *Tellus*, **57**, 117–135.

Hughes, Mimi, & Hall, ALex. 2010. Local and synoptic mechanisms causing Southern California's Santa Ana winds. *Climate Dynamics*, **34**, 847–857.

Jackson, Peter L., Mayr, Georg, & Vosper, Simon. 2013. *Dynamically-Driven Winds*. Dortrecht, Heidelberg, New York, London: Springer. Book Section 3, pages 121–173.

Jiang, Qingfang, & Doyle, James D. 2004. Gravity Wave Breaking over the Central Alps: Role of Complex Terrain. *Journal of Atmospheric Sciences*, **61**(18), 2249–2266.

Jiang, Qingfang, & Doyle, James D. 2005. Wave breaking induced surface wakes and jets observed during a bora event. *Geophysical Research Letters*, **32**(17), 1–5.

Jiang, Qingfang, & Doyle, James D. 2009. The Impact of Moisture on Mountain Waves during T-REX. *Monthly Weather Review*, **137**(11), 3888–3906.

King, J. C., Connolley, W. M., & Derbyshire, S. H. 2001. Sensitivity of modelled Antarctic climate to surface and boundarly-layer flux parametrizations. *Quarterly Journal of the Royal Meteorological Society*, **127**, 779–794.

Klemp, J. B., & Durran, D. R. 1987. Numerical modelling of Bora winds. *Meteorology and Atmospheric Physics*, **36**, 215–227.

Klemp, J. B., & Lilly, D. R. 1975. The Dynamics of Wave-Induced Downslope Winds. *Journal of the Atmospheric Sciences*, **32**(2), 320–339.

Køltzow, Morten, Schyberg, Harald, Støylen, Eivind, & Yang, Xiaohua. 2022. Value of the Copernicus Arctic Rgional Reanalysis)(CARRA) in representing near-surface temperature and wind speed in the north-east European Arctic. *Polar Research*, **41**.

Lawson, John, & Horel, John. 2015. Analysis of the 1 December 2011 Wasatch Downslope Windstorm. *Weather and Forecasting*, **30**(1), 115–135.

Lehner, Manuela, & Rotach, Mathias W. 2018. Current Challenges in Understanding and Predicting Transport and Exchange in the Atmosphere over Mountainous Terrain. *Atmosphere*, **9**(276), 1–28.

Lilly, D. K., & Zipser, E. J. 1972. The Front Range Windstorm of 11 January 1972 A Meteorological Narrative. *Weatherwise*, **25**(2), 56–63.

Lock, A., Edwards, J., & Boutle, I. 2021. *Unified Model Documentation paper 024: The Parametrization of Boundary Layer Processes*.

Long, Robert R. 1954. Some Aspects of the Flow of Stratified Fluids. *Tellus*, **6**(2), 97–115.

Louis, J.-F. 1979. A Parametric Model of Vertical Eddy Fluxes in the Atmosphere. *Boundary-Layer Meteorology*, **17**, 187–202.

Lozier, M. S., Li, F., Bahr, F., Bower, A. S., Cunningham, S. A., De Jong, M. F., De Steur, L., Deyoung, B., Fischer, J., Gray, S. F., Greenan, B. J. W., Holliday, N. P., Houk, A., Houpert, L., Inall, M. E., Johns, W. E., Johnson, H. L., Johnson, C., Karstensen, J., Koman, G., Le Bras, I. A., Lin, X., Mackay, N., Marshall, D. P., Mercier, H., Oltmanns, M., Pickart, R. S., Ramsey, A. L., Rayner, D., Straneo, F., Thierry, V., Torres, D. J., Williams, R. G., Wilson, C., Yang, J., Yashayaev, I., & Zhao, J. 2019. A sea change in our view of overturning in the subpolar North Atlantic. *Science*, **363**(6426), 516–521.

Mayr, Georg J., Armi, Laurence, Gohm, Alexander, Zängl, Günther, Durran, Dale R., Flamant, Cyrille, Gaberšek, Saša, Mobbs, Stephen, Ross, Andrew, & Weissmann, Martin. 2007. Gap flows: Results from the Mesoscale Alpine Programme. *Quarterly Journal of the Royal Meteorological Society*, **133**(625), 881–896.

Miltenberger, Annette K., Field, Paul R., Hill, Adrian H., & Heymsfield, Andrew J. 2020. Vertical redistribution of moisture and aerosol in orographic mixed-phase clouds. *Atmospheric Chemistry and Physics*, **20**, 7979–8001.

Montecinos, Aldo, Muños, Ricardo C., Oviedo, Stephanie, Martínez, Andrés, & Villagrán, Víctor. 2017. Climatological Characterization of Puelche Winds down the Western Slope of the Extratropical Andes Mountains Using the NCEP Climate Forecast System Reanalysis. *Journal of Applied Meteorology and Climatology*, **56**(3), 677–696.

Moore, G. W. K. 2021. Impact of model resolution on the representation of the wind field along Nares Strait. *Scientific Reports*, **11**, 1–14.

Moore, G. W. K., & Imrit, A. A. 2022. Impact of Resolution on the Representation of the Mean and Extreme Winds Along Nares Strait. *Journal of Geophysical Research: Atmospheres*, **127**, 1–17.

Oltmanns, M., Straneo, F., Seo, H., & Moore, G. W. K. 2015. The Role of Wave Dynamics and Small-Scale Topography for Downslope Wind Events in Southeast Greenland. *Journal of the Atmospheric Sciences*, **72**(7), 2786–2805.

Peltier, W. R., & Clark, T. L. 1979. The Evlution and Stability of Finite-Amplitude Mountain Waves. Part II: Surface Wave Drag and Severe Downslope Windstorms. *Journal of the Atmospheric Sciences*, **36**(8), 1498–1529.

Petersen, G. N., & Renfrew, I. A. 2009. Aircraft-based observations of air-sea fluxes over Denmark Strait and the Irminger Sea during high wind speed conditions. *Quarterly Journal of the Royal Meteorological Society*, **135**(645), 2030–2045.

Plavcan, David, & Mayr, Georg J. 2014. Automatic and Probabilistic Foehn Diagnosis with a Statistical Mixture Model. *Journal of Applied Meteorology and Climatology*, **53**, 652–659.

Reinecke, Patrick A., & Durran, Dale R. 2009. Initial-Condition Sensitivites and the Predictability of Downslope Windstorms. *Journal of the Atmospheric Sciences*, **66**, 3401–3418.

Renfrew, I. A., Pickart, R. S., Våge, K., Moore, G. W. K., Bracegirdle, T. J., Elvidge, A. D., Jeansson, E., Lachlan-Cope, T., McRaven, L. T., Papritz, L., Reuder, J., Sodemann, H., Terpstra, A., Waterman, S., Valdimarsson, H., Weiss, A., Almansi, M., Bahr, F., Brakstad, A., Barrell, C., Brooke, J. K., Brooks, B. J., Brooks, I. M., Brooks, M. E., Bruvik, E. M., Duscha, C., Fer, I., Golid, H. M., Hallerstig, M., Hessevik, I., Huang, J., Houghton, L., Jónsson, S., Jonassen, M., Jackson, K., Kvalsund, K., Kolstad, E. W., Konstali, K., Kristiansen, J., Ladkin, R., Lin, P., Macrander, A., Mitchell, A., Olafsson, H., Pacini, A., Payne, C., Palmason, B., Pérez-Hernández, M. D., Peterson, A. K., Petersen, G. N., Pisareva, M. N., Pope, J. O., Seidl, A., Semper, S., Sergeev, D., Skjelsvik, S., Søiland, H., Smith, D., Spall, M. A., Spengler, T., Touzeau, A., Tupper, G., Weng, Y., Williams, K. D., Yang, X., & Zhou, S. 2019. The Iceland Greenland Seas Project. *Bulletin of the American Meteorological Society*, **100**(9), 1795–1817.

Rögnvaldsson, Ó, Bao, J. W., Ágústsson, H., & Ólafsson, H. 2011. Downslope windstorm in Iceland – WRF/MM5 model comparison. *Atmospheric Chemistry and Physics*, **11**(1), 103–120.

Sandu, Irina, van Niekerk, Annelize, Shepherd, Theodore G., Vosper, Simon B., Zadra, Ayrton, Bacmeister, Julio, Beljaars, Anton, Brown, Andrew R., Dörnbrack, Andreas, McFarlane, Norman, Puithan, Felix, & Svensson, Gunilla. 2019. Impacts of orography on large-scale atmospheric circulation. *npj Climate and Atmospheric Science*, **2**(10), 1–8.

Schär, Christoph, Sprenger, Michael, Lüthi, Daniel, Jiang, Qingfang, Smith, Ronald B., & Benoit, Robert. 2003. Structure and dynamics of an Alpine potential-vorticity banner. *Quarterly Journal of the Royal Meteorological Society*, **129**, 825–855.

Serafin, Stefano, Strauss, Lukas, & Grubišić, Vanda. 2017. Climatology of Westerly Wind Events in the Lee of the Sierra Nevada. *Journal of Applied Meteorology and Climatology*, **56**(4), 1003–1023.

Serafin, Stefano, Adler, Bianca, Cuxart, Joan, De Wekker, Stephan, Gohm, Alexander, Grisogono, Branko, Kalthoff, Norbert, Kirshbaum, Daniel, Rotach, Mathias, Schmidli, Jürg, Stiperski, Ivana, Večenaj, Željko, & Zardi, Dino. 2018. Exchange Processes in the Atmospheric Boundary Layer Over Mountainous Terrain. *Atmosphere*, **9**(3), 16–32.

Sergeev, D. E., Renfrew, I. A., Spengler, T., & Dorling, S. R. 2017. Structure of a shear-line polar low. *Quarterly Journal of the Royal Meteorological Society*, **143**(702), 12–26.

Sheridan, P. F., & Vosper, S. B. 2005. Numerical simulations of rotors, hydraulic jumps and eddy shedding in the Falkland Islands. *Atmospheric Science Letters*, **6**(4), 211–218.

Sheridan, P. F., & Vosper, S. B. 2006. A flow regime diagram for forecasting lee waves, rotors and downslope winds. *Meteorological Applications*, **13**(02), 179–195.

Sheridan, Peter, & Vosper, Simon. 2012. High-Resolution Simulations of Lee Waves and Downslope Winds over the Sierra Nevada during T-REX IOP 6. *Journal of Applied Meteorology and Climatology*, **51**(7), 1333–1352.

Shestakova, Anna A., Toropov, Pavel A., & Matveeva, Tatiana A. 2020. Climatology of extreme downslope windstorms in the Russian Arctic. *Weather and Climate Extremes*, **28**(100256), 1–14.

Smith, Craig, Hatchett, Benjamin, & Kaplan, Michael. 2018. A Surface Observation Based Climatology of Diablo-LikeWinds in California's Wine Country and Western Sierra Nevada. *Fire*, **1**(2), 1–9.

Smith, Ronald B. 1980. Linear Theory of stratified hydrostatic flow past an isolated mountain. *Tellus*, **32**, 348–364.

Smith, Ronald B. 1985. On Severe Downslope Winds. *Journal of Atmospheric Sciences*, **42**(23), 2597–2603.

Smith, Ronald B. 1987. Aerial Observations of the Yugoslavian Bora. *Journal of the Atmospheric Sciences*, **44**(2), 269–297.

Smith, Ronald B. 1988. Linear Theory of Stratified Flow pas an Isolated Mountain in Isoteric Coordinates. *Journal of the Atmospheric Sciences*, **45**(24), 3889–3896.

Smith, Ronald B. 1989. Hydrostatic Airflow over Mountains. *Advances in Geophysics*, **31**, 1–41.

van Niekerk, Annelize, Sandu, Irina, Zadra, Ayrton, Bazile, Eric, Kanehama, Takafumi, Köhler, Martin, Koo, Myung-Seo, Choi, Jyun-Joo, Kuroki, Yukihiro, Toy, Michael D., Vosper, Simon B., & Yudin, Valery. 2020. COnstraining ORographic Drag Effects (COORDE): A Model COmparison of Resolved abd Parametrized Orographic Drag. *Journal of Advances in Modeling Earth Systems*, **12**(11), 1–27.

Vosper, S. B. 2004. Inversion effects on mountain lee waves. *Quarterly Journal of the Royal Meteorological Society*, **130**(600), 1723–1748.

Vosper, S. B. 2015. Mountain waves and wakes generated by South Georgia: implications for drag parametrization. *Quarterly Journal of the Royal Meteorological Society*, **141**(692), 2813–2827.

Vosper, S. B., Brown, A. R., & Webster, S. 2016. Orographic drag on islands in the NWP mountain grey zone. *Quarterly Journal of the Royal Meteorological Society*, **142**(701), 3128–3137.

Vosper, Simon, Ross, Andrew, Renfrew, Ian, Sheridan, Peter, Elvidge, Andrew, & Grubišić, Vanda. 2018. Current Challenges in Orographic Flow Dynamics:

Turbulent Exchange Due to Low-Level Gravity-Wave Processes. *Atmosphere*, **9**(9), 1–18.

Wallace, John M., & Hobbs, Peter V. 2006. *Atmospheric Science: An Introductory Survey*. International Geophysics Series, vol. 92. Amsterdam, Boston, Heidelberg, London, New York, Oxford, Paris, San DIego, San Francisco, SIngapore, Sydney, Tokyo: Academic Press.

Walters, David, Boutle, Ian, Brooks, Malcolm, Melvin, Thomas, Stratton, Rachel, Vosper, Simon, Wells, Helen, Williams, Keith, Wood, Nigel, Allen, Thomas, Bushell, Andrew, Copsey, Dan, Earnshaw, Paul, Edwards, John, Gross, Markus, Hardiman, Steven, Harris, Chris, Heming, Julian, Klingaman, Nicholas, Levine, Richard, Manners, James, Martin, Gill, Milton, Sean, Mittermaier, Marion, Morcrette, Cyril, Riddick, Thomas, Roberts, Malcolm, Sanchez, Claudio, Selwood, Paul, Stirling, Alison, Smith, Chris, Suri, Dan, Tennant, Warren, Vidale, Pier Luigi, Wilkinson, Jonathan, Willett, Martin, Woolnough, Steve, & Xavier, Prince. 2017. The Met Office Unified Model Global Atmosphere 6.0/6.1 and JULES Global Land 6.0/6.1 configurations. *Geoscientific Model Development*, **10**(4), 1487–1520.

Whiteman, C. David. 2000. *Mountain Meteorology: Fundamentals and Applications*. Oxford, New York: Oxford Univeristy Press.

Wood, Nigel, Staniforth, Andrew, White, Andy, Allen, Thomas, Diamantakis, Michail, Gross, Markus, Melvin, Thomas, Smith, Chris, Vosper, Simon, Zerroukat, Mohamed, & Thuburn, John. 2014. An inherently mass-conserving semi-implicit semi-Langrangian discretization of the deep-atmosphere global non-hydrostatic equations. *Quarterly Journal of the Royal Meteorological Society*, **140**(682), 1505–1520.

Ágústsson, Hálfdán, Bao, Jian-Wen, Rögnvaldsson, Ólafur, & Ólafsson, Haraldur. 2007. Downslope windstorms in Iceland - WRF/MM5 model comparison - II. *NCAR Tech. Note*.

Ágústsson, Hálfdán, & Ólafsson, Haraldur. 2010. The bimodal downslope windstorms at Kvísker. *Meteorology and Atmospheric Physics*, **116**(1-2), 27–42.

Ólafsson, Haraldur, & Bougeault, Philippe. 1996. Nonlinear Flow Past an Elliptic Mountain Ridge. *Journal of the Atmospheric Sciences*, **53**(17), 2465–2488.

Ólafsson, Haraldur, & Ágústsson, Hálfdán. 2007. The Freysnes downslope windstorm. *Meteorologische Zeitschrift*, **16**(1), 123–130.